



Universidade do Minho
Escola de Ciências

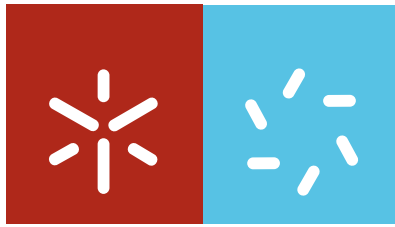
Nuno Miguel Azevedo Machado de Araújo **Kinetics of deposition and post evolution relaxation in thin-films**

Nuno Miguel Azevedo Machado de Araújo

**Kinetics of deposition and post evolution
relaxation in thin-films**

UMinho | 2009

Julho de 2009



Universidade do Minho
Escola de Ciências

Nuno Miguel Azevedo Machado de Araújo

**Kinetics of deposition and post evolution
relaxation in thin-films**

Tese de Doutoramento em Ciências
Área de conhecimento Física

Trabalho efectuado sob orientação do
Professor Doutor António Manuel Rosa Cadilhe

Julho de 2009

É AUTORIZADA A REPRODUÇÃO PARCIAL DESTA TESE,
APENAS PARA EFEITOS DE INVESTIGAÇÃO, MEDIANTE DECLARAÇÃO
ESCRITA DO INTERESSADO, QUE A TAL SE COMPROMETE.

Kinetics of deposition and post evolution relaxation in
thin-films

Nuno Miguel Azevedo Machado de Araújo

“The progress of science is marked by the continual success of attempts to unify greater and greater range of phenomena in more and more comprehensive theoretical schemes.”

L. Sklar, in *Physics and Chance: Philosophical issues in the foundations of statistical mechanics*.

Abstract

This thesis is devoted to the use of statistical physics concepts to study the growth of films, under nonequilibrium conditions. Specifically, we consider the influence of the particle/particle and particle/substrate interacting rules on the morphology of the obtained film.

We report how interesting structures can emerge from interacting rules as simple as the ones from the random sequential adsorption process. In the presence of a patterned substrate, made up of well defined regions (cells) where particles can irreversibly stick, a rich set of morphologies are obtained at the jammed state. Such structures reveal, not only the order of the pattern, but also the stochastic nature of the adsorption process and the competition during adsorption. Besides, we show that such pattern changes also the kinetics toward the asymptotic limit and report, for the first time, a transition from power law to exponential, in the functional dependence of the coverage approach to the jamming value.

The competitive adsorption of segments with different sizes on a line is also considered. The influence of the size ratio on the jammed state structure is analyzed with the cumulants of the distance between segments, up-to the fourth order. Yet, a probability distribution function of distances is proposed, based on heuristic arguments. The obtained results with the proposed function are in agreement with the ones from simulation.

For the growth regime where diffusion of particles on the substrate cannot be neglected, the influence of the flux of impinging particles on the nucleation and growth of islands is studied. A model based on the kinetic Monte Carlo method is then proposed to study the

homoepitaxial growth of Ag/Ag(100). Based on symmetry considerations, for both the substrate geometry and the interaction potential, the list of possible processes is reduced from 1024 to 241 elements. The model is able to reproduce previously reported results as well as gain new insights into the nucleation process, specially, for cases where the shape of the island and its local environment, play an important role on the overall kinetics.

Resumo

Nesta tese, aplicam-se conceitos de física estatística ao estudo de crescimento de filmes em condições de não equilíbrio. Considera-se o efeito da interação partícula/partícula e partícula/substrato na morfologia do filme.

Através de simulações de Monte Carlo, mostra-se que estruturas interessantes podem emergir de processos tão simples como a deposição sequencial aleatória. Uma grande variedade de estruturas pode ser obtida na presença de um padrão, constituído por regiões bem definidas (células) onde as partículas podem adsorver irreversivelmente. Estas estruturas devem-se ao efeito conjugado das restrições introduzidas pelo padrão e do efeito cooperativo entre as partículas durante a adsorção. Mostra-se ainda que, na presença do padrão, há uma transição de lei de potência para exponencial, na dependência funcional da aproximação da cobertura ao estado limite.

É também estudada a adsorção competitiva de segmentos de dois tamanhos diferentes, numa linha. A influência da relação de tamanhos na estrutura final é caracterizada com base nos momentos (de elevada ordem) da distância entre segmentos. Propõe-se uma função de densidade de probabilidade para as distâncias, estando os resultados obtidos com essa função em concordância com os obtidos computacionalmente.

Finalmente, estuda-se a deposição e a relaxação de átomos numa superfície cristalina, desenvolvendo-se um modelo com base no método de Monte Carlo cinético, para estudar o crescimento de Ag/Ag(100). Com considerações de simetria baseadas no substrato e no potencial de interação, a lista de possíveis processos é reduzida de 1024 para 241 elementos. O modelo considerado é capaz de reproduzir resultados anteriores, bem como

permitir obter mais informação sobre o processo de nucleação, em especial nas situações em que tanto a forma da ilha como o meio em que se encontra desempenham um papel fundamental na cinética do sistema.

Preface

This thesis is the result of my PhD research, started in October of 2005, at the *Universidade do Minho*, in the field of far-from-equilibrium statistical physics. During this journey, I have got the opportunity to interact with many people at the University, the *Los Alamos National Laboratory*, and several conferences, who contributed to my work and to what I am today.

Professor António Cadilhe has introduced me the field of far-from-equilibrium physics, when I was an undergraduate student. At that time, he draw me into research issues, with the opportunity to engage in a project. Since then, during the last six years, he has guided myself, not only in the research itself, but also in the study of advanced topics in physics. For all this and much more, I am deeply indebted with him.

I am also grateful to professor Vladimir Privman for all the advices that he gave me, specially in this later stage. My thanks also to Dr. Arthur Voter for the opportunity to work during three months with him, at the *Los Alamos National Laboratory*, from which I have, definitely, benefited.

Nonetheless, this thesis has profited from the careful reading and scrutiny of several friends. Thanks are due to Cristóvão Dias, João Filipe Marques, Abhijit Chatterjee, Isabel Araújo, Sofia Vila-Chã, and Joaquim Machado. To them, my deep gratefulness.

In addition, I wish to acknowledge the *Fundação para a Ciência e a Tecnologia* the fellowship (SFRH/BD/17467/2004) and to the project SeARCH the computational facilities.

Contents

Abstract	iii
Resumo	v
Preface	vii
Contents	ix
List of Tables	xvii
List of Figures	xix
I Introduction and Theoretical Considerations	1
1 Statistical physics and out-of-equilibrium systems	3
1.1 Phase space, state vector, phase functions	7
1.2 Equilibrium vs out of equilibrium	9
1.3 From Hamilton's dynamics to Liouville's equation	10
1.4 Energy landscape	13
1.5 Stochastic processes	14
1.5.1 Langevin equation	15
1.5.2 Master equation	17
1.6 Statistical-physics growth models	19

1.6.1	Eden growth model	21
1.6.2	Diffusion-limited aggregation	22
1.7	Scaling and universality	22
1.7.1	Scaling law for the Random Deposition model	25
1.7.2	Ballistic deposition	27
2	Computational methods in statistical physics	33
2.1	The Monte Carlo method	37
2.1.1	Standard Monte Carlo	39
2.1.2	Kinetic Monte Carlo	47
II	Micro- to Nano-Scale	53
3	Competitive adsorption on a line	55
3.1	Model	57
3.2	Definitions and relations	58
3.3	Monte Carlo simulations	63
3.3.1	Algorithm	63
3.3.2	Simulations	64
3.3.3	Results	65
3.4	The gap-size distribution	73
3.4.1	Computational results	74
3.4.2	Proposed function	75
3.5	Conclusions	78
4	How can a pattern change the irreversible adsorption?	81
4.1	Model and definitions	83
4.2	The “Phase Diagram”	87
4.3	The jammed state	89

4.3.1	Noninteracting cell-cell adsorption	89
4.3.2	Interacting cell-cell adsorption	94
4.3.3	Interparticle distribution function	99
4.4	Adsorption kinetics	103
4.5	An efficient algorithm	111
4.5.1	Clean substrate	113
4.5.2	Mesh-cell test conditions	117
4.5.3	Pre-patterned substrate	119
4.5.4	Some results	120
4.5.5	Measurement of empty area distribution	126
4.6	Conclusions	126
 III Down to the Atomic Scale		129
 5 Islands nucleation and growth		131
5.1	Surface diffusion	133
5.2	Definitions	135
5.3	Modeling islands nucleation and growth	136
5.3.1	Rate equations	138
5.4	Model	141
5.5	Results	146
5.6	Conclusions	153
 Final Remarks		155
 Bibliography		159
 Index		187

Nomenclature

q set of generalized coordinates

p set of generalized momenta

f degrees of freedom

\vec{X} state vector

$F(\vec{X})$ space function

\mathcal{H} Hamiltonian

t time

ρ phase-space density

v velocity

γ friction coefficient

η noise term

$\delta(t)$ Dirac delta function

Γ strength of the noise

m particle mass

k_B Boltzmann constant

T	temperature
$P_s(t)$	population of the state s
W_{ij}	transition rate from state i to state j
E	energy
E_i	energy of state i
E_a	activation energy
ν_i	rate of process i
ν_0	attempt frequency
L	linear system size
h	column height
w	interface roughness
w_{sat}	saturation roughness
$\tilde{\alpha}$	roughness exponent
$\tilde{\beta}$	growth exponent
t_\times	crossover time
z	dynamic exponent
\mathcal{O}	observable
σ_i	spin
J_{ij}	strength of the exchange interaction between spin i and j
γ_T	$\exp\left(\frac{J}{k_B T}\right)$

Y_i	random number of type i
$t_{i,low}$	time of process i at T_{low}
$t_{i,high}$	time of process i at T_{high}
R	size ratio of the deposited segments
Φ_i	deposition flux of specie i
θ	coverage
θ_J	jamming coverage
σ_J	jamming coverage standard deviation
$P_i(x)$	probability distribution of empty space of type i
$\langle x^n \rangle_a$	moment of order n of the a gap-size distribution
κ_m^a	cumulant of order m of the a gap-size distribution
$G_a(k)$	characteristic function
S_a	skewness
K_a	kurtosis
r_0	particle radius
r_{\min}	minimum particle radius
r_{\max}	maximum particle radius
α	cell size in units of particle diameter
β	cell-cell separation in units of particle diameter
σ_θ	coverage error

Λ	area engulfing all available areas for adsorption
c	linear size of the mesh cell
t_{CPU}	computational run time
N_p	density of particles
D_c	collective diffusion coefficient
D	(tracer) diffusion coefficient
\mathcal{F}	Helmholtz free energy
S	entropy
N_{isl}	density of islands
s	island size
N_1	density of adatoms
n_s	number of islands with size s
N_s	density of islands with size s
s_{av}	mean island size
Φ	deposition flux
R_M	ratio between the diffusion coefficient and the flux
U_i	capture rate of adatoms by islands with size i
θ_{s^*}	coverage of the substrate by stable islands

List of Tables

2.1	Scheme of all possible configurations in a 2×2 square lattice of Ising spins. For such system $2^4 = 16$ different configurations are possible. For each scheme is the fraction of configurations as well as the Boltzmann factor obtained by considering periodic boundary conditions and an exchange interaction J . The parameter γ_T is defined as $\exp\left(\frac{J}{k_B T}\right)$	45
3.1	The table presents the coverage, θ_J , as a function of the size ratio, R , while σ represents the associated error. These results are for a system size of 10^7 and for 10^2 samples.	67
3.2	The table summarizes the estimated values of R , where the first four cumulants take maximum and minimum values, all measured with an error of ± 0.005 . The corresponding values of the cumulants are also included. Cells marked with $(*)$ means that the BB -gap is strictly monotonic. . . .	70

-
- 4.1 The table shows the jammed coverage values in the NICCA-MPCA case, i.e., for $\beta \geq 1$ and $\alpha \geq 1/\sqrt{2}$. In the first column, n is the number of particles per unit cell of the close-packed situation. The values of α_n , defined in the text, are shown in the second column. The third column gives the close-packed coverage values for the range of up-to- n particles per cell. In the fourth column, the jamming coverage values, θ_J , from simulations are presented. These values are for a representative choice $\beta = \beta^* = 1.2$ (see text), and for the α values shown in the second column. Finally, in the fifth column, the standard deviation, σ_J , of the jamming coverages is given. 93
- 4.2 Tabulation of numerically simulated RSA jammed-coverage values, at fixed $\beta = \beta^* = 1.2$, for the range of α from 0.72 to 1.40. The standard deviations are also shown. 95
- 4.3 The table shows simulated values of the coverage, θ_J , and the corresponding standard deviation σ_J , for several values of α and β , in the ICCA-SPCA and ICCA-MPCA regions of the “phase diagram” shown in Fig. 4.3. . . . 96
- 4.4 The table presents the jammed state coverage (θ_∞), the coverage error (σ_θ), and the computational run time (t_{CPU}), as a function of the linear system size (L), for 10^3 independent runs of monodisperse particles adsorption on clean/regular substrate. 121
- 5.1 The table summarize the contributions (ΔE) of each fundamental process to the activation barrier, eq. (5.23). Values computed from different processes cataloged by Voter [39]. 145

List of Figures

1.1	Snapshots of Eden model. (a) Aggregate with 12 000 particles (the red sites are the active ones). (b) Aggregate with 1 200 000 particles.	21
1.2	Snapshots of Diffusion-limited aggregation (DLA) model. (a) Aggregate with 500 particles. (b) Aggregate with 50 000 particles.	23
1.3	Rules for the Random Deposition model.	25
1.4	(a) Snapshot for Random Deposition model on a linear lattice with size 500 after the deposition of 500 layers. Color changes for each 100 layers. (b) For Random Deposition model on a linear lattice with size 10^3 , roughness as a function of time (measured in terms of deposited layers). Results sampled over 10^3 samples.	26
1.5	Rules for the Ballistic Deposition model.	28
1.6	(a) Snapshot for Ballistic Deposition model on a linear lattice with size 500 after the deposition of 500 layers. Color changes for each 100 layers. (b) Interface roughness as a function of time for a system size of 4096. (c) Saturation roughness as a function of system size. (d) Crossover time as a function of system size. All the results were averaged over 10^4 samples. . .	29
1.7	Plot of the scaling function for different values of system size.	31
2.1	Relationship between theory, experiment, and computer simulations. From David P. Landau and Kurt Binder. [56]	35

2.2	Snapshots of percolation model for a square lattice with 4 million lattice sites: before, near, and above the percolation threshold.	40
2.3	Fraction of samples with percolation clusters (f_p) as a function of occupation probability, p , for different linear system sizes, L , namely, 1024, 2048, 4096, and 8192. Results average over 10^4 samples.	41
2.4	Snapshots of the equilibrium configuration for the Ising model: below, near, and above the critical temperature. System with 250 thousand spins interacting according to the Hamiltonian of eq. (2.3). Obtained after L^2 Monte Carlo steps.	43
3.1	Rules of the <i>Random Sequential Adsorption</i> model.	58
3.2	Algorithm cartoon for three consecutive steps (a), (b), and (c). The dashed particles represent segments adsorbed during the elapsing step.	64
3.3	Coverage dependence on the size ratio for equal depositing fluxes of each segment size, for various values of the size ratio, namely, 1, 1.1, 2, 4, and 10. Results obtained for a system size of 10^6 and averaged over 10^2 samples.	65
3.4	Coverage dependence on the size ratio for equal depositing fluxes of each segment size. Plot showing the jamming coverage dependence on the size ratio.	66
3.5	Fraction of available empty space, at the jamming state. In the insets the size ratio varies between 1 and 20. One has the <i>AA</i> -, <i>AB</i> -, and <i>BB</i> -gap types represented by circles, squares, and triangles, respectively. Due to symmetry reasons, the <i>BA</i> case (non filled squares) is equal to the <i>AB</i> one.	68
3.6	Normalized population of gaps at the jamming state. In the insets the size ratio varies between 1 and 20. We use the same legend as in Fig. 3.5.	69

-
- 3.7 Plots involving cumulants up to the fourth order of the gap-size distribution functions for each gap type as a function of the size ratio. Results obtained through Monte Carlo simulations (a, b, c, and d) and from proposed function to the gap-size distribution (e, f, g, and h). We use the same legend as in Fig. 3.5. (a) and (e) Average distance between pairs of segments. (b) and (f) Dispersion of the distance between pairs of segments. (c) and (g) Skewness. (d) and (h) Kurtosis. 71
- 3.8 Gap-size distribution functions at the jamming state: For a size ratio of one, the solid curve represents $P_0(x)$, while the remaining *AA*-, *AB*-, and *BB*-gap types are identical, and therefore fall onto a single curve. 74
- 3.9 Gap-size distribution functions at the jamming state: For a size ratio of 2.0, one observes the splitting of the various gap types. Please, refer to the text for further details. 75
- 3.10 Plot of α_a as a function of size ratio obtained from the first moment of Monte Carlo simulations. We use the same legend as in Fig. 3.5 78
- 4.1 Scheme of four pattern unit cells. Dashed lines delineate the square lattice unit cells. Adsorption of disks can only take place when their geometrical center lands inside the blue regions. Two parameters characterize the pattern, the size of the cell and the cell-cell separation. 84
- 4.2 A disk fails adsorption onto the substrate because (a) its center does not fall within an allowed-landing cell, or (b) it overlaps with a previously adsorbed disk. 85
- 4.3 The major subdivisions in the two-parameter space. For cell-cell separation $\beta < 1$ we have the *interacting cell-cell adsorption* (ICCA), while for $\beta \geq 1$ we have the *noninteracting cell-cell adsorption* (NICCA). For cell sizes $\alpha < 1/\sqrt{2}$ we have a *single-particle-per-cell adsorption* (SPCA), while for $\alpha \geq 1/\sqrt{2}$ we have *multiparticle-per-cell adsorption* (MPCA). 87

-
- 4.4 Typical configuration of a region of 30×30 unit cells, for $\alpha = 0.6$ and $\beta = 1.2$ at the jammed state. This snapshot corresponds to the NICCA-SPCA, upper-left, region in Fig. 4.3. 90
- 4.5 Typical configuration of a region of 30×30 unit cells, for $\alpha = 1.2$ and $\beta = 1.2$ at the jammed state. Particles attempting adsorption never overlap previously adsorbed ones in different cells, but contrary to Fig. 4.4 each cell can now adsorb more than one particle. Since $\beta = 1.2 > 1$, the kinetics of adsorption at each cell is decoupled from that at other cells. This snapshot corresponds to the NICCA-MPCA, upper-right, region in Fig. 4.3. 91
- 4.6 Coverage values obtained by Monte Carlo simulation of our RSA model (red solid line, the jammed-state coverage) and by direct calculation for the close-packed configurations (green dashed line), both for $\beta = 1$. Notice the discontinuities in the values of the close-packed coverage as opposed to the smooth variation in the RSA case. The jammed-state coverages for $\beta = 2$, calculated according to relation (4.6), are also shown for comparison (blue dotted line). 92
- 4.7 Configuration of a region of 30×30 unit cells, for $\alpha = 0.2$ and $\beta = 0.5$, at the jammed state. A particle attempting adsorption can overlap a previously adsorbed particle in a different cell. This excluded volume interaction is responsible for correlations which result in locally-diagonal, semi-ordered domains as seen in this snapshot. Such snapshots corresponds to the ICCA-SPCA, lower-left, region of the diagram (Fig. 4.3). 97
- 4.8 Configuration of a region of 30×30 unit cells, for $\alpha = 1.2$ and $\beta = 0.2$, at the jammed state. Such snapshots corresponds to the ICCA-MPCA, lower-right, region of the diagram (Fig. 4.3). For this low β value, the probability of a particle attempting adsorption to overlap with one in a neighboring cell is appreciable, thus building up a somewhat longer range diagonal semiordering than that seen for the parameter values of Fig. 4.7. 98

- 4.9 Plots of the distribution function for various values of α , at fixed values of β : (a) $\beta = 1.2$, with $\alpha = 0.2, 0.4, 0.8$, and 1.4 ; (b) $\beta = 0.2$, with $\alpha = 0.2, 0.4$, and 1.2 ; (c) $\beta = 0.8$, with $\alpha = 0.2, 0.4, 0.6$, and 1.2 101
- 4.10 The distribution function (a) for constant $\alpha = 0.2$, with $\beta = 0.2, 0.5, 1.2, 1.4$; (b) for constant $\alpha = 1.2$, with $\beta = 0.2, 0.4, 0.6, 0.8, 1.2$; (c) along the diagonal line $(0, 0) - (1/\sqrt{2}, 1)$ in the ICCA-SPCA region of the (α, β) “phase diagram,” Fig. 4.3, with $(\alpha, \beta) = (0.2, 0.28), (0.3, 0.42), (0.5, 0.70), (0.6, 0.84)$ 101
- 4.11 For ICCA-SPCA, a particle adsorbed in a neighboring cell can constrain particles adsorption on the central cell. For each adsorbed particle there is a “shadowed” region where no other particle center can adsorb. If the overlap of the shadowed regions of the four neighboring particles completely overlap the central cell, there is no minimum finite area available for adsorption and the average number of particles per cell will be less than one. 105
- 4.12 For fixed value of cell size ($\alpha = 0.6$) and different values of the distance between cells ($\beta = \{0.3, 0.4, 0.67, 0.69, 0.71, 0.8, 1.2\}$): (a) Approach of the coverage to the jamming limit as a function of time. (b) Distribution of empty, depositable, areas, before the jammed state. 106
- 4.13 For fixed value of cell-cell separation ($\beta = 0.7$) and different values of the cell size ($\alpha = \{0.2, 0.4, 0.55, 0.59, 0.62, 0.7\}$): (a) Approach of the coverage to the jamming limit as a function of time. (b) Distribution of empty, depositable, areas. 107
- 4.14 Spatial distribution of particles inside the cell, at the jammed state, for $\alpha = 0.6$ and for different values of β : (a) 0.4, (b) 0.5, (c) 0.6, and (d) 0.7. 108
- 4.15 Snapshot of the jammed state with 30×30 unit cells, for $\alpha = 0.6$ and for different values of β : (a) 0.4, (b) 0.5, (c) 0.6, and (d) 0.7. 109

4.16	Spatial distribution of particles inside the cell for $\alpha = 0.6$ and $\beta = 0.7$ for different values of coverage: (a) 80%, (b) 90%, and (c) 99.9% of the jamming coverage.	110
4.17	Scheme of the algorithm.	111
4.18	Snapshot of the system before and after rescaling. The black squares represent the free mesh cells. Without changing the coverage, a rescale of the mesh cell reduce the total area where adsorption attempts take place. . .	117
4.19	Scheme of shadow tests for (a) one particle, (b) two particles, (c) three particles, and (d) four particles. The blue cells are the ones that become shadowed due to the mesh-cell test.	118
4.20	For the irreversible adsorption of monodisperse disks. (a) Coverage, θ_∞ as a function of the linear size of the system. (b) Error of the coverage as a function of the system size.	122
4.21	Coverage as a function of time for adsorption on clean/regular substrates. On clean substrates, adsorption of monodisperse particles for a system size of $L = 4096$ (red solid line) and truncated gaussian-size distributed particles with size dispersion of 1% and $L = 2048$ (green dashed line). Sampled over 10^3 independent runs for the monodisperse case and 10^2 samples for adsorption of particles with truncated gaussian-size distribution.	122
4.22	Run time as a function of substrate area for 10^3 independent runs of monodisperse particles adsorption on clean/regular substrates.	123

- 4.23 Pair correlation function of distance between particles at the jammed state for adsorption on clean/regular substrate. Adsorption of monodisperse particles on a system with size $L = 4096$ (red solid line), binary mixture of particles with size ratio 2 for a system size of $L = 2048$ (blue dashed line), and adsorption of truncated gaussian-size distributed particles with size dispersion of 1% for a system size of $L = 2048$ (green dotted line). Sampled over 10^3 independent runs to the monodisperse and binary mixture cases and 10^2 to the other system. The curves for monodisperse and truncated gaussian-size distribution are almost overlapped. 125
- 4.24 Pair correlation function of distance between particles at the jammed state for adsorption on clean/regular substrate for system sizes ranging from $L = 256$ to $L = 4096$. The logarithmic divergence at $r \rightarrow 1$ is strongly dependent on the system size. Sampled over 10^3 independent runs. 125
- 5.1 Basic cell of 12 lattice sites. The central sites are the initial and final position and the numerated ones are their first and second neighbors. . . . 142
- 5.2 Fundamental processes for Ag/Ag(100). All processes that can take place in the surface are superpositions of these fundamental processes with the terrace diffusion. (a) initial bond break, (b) initial second neighbor (can be one or two), (c) first initial slide neighbor, (d) second initial slide neighbor, (e) first edge neighbor, (f) second edge neighbor, (g) final bond formation, (h) final second neighbor, (i) first final slide neighbor, and (j) second final slide neighbor. 143
- 5.3 Snapshots of a system with 256×256 lattice sites for a coverage of 20%, under different fluxes of incoming atoms: (a) 10^0 ML/s, (b) 10^{-1} ML/s, (c) 10^{-2} ML/s, and (d) 10^{-3} ML/s. 147

-
- 5.4 For different values of the flux: (a) Density of islands (N_{isl}) as a function of the coverage (θ). (b) Density of monomers (N_1) as a function of the coverage (θ). System size of 256×256 lattice sites and results averaged over five samples. Error bars included for each data point. 148
- 5.5 Average island size (s_{av}) as a function of the coverage (θ). System size of 256×256 lattice sites and results averaged over five samples. Error bars included for each data point. 149
- 5.6 Density of islands as a function of the parameter $R_M = \frac{D}{\Phi}$. (a) For values of R_M ranging from 10^{-1} to 10^2 . (b) For higher values of R_M . System size of 256×256 lattice sites and results averaged over five samples. Error bars included for each data point. 150
- 5.7 Average island size as a function of the parameter $R_M = \frac{D}{\Phi}$. (a) For values of R_M ranging from 10^{-1} to 10^2 . (b) For higher values of R_M . System size of 256×256 lattice sites and results averaged over five samples. Error bars included for each data point. 151
- 5.8 Island size distribution for different values of flux obtained for a coverage of 20%. (a) For high values of flux. (b) For low values of flux. System size of 256×256 lattice sites and results averaged over five samples. 152

Part I

Introduction and Theoretical Considerations

Chapter 1

Statistical physics and out-of-equilibrium systems

“Probability is no longer a state of mind due to our ignorance, but the result of the laws of nature.”

I. Prigogine, in *The end of Certainty: Time, Chaos, and the New Laws of Nature*.

Systems made up of many interacting particles have drawn the attention of physicists. Phenomena not predicted from the microscopic interactions emerge, from the collective behavior, at the macroscopic level. Besides, for certain systems, due to the stochastic nature of the phenomena, fluctuations play a relevant role and, therefore, the evolution cannot be predicted solely from the fundamental laws, i.e., randomness needs to be considered. Thus, a statistical description of the possible outcomes is the meaningful approach to the problem in opposition to the deterministic one.

By the end of the nineteenth century, Physics has evolved through two, apparently, unrelated fields of knowledge: the mechanics (classical and, more recently, quantum), characterized by the deterministic description of particles motion, and the thermodynamics, devoted to the study of systems with large degrees of freedom. On one side, the

classical and quantum mechanics are connected with the equations of motion, Hamilton and Schrödinger equation respectively, both characterized by time reversibility [1]. On the other side, thermodynamics is distinguished by irreversibility in the context of its second law [2].

Among the seminal works by James Clerk Maxwell (1831-1879) [3], Josiah Gibbs (1839-1903) [4], Ludwig Boltzmann (1844-1906) [5], and Albert Einstein (1879-1955) [6], among others [7], the field of Statistical Physics emerges. Though the initial main goal was filling the hiatus between the two perspectives referred above, nowadays, the object of study goes much further and, in fact, the description of systems with interacting large degrees of freedom cannot avoid it.

Physically relevant (macroscopic) parameters like pressure, entropy, and temperature, are not due to single atoms but due to an ensemble of atoms [8], therefore it is important to study the collective behavior of such ensemble. In most cases (if not all), the study of the time evolution of all degrees of freedom is either useless or impossible (or even both). Besides, most systems are not deterministic, they can evolve from a given initial state through multiple ways out. Consequently, a deterministic description has revealed unable to track most multiparticles systems and, consequently, statistical descriptions have become a reliable approach [1, 7].

Despite the extensive work, in the literature, about equilibrium systems, such systems are more an exception than a rule. Observing nature we realize that systems are constantly affected by external factors that keep the system away from equilibrium, yielding out of equilibrium. Thus, structures are kinetically trapped and equilibrium configurations are not achieved. The study of the time evolution of a system is fundamental to the understanding of its structure. The first remarkable results are due to L. Onsager¹ [9, 10], which focus on systems close to stable configurations. In the follow up, a lot of work has been done in the fast growing field of out-of-equilibrium systems, with special focus on the far-from-equilibrium ones where the linear relations proposed by Onsager do not any

¹Lars Onsager have received the Nobel Prize in Chemistry, in 1968, due to this striking work.

longer apply².

Another contribution to this field came from the observation that, different systems with different types of interaction, share similar phenomena, leading to the concept of *universality classes*. This means that, for certain emerging properties, the detailed description of local interactions is not relevant. Such observation thrust physicists in an interesting and interdisciplinary journey through distinct fields [12, 13, 14, 15], not only dealing with lifeless components like, e.g., materials science [16] and geology [12], but also biology [17], neurology [18], sociology [19, 20, 21], and economy [22, 23, 24, 25]. Despite the huge number of variables involved in such systems, simple models have been developed to explain global behaviors.

In this work, we address the formation of films on top of substrates. The advance of experimental techniques has improved our ability to observe, as well as control, processes at a smaller length scale. Since the desirable structures are small and usually difficult to prepare in a fully controlled manner, it is necessary to understand how to achieve them through self-organization. Therefore, interest has shifted toward the control of the system properties through growth parameters like, e.g., temperature, flux of incoming particles, and reactivity of the substrate. On that ground, identification of the relevant mechanisms which affect the system morphology is essential. Yet, how each identified mechanism affects the evolution of the system is also pertinent.

We attempt to answer some rising questions about such systems like, e.g., the effect of both the substrate morphology and mobility on the film structure. We develop a set of theoretical models to mimic the growth of films under different conditions. Using theoretical oriented methodologies, it is possible to control the considered conditions to characterize, in an effective way, the influence of each process on the overall dynamics.

Film growth can occur in a close or an open system. In a close system, the total amount of deposited material is preserved and it, eventually, achieves the thermodynamic equilibrium. In an open system, the most common, deposition is present. Competition

²It is beyond the scope of this work to review the historical evolution of the field. For such, see, e.g., [11, 7].

between deposition and relaxation mechanisms keeps the system out of equilibrium. Thus, the obtained structures, even when a steady state is attained, do not correspond to the equilibrium ones but are, instead, determined by the growth kinetics. This thesis is devoted to the latter systems yielding out-of-equilibrium conditions.

Based on the system at hand, as well as on the properties we intend to address, different levels of detail, are required. For example, when particles attempting adsorption are much larger than the atoms of the substrate, the periodic-lattice structure of the substrate becomes irrelevant. On the other hand, for other type of problems, the periodicity of the lattice is fundamental. For those cases, an atomistic description of the system accounts for the necessary length scale to understand the relevant phenomena. Notwithstanding, as discussed within the present chapter and in Chapter 5, even for such systems a detailed description of thermal vibrations of each atom is superfluous.

We consider two different growth limits. In the first one, landing particles, interacting solely through excluded volume, stick irreversibly, yielding the random sequential adsorption process (Part II). On the second case, an atomistic description of the film growth is considered (Part III). Atoms are deposited on a crystalline substrate and are able to diffuse on top of it. The thesis is, then, divided in three different parts: *Introduction and Theoretical Considerations*, *Micro- to Nano-scale*, and *Down to the Atomic Scale*. The first part is devoted to the scientific background of this work and includes the first two chapters. In the present one we start with a brief review of statistical physics, followed by a discussion, in Chapter 2, of the computational methods applied in the field. It is not our intention to provide a full review of the subject but to summarize the main definitions, theories, and methods used throughout the document. In Part II, adsorption is considered in the limit where adsorbing particles are much larger than the ones from the substrate, therefore a decoupling of length scales between the adsorption process and atomic bonds can be done (Chapters 3 and 4). Chapter 3 is devoted to the adsorption of segments on a line, while Chapter 4 is devoted to the effect of a patterned substrate on the adsorption of disks on a surface. The Part III is dedicated to the study of thin-films growth, where

an atomistic description of the deposition process is required. Specifically, we study the effect of the deposition rate on the morphology of the film.

The goal of the present chapter is to give a brief introduction to the field of statistical physics and build a scientific scaffold of concepts and methods to support the remaining chapters. We start by introducing the concept of phase space to represent the system configurations, followed by a brief description of the Hamilton's dynamics as well as the way to Liouville's equation, in order to describe the time evolution of a set of possible initial configurations. Through the analysis of the typical time scales in a system consisting of an adatom on a crystalline substrate, the concept of infrequent events is introduced. We discuss, as well, how the employment of decoupling time scales can lead to a simplification of the problem being addressed. Since the deterministic description is not suitable to study the majority of systems with large degrees of freedom, the concept of stochastic processes is presented and the phenomenological description of physical systems discussed, with special focus to the Langevin dynamics and a general formulation using the Master equation. To finalize, the concept of scaling and universality is also presented, opening the door to the use of simplified models, where only the main features are included, to mimic more complex systems. Using two deposition models, random and ballistic deposition, we show that, despite the degree of simplification, relevant properties can be caught.

1.1 Phase space, state vector, phase functions

In the field of Statistical Physics, as stated previously, we deal with an ensemble of particles (e.g., atoms or molecules) and how some properties emerge from the microscopic dynamics. With that aim, it is important to bridge from the microstate to the correspondent macrostate. In this section, concepts like phase space, state vector, and phase functions are defined and considered to differ these two types of states (micro and macro).

A mechanical system is defined by the set of generalized coordinates (q_i) of each particle and the corresponding generalized momenta (p_i) [26, 27]. For sake of simplicity and

convenience, from now on, q and p represent, respectively, the set of all generalized coordinates and momenta. A system with f degrees of freedom has f generalized coordinates and f generalized momenta, i.e., the $2f$ parameters, $\{q, p\}$, completely define the system configuration. Therefore, a $2f$ -dimensional Euclidean system [4, 28], named phase space, can be used to define the set of all possible system configurations. A particular state can then be represented, in the phase space, by a $2f$ -dimensional state vector [29], \vec{X} , defined as

$$\vec{X} = \vec{X}(q, p) . \quad (1.1)$$

The experimentally measured physical parameters, such as temperature, pressure, and entropy, are due to the ensemble of particles, being a function of the state [8], therefore we can also define each physical parameter as a function F over the phase space, named space function [30], where

$$F = F(\vec{X}) . \quad (1.2)$$

At this point, it is relevant to differ microstate from macrostate. A microstate is completely defined by the corresponding state vector and a macrostate is defined by a set of phase functions. Therefore, is straightforward to conclude that each microscopic configuration corresponds to a single macroscopic parameter (value of the space function) but, the same macroscopic parameter can be related with multiple microscopic states (state vectors). These concepts are fundamental in Statistical Physics since it is the map from the microstates to macrostates that allows us to understand large scale behaviors from the microscale dynamics. For example, according to a fundamental principle in equilibrium statistical physics, named ergodic principle (see, e.g., [28, 30]), for an isolated ergodic system, in equilibrium, all the accessible microstates (with the same energy) are equally probable. But, at the same time, when we look into nature we conclude that, even for systems in equilibrium, different macrostates occur with different probabilities. Why? Since the phase functions are additive functions of large degrees of freedom [30], the number of microstates related to a given macrostate differ from state to state (macro). There-

fore, different macrostates occur with different probabilities. Looking to the microstate dynamics, systems are always changing from state to state and, consequently, moving in the phase space. However, on the macrostate level, the physical parameters (state functions) are not, necessarily, time dependent. In the next section we discuss the concepts of equilibrium and out-of-equilibrium systems. For the latter one, two different types are presented, namely, non- and far-from-equilibrium systems.

1.2 Equilibrium vs out of equilibrium

Thermodynamics was the first field of knowledge dedicated to the study of large ensembles of particles. Such discipline is mainly devoted to those systems whose the full set of macroscopic parameters (phase functions) does not change in time or, for finite systems, each parameter is characterized by small fluctuations around the mean value (thermodynamic value). Those systems are said to be in equilibrium.

Looking into nature we rarely observe equilibrium. Year after year, global growth of population is reported. Weather is changing (temperature, pressure, ...) and differs from place to place. Flux of energy, from the Sun to the Earth, leads to irreversible chemical reactions with fundamental relevance in biological activity. Life is itself a proof of a system out of equilibrium. Therefore, equilibrium is more an exception than a rule [1, 31]. Nature is, undeniably, out of equilibrium. It is beyond the scope of this thesis to discuss why nature is out of equilibrium. Such philosophical question is discussed in several different places (see, e.g., [11]). For our purpose, we just recognize that nature is out of equilibrium and, once in a while (rarely), some local equilibrium is found.

Out-of-equilibrium systems can be of two main types: nonequilibrium or far from equilibrium [32]. Nonequilibrium occurs when an external parameter acts over the system keeping it away from equilibrium [33]. A gradient is obtained and, even if we wait “infinite” time, the system does not fall into the equilibrium state. In fact, it converges to a steady state, the one with lowest rate of entropy production, which is characterized by a stability

similar to the equilibrium one. When the system is slightly perturbed from such state, it returns to the steady state and the perturbation smears out. Onsager made several contributions to the study of this type of systems [9, 10]. He proposed a linear relation between the driving force and the thermodynamic flux to equilibrium. Following such consideration it was possible to study properties like correlations and the kinetic approach to the steady state.

Far-from-equilibrium systems are in an unstable state and, once released, they “flow” to the equilibrium one. In a more general way, such systems can be constantly kept out of equilibrium due to exchange of matter and energy with the surrounding and, therefore, yielding nonequilibrium conditions. However, it is important to stress that a far-from-equilibrium system is not, necessarily, a nonequilibrium one. Thermodynamic parameters, like pressure and temperature, can only be defined locally. The linear relations proposed by Onsager are not valid for far-from-equilibrium systems [7]. Therefore, it is difficult/impossible to attempt a deterministic description of the system evolution.

In the next section, we discuss how to describe the time evolution of a multicomponent system, with special focus on the deterministic description and its limitations.

1.3 From Hamilton's dynamics to Liouville's equation

A state vector, \vec{X} , defines a particular microstate of a system and geometrically localizes it in the phase space. The system can also be visualized as a point in the phase space, defined by the state vector. If the Hamiltonian of the system is known, $\mathcal{H}(\vec{X}, t)$, the system time evolution can be described with the Hamilton equations [26, 27, 34],

$$\dot{p}_i = -\frac{\partial \mathcal{H}}{\partial q_i} \quad (1.3)$$

and

$$\dot{q}_i = \frac{\partial \mathcal{H}}{\partial p_i} , \quad (1.4)$$

where the dot stands for the time derivative.

The solution of the equations written above leads to a deterministic description of the particles motion and, consequently, to a well defined trajectory of the system state in the phase space. To be successful it is important to know the Hamiltonian of the system and to be able to identify its initial state (with infinite precision). So far, let us consider that the former condition is attained and focus on the latter one. In the quantum limit, it is well known that, according to Heisenberg theory (see, e.g. [35]), uncertainty is intrinsic to the system, being not just related to the complex nature of it, occurring also for the simplest one [36]. But even for classical systems, it is impractical to measure the dynamical state of all particles in the system [37] and, if we could do it, there is no experimental setup with which it is possible to obtain such states with infinite precision. However, such limitation in classical systems is not only due to the lack of knowledge from the observer [31]. Two different factors are related to such limitation: the stability of the system and its integrability. If two trajectories, initial close to each other, diverge, the system is classified of unstable (e.g., chaotic systems), otherwise, it is stable [1]. Besides, Poincaré classified physical systems into integrable and non-integrable, where the non-integrable systems are characterized by resonance between degrees of freedom. These systems cannot be described deterministically and the concept of trajectory has no meaning. The non-integrable case is the typical one for systems with many-particles characterized by non-linear interactions [7].

When an experimental setup is prepared, the initial configuration (set of phase functions) is compatible with multiple microstates. Therefore, instead of describing the evolution of a point in the phase space it is preferable to study the evolution of a set of points. The concept of trajectory in the phase space gives place to a time evolution description of the “cloud” of possible states [11]. To that end, we define a phase-space density $\rho(\vec{X}, t)$, such that $\rho(\vec{X}, t)d\vec{X}$ is the probability of finding the system, at time t , in the hyper-cube

$[\vec{X}, \vec{X} + d\vec{X}]$ of the phase space [2, 38].

To describe the evolution of the phase-space density, in a deterministic way, it is important to analyze its time evolution. Since the phase-space density is related with a probability³ (where a conservation law applies to the total probability), let us consider the continuity equation

$$\frac{\partial \rho}{\partial t} + \vec{\nabla} \cdot (\dot{\vec{X}} \rho) = 0 \quad . \quad (1.5)$$

Expanding the equation we have

$$\frac{\partial \rho}{\partial t} = - \sum_{i=1}^f \left[\rho \left(\frac{\partial \dot{q}_i}{\partial q_i} + \frac{\partial \dot{p}_i}{\partial p_i} \right) + \left(\frac{\partial \rho}{\partial q_i} \dot{q}_i + \frac{\partial \rho}{\partial p_i} \dot{p}_i \right) \right] \quad . \quad (1.6)$$

According to Hamilton theory (from eqs. (1.3) and (1.4)),

$$\frac{\partial \dot{q}_i}{\partial q_i} = - \frac{\partial \dot{p}_i}{\partial p_i} \quad , \quad (1.7)$$

so, considering eqs. (1.6) and (1.7),

$$\left(\frac{\partial \rho}{\partial t} \right)_{q,p} = - \sum_i \left(\frac{\partial \rho}{\partial q_i} \dot{q}_i + \frac{\partial \rho}{\partial p_i} \dot{p}_i \right) \quad , \quad (1.8)$$

which is the so called Liouville's equation [2, 26, 28, 29, 30, 34, 37, 38]. It corresponds to a deterministic description of the “cloud” of the most probable states. The same equation can be re-written, for sake of simplicity, as a function of the Poisson brackets of the phase-space density and the Hamiltonian (see, e.g., [34]),

$$\left(\frac{\partial \rho}{\partial t} \right)_{q,p} = - \{ \rho, \mathcal{H} \} \quad . \quad (1.9)$$

Note that, even with such equation (Liouville's equation), to study a certain physical system we need to be able to write the Hamiltonian of the system or, at least, know how

³A large number of points in the phase space are considered such that the continuum approach is valid.

to relate the space density with q and p . As it is discussed below, the concept of stochastic systems will lead to a more appropriated description.

1.4 Energy landscape

As discussed above, it is unfeasible to study certain multicomponent systems in a deterministic way. In the case of thin films, by picturing the energy landscape, we realize that different phenomena occur at different time scales and, therefore, decoupling of such scales can be employed to simplify the problem solving. Therefore, it is important to pick the relevant parameters to consider in order to attempt a probabilistic description of the system.

Consider the diffusion of atoms on a crystalline substrate. The substrate, typically, consists on a periodic arrangement of atoms distributed in an array according to the geometry of the lattice. The potential energy landscape for the diffusing atom consists on multiple basins separated by barriers, which are much higher than the typical thermal energy ($k_B T$). The energy difference between the top of the barrier and the basin is the activation energy (E_a). Once in a basin, the adatom vibrates to and fro in all directions and exchanges energy with the substrate. Eventually, due to thermal fluctuations, the vibrating atom acquires enough energy to climb across the barrier and hops to another basin. Since the energy barrier is much larger than the typical thermal energy ($k_B T$), it is reasonable to assume that the adatom stays at a given basin, enough time to attain local equilibrium with the substrate. If such is true, since the substrate can be seen as a thermal bath, the energy distribution is in agreement with the canonical distribution (Boltzmann distribution). Due to the thermalization process, memory of the previous states is lost, and the transition to the next one only depends on the actual state (Markov process). Consequently, Transition State Theory (TST) can be applied.

According to the harmonic Transition State Theory, the rate of a given transition is

given by Arrhenius equation

$$\nu = \nu_0 \exp\left(-\frac{E_a}{k_B T}\right), \quad (1.10)$$

where ν_0 is the attempt frequency (related with the vibration of the adatom in the basin). As an example, consider the diffusion of an adatom of silver in a (100) silver surface⁴. To make a single hop, an isolated atom, needs to cross an activation barrier of 0.48 eV [39]. The typical attempt frequency is 10^{13} s^{-1} [40]. At room temperature, $T = 298 \text{ K}$, the typical resting time of an atom in the basin is then $\tau_{\text{diff}} \approx 10^{-5} \text{ s}$, according to eq. (1.10). However, the vibration time is $\tau_{\text{vibration}} \approx 10^{-13} \text{ s}$. This way, the system is characterized by vibrating atoms that, once in a while, hop between different neighboring basins. For each trial (vibration event), the probability of a successful transition is low, therefore, the event of transition is named infrequent event⁵, being a Poisson process in time [2].

The time scale of vibration and hopping can be decoupled. Such decoupling can be used to simplify the problem solving, instead of fully trace the vibration, the probability of each transition between basins can be computed and the possible directions of the hop considered⁶. This example is a potential application of the stochastic idea discussed forward. Instead of mimicking all the dynamics (vibration), a stochastic model is considered where processes (transitions) occur accordingly to a probability distribution function. Note that, the choice of the main details to take account for in the system description, is always related with the properties under study. For example, in Chapter 5, we apply the time scale decoupling to study the island size distribution for submonolayer growth of Ag/Ag(100), where the detailed description of the vibration is irrelevant.

1.5 Stochastic processes

For most cases, if not all of them, the treatment of all variables returns much more information than the one needed to solve a specific problem. Moreover, as discussed

⁴The homoepitaxial growth of Ag/Ag(100) is discussed in the context of the Chapter 5.

⁵Also known as rare events [16].

⁶The probability for each direction only depends on the activation energy of each process.

above, such treatment can easily become impracticable. To overshoot such obstacle it is important to reduce the number of considered degrees of freedom. That can be achieved by selecting the variables which, instead of being fully treated, can be averaged and only consider their distributions. Such treatment is known as coarse grain approximation.

After picking the variables that can be integrated it is necessary to compute their distribution, which can be done from the output of an experiment or from phenomenological considerations. Therefore, due to the nature of these variables, they are named stochastic variables. A process written in terms of stochastic variables is, consequently, denoted stochastic process [36, 38, 41, 42].

In the present section we discuss the stochastic processes in the context of the Langevin dynamics and of the general Master equation.

1.5.1 Langevin equation

To introduce stochastic systems and understand their relevance, focus on the Brownian motion problem. In 1827, the botanist Robert Brown, observed that large particles (pollen particles) in a fluid (e.g., water), make a characteristic random motion. This have called the attention of many scientists, who attempt to explain it as well as use such motion to argue in favor of the atomistic theory of matter [43].

Consider a large particle inside a fluid. To fully describe the system we need to be able to write the Hamiltonian of the system and the initial configuration of all particles: the Brownian particle and the ones from the fluid. Since our purpose is the description of the large particle, let us consider its velocity, $v(t)$, and attempt a phenomenological description of the collisions with the particles from the medium. The forces exerted by the medium can be represented by two components. A slowly varying force that drags the system to the equilibrium configuration, represented by a damping term linear in the velocity, $-\gamma v(t)$, and a fast varying force, mimicking the thermal noise, represented by the noise term, $\eta(t)$.

Regarding the noise term, since there is no preferential direction during collisions, as

well as no spatial dependence

$$\langle \eta(t) \rangle = 0 \quad , \quad (1.11)$$

where $\langle \dots \rangle$ represents the average over an ensemble of particles. Besides, $\eta(t)$ is rapidly varying in time [2, 36] so the correlation function can be written as

$$\langle \eta(t)\eta(t') \rangle = \Gamma \delta(t-t') \quad , \quad (1.12)$$

where Γ is a constant to be computed later on and $\delta(t-t')$ is the Dirac delta function. Such correlation function means that the collisions correlation time is zero⁷ so, two consecutive collisions, are uncorrelated. For those cases, the noise is classified as white noise.

The equation of motion for the Brownian particle is the following Langevin equation,

$$m\dot{v}(t) = -\gamma v(t) + \eta(t) \quad . \quad (1.13)$$

For simplicity we define $\gamma' = \gamma/m$ and $\eta'(t) = \eta(t)/m$, so the equation of motion becomes

$$\dot{v}(t) = -\gamma' v(t) + \eta'(t) \quad . \quad (1.14)$$

Solving the previous equation and averaging over an ensemble of particles the following result is obtained for the mean velocity,

$$\langle v(t) \rangle = \langle v(0) \exp(-\gamma't) \rangle \quad , \quad (1.15)$$

where $v(0)$ is the initial velocity, and for the mean square velocity,

$$\langle v^2(t) \rangle = \langle v^2(0) \exp(-2\gamma't) \rangle + \frac{\Gamma}{2\gamma'} (1 - \exp(-2\gamma't)) \quad . \quad (1.16)$$

For large values of time, equilibrium is attained and the canonical ensemble needs to

⁷Stochastic processes without memory are also known as Markovian processes.

be recovered [4], i.e., according to equipartition theorem [2],

$$\langle v^2(\infty) \rangle = \frac{k_B T}{m} , \quad (1.17)$$

where k_B is the Boltzmann constant. On that ground,

$$\Gamma = \frac{k_B T}{m} 2\gamma' . \quad (1.18)$$

This relation is called fluctuation-dissipation since it relates the strength of the noise (Γ) with the friction coefficient (γ) [44].

The previous example shows that, the Langevin equation can be used to describe a system where certain variables are averaged. Specifically, the description of the collision process is reduced to the use of the mean value and correlation function of the noise term. For certain systems, either the noise term is position dependent or the damping term is non-linear (or both), leading to a problem with much higher complexity [36].

1.5.2 Master equation

The study of stochastic systems implies some phenomenological approaches. When the detail of the full system dynamics is not important and attention is focused on transitions between accessible states, the Master equation plays a relevant role [44].

A Master equation describes the population, $P_s(t)$, of a given state s . The system is considered to be Markovian, i.e., transition only depends on the actual configuration and not on its entire history [29]. The time evolution contains gain contributions (transitions from other states, r , to the considered state) and loss contributions due to transitions from the state to other states. Generically,

$$\frac{d}{dt} P_s(t) = \sum_r W_{rs} P_r(t) - \sum_r W_{sr} P_s(t) , \quad (1.19)$$

where W_{rs} is the transition rate from state r to state s . Under equilibrium conditions,

the population of each state is time independent,

$$\frac{d}{dt}P_s(t) = 0 \quad . \quad (1.20)$$

The trivial solution is then

$$P_r W_{rs} = P_s W_{sr} \quad , \quad (1.21)$$

known as detailed balance. Note that, other solutions can also exist but, for equilibrium problems, only the properties at the equilibrium state are important, and the detailed balance condition leads to the proper distribution.

The detailed balance condition allows to compute relations between transitions in order to guarantee a certain distribution at the equilibrium state. Let us consider two typical equilibrium ensembles: the microcanonical and the canonical. The microcanonical ensemble is an isolated system. As referred before, according to the fundamental postulate of statistical mechanics [2, 34], for an isolated system, with energy $E + \delta E$, all microstates are equally probable, $P_s = P_r$. Therefore, from the detailed balance, eq. (1.21),

$$W_{rs} = W_{sr} \quad . \quad (1.22)$$

The canonical ensemble is a closed system in contact with a heat reservoir. In equilibrium, the probability distribution of each state shall follow the Boltzmann distribution, meaning that it is related with the energy of the state, such that,

$$P_i \propto \exp\left(-\frac{E_i}{k_B T}\right) \quad . \quad (1.23)$$

On that ground,

$$\frac{W_{rs}}{W_{sr}} = \exp\left(-\frac{E_s - E_r}{k_B T}\right) \quad . \quad (1.24)$$

The conditions discussed above are only valid when the system is in thermodynamic equilibrium. When the system is out of equilibrium, for certain conditions, detailed bal-

ance can be broken [32]. For example, consider the adsorption of colloidal particles on a substrate⁸. For such system, after particles adsorption, the time scale for desorption is much larger than the typical experimental time scale. Therefore, the detailed balance condition can be broken, by neglecting the desorption process, without leading to any bias in the study.

The analytical solution of the Master equation is not a straightforward process. Two type of obstacles are common, the definition of the proper transition probabilities, specially for out-of-equilibrium systems, and solving the set of equations. In the next chapter we discuss the use of Monte Carlo methods to computationally solve such equations.

1.6 Statistical-physics growth models

As stated previously, solving the deterministic equations is, usually, more than a hard task. In fact, in most cases, it is an impossible one. Therefore, instead of following a detailed treatment it is preferable to make coarse grain approximations leading to a significant reduction of the number of degrees of freedom. As it is discussed in the next section, different systems share some kind of universality [45], i.e., not all the details are important to grasp the most relevant phenomena in the system.

The main idea in physics is to build models [46, 47, 48], as simple as possible, to describe the physical system. Models are sets of phenomenological rules that try to grab the fundamental properties of a system (or class of systems). Such models shall be simpler to solve, either analytically or numerically, than the deterministic one. Despite simple, models should not loose the relevant features. As discussed in the next chapter as well as in the remaining of the thesis, computational approaches have a fundamental role in the study of such models.

To develop a model for a certain system, two different points of view can be followed. It is possible to build a model where all features, considered relevant, are included and

⁸The adsorption process is discussed in the context of the Part II.

study what emerges from this set of rules, or create models through a sequence of steps. At each step, one feature is included and the effect of such feature studied carefully. With such methodology, it is possible to understand the relevance of each added rule.

Throughout this thesis different models are referred. Not all the models are considered with the same level of deepness. In this section we discuss two different models related with growth phenomena: Eden and Diffusion-limited aggregation. They have historical relevance in statistical physics, since are among the first ones to deal with kinetic structures. When out-of-equilibrium aggregation is considered, the history of the system (memory) is relevant, because the obtained structures are the kinetic ones. On the other hand, in the thermodynamic equilibrium growth, the obtained structures are not history dependent. These models show that out-of-equilibrium growth conditions lead to different morphologies when compared with the ones obtained under equilibrium conditions⁹ [50, 51, 52, 53]. In the next section, two deposition models, Random Deposition and Ballistic Deposition, are introduced to discuss the concepts of Universality and Scaling. In the next chapter, two different models are discussed: percolation model and Ising model. The former one is a static model dealing with critical concentrations of active material leading to connected paths that spread all over the system. The latter is related with the interaction between magnetic spins. This is an equilibrium model, but it is important in the field of statistical physics since it is characterized by a phase transition in 2D, has an analytical solution presented by Onsager [54], and different systems, magnetic and non-magnetic ones, can be mapped to such model [55, 56]. In the next part of the thesis, a generalized version of the random sequential adsorption model is presented. Such model have been proved to mimic fundamental properties characterizing the irreversible adsorption of particles on surfaces. And, in the last part, we introduce our own model to study homoepitaxial growth of Ag/Ag(100).

⁹With Renormalization-Group theory, H. Gould, F. Family and H. E. Stanley, proved that equilibrium growth and kinetic growth have different growth statistics [49].

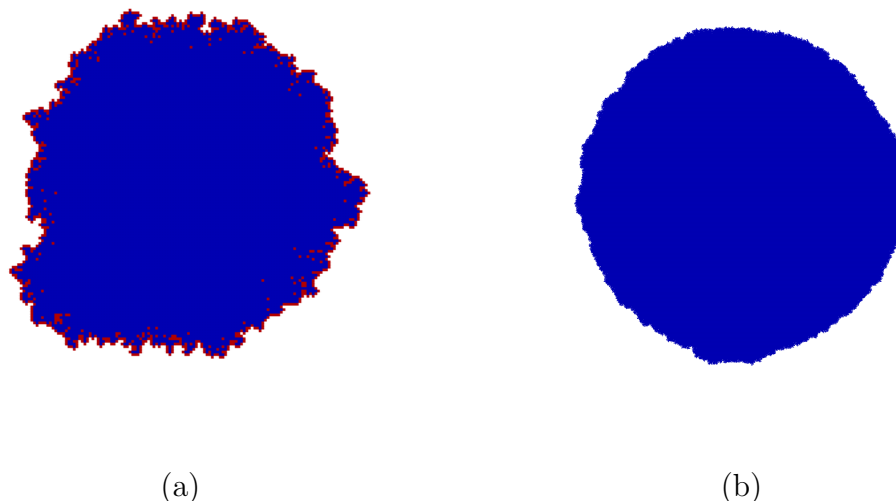


Figure 1.1: Snapshots of Eden model. (a) Aggregate with 12 000 particles (the red sites are the active ones). (b) Aggregate with 1 200 000 particles.

1.6.1 Eden growth model

In 1960, M. Eden has presented a model to study growth phenomena [57]. Such model, now known as Eden growth model, is characterized by random accumulation of matter in the interface of a cluster. It can be used to study different growth phenomena like: growth of bacteria colony, fire propagation, and aggregation with relaxation.

In the Eden Growth model the system is initialized with an occupied site in the center. At each iteration, one empty site in the neighborhood of an occupied one, is randomly chosen. The state of the chosen site is converted from empty to occupied. The process is repeated till a limiting number of iterations. Such model leads to compact clusters. In Fig. 1.1(a) is an aggregate with 12 000 particles. The red sites are the reactive ones. By reactive we mean that are the sites where the next particle can aggregate. In Fig. 1.1(b) is an aggregate with 1 200 000 particles. As we can observe, the obtained structure is compact and invariant under rotation.

Different variants of this model can be presented. For example, if the system under study is a fire propagation, it is more accurate to select an active site with neighboring

empty ones instead of a reactive one. This approach favors (higher probability of becoming active) sites with more than one active neighbor.

Despite being a geometrical growth model, since the kinetics only depends on the structure [53], the strong dependence on the history of growth, make it difficult to study with analytical methods. Notwithstanding, its computational implementation is simple.

1.6.2 Diffusion-limited aggregation

Under out-of-equilibrium conditions, since the system does not have enough time to relax between two different deposition events, the history becomes relevant. We now consider the Diffusion-limited aggregation model (DLA). We intend to emphasize that different deposition conditions lead to morphologically different structures.

According to the Diffusion-limited aggregation model, the system is initialized with an occupied site in the center (seed). For each iteration, a particle is injected far from the aggregate and diffuses (random walk). When the diffusing particle touch the aggregate it sticks, irreversibly, to it and become immobile. Another particle is then injected.

In Fig. 1.2(a) is a typical aggregate obtained with this model, with 500 particles. In Fig. 1.2(b) is an aggregate with 50 000 particles. In opposition with the Eden model, where a compact aggregate is obtained, with DLA screening effect is observed. The aggregate is characterized by a set of branches where screening effect is observed. The density of the aggregate decreases with the increasing size (number of particles) [58].

With Figs. 1.1 and 1.2 it is possible to conclude that the obtained structures, with these two different models, are fundamentally different. Once again, we stress a strong dependence on the deposition conditions.

1.7 Scaling and universality

One of the main goals in physics is to find how to relate the variables of the system (at least some) to obtain general rules [45]. In 1945, Guggenheim [59] showed that, when

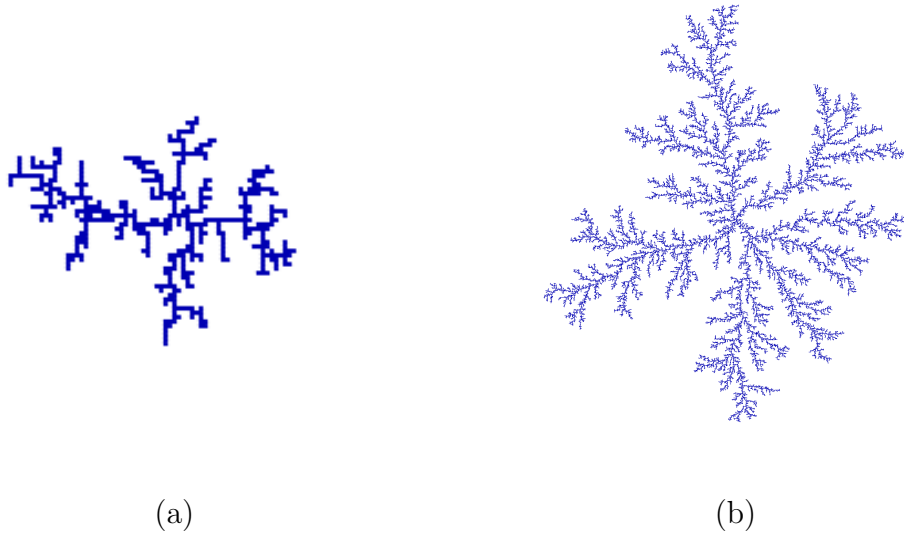


Figure 1.2: Snapshots of Diffusion-limited aggregation (DLA) model. (a) Aggregate with 500 particles. (b) Aggregate with 50 000 particles.

T/T_c is plotted as a function of ρ/ρ_c , where T and ρ are, respectively, the temperature and the density, for eight different fluids, the obtained curve is the same¹⁰. Despite different interactions between the particles, when T and ρ are rescaled according to the respective critical values, such differences become irrelevant [46], revealing a kind of universality between systems with different interactions. Near the critical point, the correlation length diverges being much larger than the interaction length scale. For such regime, the weight of short interactions on the global behavior decreases [12, 29] and some properties become not dependent on the interaction detail.

According to the scaling idea, thermodynamic functions, in the asymptotic limit, are homogeneous functions of their distance to the critical point (ϵ) [29, 60]. If $F(\epsilon)$ is an homogeneous function, then

$$F(\mu\epsilon) = g(\mu)F(\epsilon) \quad , \quad (1.25)$$

¹⁰The index c stands for the critical values, which are obtained at the critical point, where the transition from liquid to gas occurs.

i.e.,

$$F(\epsilon) = A\epsilon^\zeta \quad . \quad (1.26)$$

In his paper, Guggenheim, showed that, if we make

$$\epsilon = |\rho - \rho_c|/\rho_c \quad (1.27)$$

and

$$F(\epsilon) = |T(\epsilon) - T_c|/T_c \quad , \quad (1.28)$$

then $\zeta = 1/3$, i.e., different liquids have the same exponent ζ [29].

Many different systems, apparently unrelated, have shown to have similar behaviors. The concept of *universality* was then introduced [61]. The group of systems sharing the same set of exponents are members of the same *universality class* [32]. Studies reveal that only few factors are relevant to the exponent [16] and that relations between exponents can be obtained from heuristic arguments or Renormalization Group calculations [33, 62, 63]. The advantage of *universality* concept is that not all the systems need to be fully studied. Instead, some conclusions obtained with a given system can be extended to other systems from the same *universality class*. Therefore, complex systems can be mapped to less complex ones, from the same *class*, without loss of relevant information [32, 64]. In fact, statistical physics models, make use of universality to describe complex phenomena of the real world, based on simplified models [46].

The first results have been obtained for equilibrium conditions, but the concept of *universality* can be extended to out-of-equilibrium systems [16, 32]. To discuss the concept of *universality classes* out of equilibrium we consider two different growth models: Random Deposition (RD) and Ballistic Deposition (BD). Interesting problems related with growth have been address by physicists [16, 32, 64, 65]. A relevant subject to account for during the study of such systems is the use of scaling theory to study finite-size effects [63, 66]. When the system size is much larger than the correlation length, no finite-size effects are expected to occur (no dependence on the system size). But, on the other hand, if

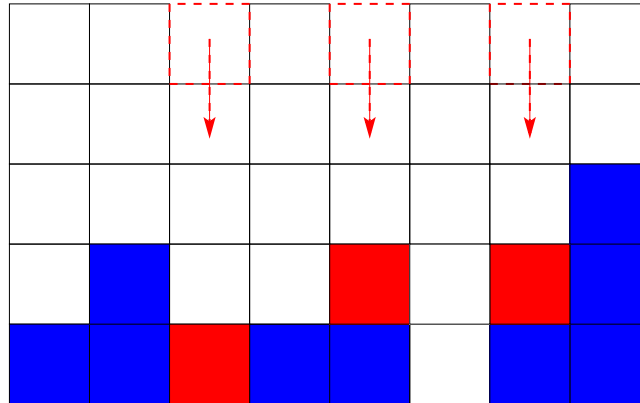


Figure 1.3: Rules for the Random Deposition model.

the correlation length is much larger than the system size, as expected at the criticality of a continuum phase transition (correlation length diverges), strong dependence on the system size is observed [66]. Scaling functions to consider the finite-size effect are discussed below, in the context of the Ballistic Deposition model.

1.7.1 Scaling law for the Random Deposition model

The Random Deposition (RD) model is the simplest growth model [16, 32]. Consists in a (1+1)-dimensional model where a discrete lattice is considered as a substrate. Particles are randomly deposited all over the lattice without any kind of lateral interaction.

Consider a linear lattice with size L , in units of the lattice parameter. For each time step, L particles are randomly deposited. In Fig. 1.3 are summarized the deposition rules. A snapshot of a system with $L = 500$ after the deposition of 500 particle layers is in Fig. 1.4(a). Color changes for each 100 layers. It is possible to observe that the interface roughness (noise) grows with the number of layers.

When we deal with interface properties is important to characterize the surface. Let

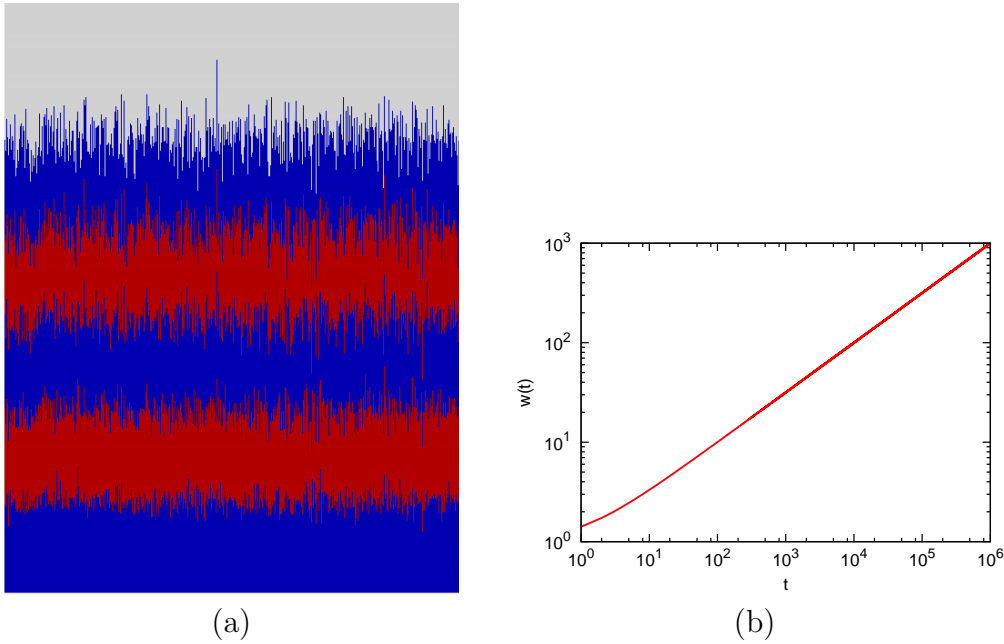


Figure 1.4: (a) Snapshot for Random Deposition model on a linear lattice with size 500 after the deposition of 500 layers. Color changes for each 100 layers. (b) For Random Deposition model on a linear lattice with size 10^3 , roughness as a function of time (measured in terms of deposited layers). Results sampled over 10^3 samples.

us define $h(i, t)$ as the height of the column i at time t . The mean height is then given by,

$$\langle h(t, L) \rangle = \frac{\sum_{i=1}^L h(i, t)}{L} , \quad (1.29)$$

and the interface width (roughness), w , given by

$$w^2(t, L) = \langle (h(i, t) - \langle h(t, L) \rangle)^2 \rangle = \frac{\sum_{i=1}^L (h(i, t) - \langle h(t, L) \rangle)^2}{L} . \quad (1.30)$$

For the RD model the surface roughness grows with time according to a power law,

$$w(L, t) \sim t^{\bar{\beta}} , \quad (1.31)$$

where the exponent $\tilde{\beta}$ is the growth exponent [32]. In Fig. 1.4(b) is the interface roughness (eq. (1.30)) as a function of time for a system with $L = 10^3$. Results have been sampled over 10^3 samples. The value of $\tilde{\beta}$ computed with such results is 0.500. Since the deposition is completely random, without any local interaction, such exponent can also be analytically obtained (see, e.g., [16]). In the lack of lateral correlations, the roughness is expected to grow indefinitely without any saturation limit. Contrarily, in the case of the BD model (discussed in the next section), due to the lateral interaction, finite systems are characterized by a saturation roughness.

1.7.2 Ballistic deposition

To go ahead with the discussion of the scaling idea we use the Ballistic Deposition model. This model is also for (1+1)-dimensional growth and have been initial proposed to study the properties of colloidal aggregates with porous. The interest in it comes from the lateral correlations developed during the growth process.

As in the RD, the substrate is considered to be a linear lattice with size L in units of lattice constants. At each step, L iterations are performed. An iteration consists in randomly chose a column and release a particle at the top of the chosen column (far from the substrate). The released particle falls straight into the surface and aggregates as soon as it finds a neighboring occupied site. In Fig. 1.5 are summarized the deposition rules.

In Fig. 1.6(a) is a snapshot of a system with $L = 500$ after the deposition of 500 layers. Color changes for each 100 layers. When compared with the RD model (see Fig. 1.4(a)), we observe that, due to the lateral interactions, for BD model, porous are obtained during film growth. Therefore, the density of the film is expected to be lower. With the color scheme is also possible to observe that, the growth of the roughness with the number of deposited layers is weaker in BD model than in RD model. In the Ballistic Deposition model, any contribution to the roughness due to a fluctuation in the height of a given column, can be smoothed out by particles deposited on neighboring columns.

In Fig. 1.6(b) is the roughness as a function of time for a system size of 4096 lattice sites.

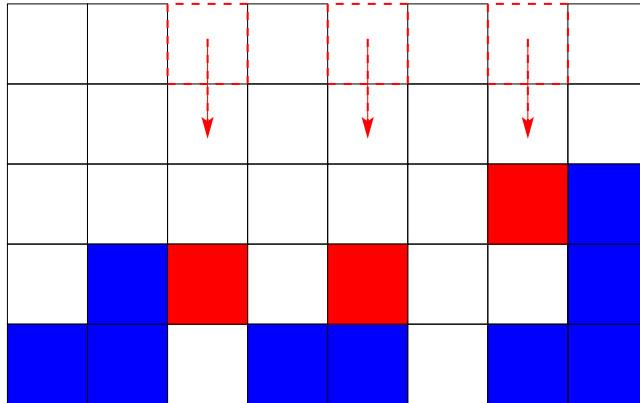


Figure 1.5: Rules for the Ballistic Deposition model.

Such function is characterized by three different regimes. A first regime, characterized by uncorrelated deposition of particles in the substrate, where the growth exponent, $\tilde{\beta}$, is $1/2$, as expected for the Random Deposition (see previous section). A second regime, where a competition occurs between the noise (deposition) and the relaxation. If, due to fluctuations, a column grows more than the neighboring ones, the increase in the roughness is smeared by particles aggregation at neighboring sites. Such regime is characterized by $\tilde{\beta} = 1/3$. The third regime is characterized by a saturation value of the interface roughness. The system “gets to know” that is inside a box and, due to the system finite size, a saturation roughness, w_{sat} , is attained. The latter regime is a finite size effect, therefore, for the infinite system, such regime is not present.

For the purpose of this section we focus on the second and the third regime. The transition between this two regimes occur for $t = t_x$, where t_x is the crossover time. If the third regime occurs due to the finite size of the system, both the saturation roughness, w_{sat} , and the crossover time, t_x , are expected to scale with the system size. In Fig. 1.6(c) the saturation roughness scales as,

$$w_{sat}(L) \sim L^{\tilde{\alpha}} \quad (1.32)$$

where $\tilde{\alpha}$ is the roughness exponent, equal to $1/2$. In Fig. 1.6(d) the crossover time scales

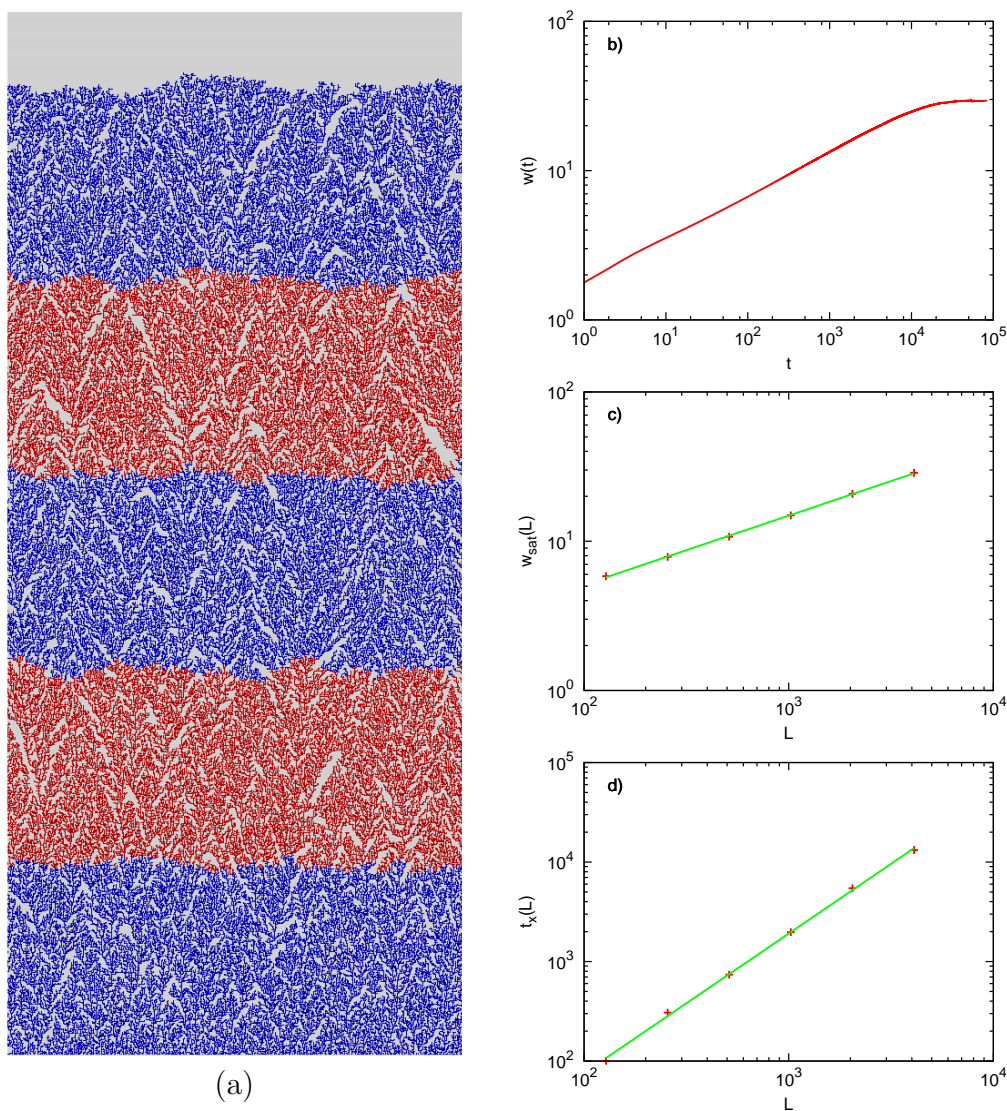


Figure 1.6: (a) Snapshot for Ballistic Deposition model on a linear lattice with size 500 after the deposition of 500 layers. Color changes for each 100 layers. (b) Interface roughness as a function of time for a system size of 4096. (c) Saturation roughness as a function of system size. (d) Crossover time as a function of system size. All the results were averaged over 10^4 samples.

as,

$$t_{\times}(L) \sim L^z \quad (1.33)$$

where z is the dynamic exponent, equal to $2/3$. The dependence of such exponents on the system size was studied recently (see e.g., [67]).

It is also interesting to find scaling laws between exponents. According to eq. (1.31), at the crossover time, $w(L, t_{\times}) \sim t_{\times}^{\tilde{\beta}}$. However, according to eq. (1.32), $w_{sat}(L) \sim L^{\tilde{\alpha}}$. Since, $w(L, t_{\times}) = w_{sat}(L)$, we conclude that,

$$z = \frac{\tilde{\alpha}}{\tilde{\beta}} . \quad (1.34)$$

Back again to the roughness as a function of time (see Fig. 1.6(b)), the obtained curve, for different system sizes, are qualitative similar, but the transition between different regimes occurs for different values of crossover time and, therefore, for different values of saturation roughness. A scaling function f can, then, be defined such that

$$\frac{w(L, t)}{w_{sat}(L)} \sim f\left(\frac{t}{t_{\times}}\right) . \quad (1.35)$$

On that ground, according to eqs. 1.32 and 1.33,

$$w(L, t) \sim L^{\tilde{\alpha}} f\left(\frac{t}{L^z}\right) . \quad (1.36)$$

The scaling function obtained for different system sizes is in Fig. 1.7.

The Ballistic Deposition model belongs to the Kardar-Parisi-Zhang (KPZ) universality class [68]. It is interesting to note that, despite apparently different, the Eden model belongs to the same *universality class*. The KPZ class is characterized by the following set of exponents,

$$\tilde{\alpha} = 1/2 \quad , \quad \tilde{\beta} = 1/3 \quad , \quad \text{and} \quad z = 2/3 \quad . \quad (1.37)$$

The bottom line of the present chapter is that, for most systems, with many degrees of

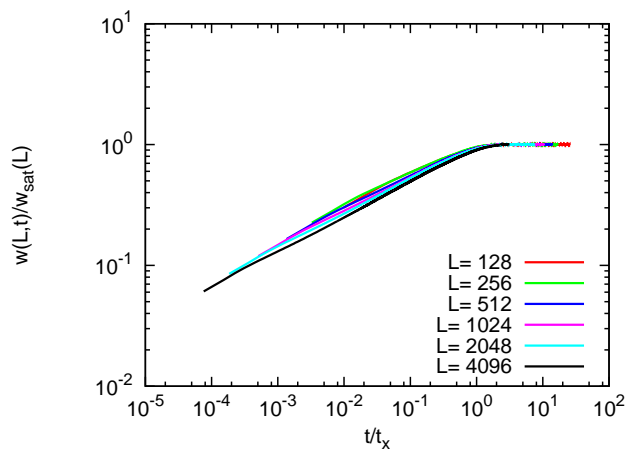


Figure 1.7: Plot of the scaling function for different values of system size.

freedom, the statistical description is the meaningful one. Therefore, stochastic variables need to be defined to reduce the number of degrees of freedom in the problem. Recall also that, it is possible to build simplified models to mimic the behavior of more complex systems from the same *universality class*. In the next chapter, we discuss the use of computational methods to study such systems.

Chapter 2

Computational methods in statistical physics

“The basic theorem of interdisciplinary research states: physicists not only know everything, they know everything better. This theorem is wrong, it is valid only for computational statistical physicists like me.”

D. Stauffer, in *Introduction to statistical physics outside physics*.

As discussed in the previous chapter, the study of systems with many particles interacting with each other is a far-from-easy task. To understand a system, it is important to analyze how each factor, or set of factors, affects the global behavior. Therefore, it is necessary to fix all the variables in the system (named controlled variables) and change only the one that we intend to characterize the relevance.

For centuries, physicists follow two different approaches to study Nature: experiments and theory. The experimental approach consists in the observation of phenomena in the field or under controlled experimental conditions. The main obstacle is related with the control of all the parameters that affect the system behavior. On the other hand, when theoretical approaches are considered, simple models are developed to study a given

system (see previous chapter). Such methodology allows, in principle, to control all system parameters.

Only a small fraction of theoretical models have been solved analytically [69], the Achilles' heel of analytical methods is their limitation to oversimplified models. With the electronic computer, came the possibility of making more instruction per unit of time than the human, pencil and paper, capability. Therefore new doors have been opened for the scientific research, not only being able to bridge between theory and experiment, through the resolution of equations obtained with analytical techniques, but also giving the opportunity to study Nature through more complex models where oversimplification is avoided. In fact, simulation has become a source of interesting problems in science [16, 56].

David P. Landau and Kurt Binder [56] summarize the role of simulation in research with the triangle schematized in Fig. 2.1. In the vertices of the triangle are the three methodologies: theory, experiment, and simulations, and in the center the object of study, Nature. Simulation can be used to test models, previously developed by theory, and to compare the obtained results with the experimental ones, paving the way between theory and experiment. Through it, it is also possible to directly analyze Nature and give information to guide experiments and theoretical models. It plays also a relevant role in the development of such models, since parameters can be tuned like, e.g., the interaction energy or the rate of each process, to fit experimental results¹ [70].

Since the advent of the electronic computer, many techniques have been developed to study natural phenomena. Based on the type of problem under study, it is important to define what are the time and length scales where the relevant processes occur. It is such definition which determines the necessary level of detail and, consequently, the most tailored technique to carry out the analysis. Therefore, models and techniques shall be optimized according to the problem at hand.

Since different physical phenomena occur at different time and length scales, Bris-

¹The use of simulation to test and redefine a theoretical model can become a tricky task since, in principle, it is always possible to fit the model to a given experimental result.

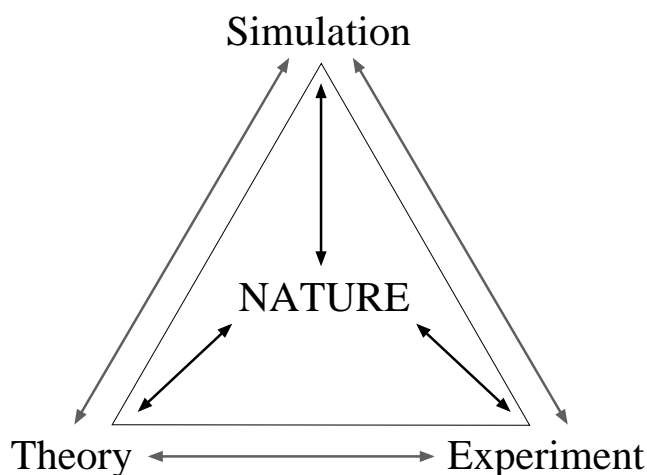


Figure 2.1: Relationship between theory, experiment, and computer simulations. From David P. Landau and Kurt Binder. [56]

towe and Hasnip [47, 71], hierarchize the modeling methods into four different regimes: electronic, atomic, microstructural, and continuum. Such regimes are addressed in the following paragraphs.

The electronic regime methods [72] are typically devoted to the resolution of the quantum equation, i.e., Schrödinger equation. With such methods, it is possible to study properties like, e.g., the atomic equilibrium positions, the configuration energy, the band structure, the density of states, and the charge distribution. Inside the electronic regime, the most well known techniques are the Density-Functional Theory (DFT) and the Quantum Monte Carlo (QMC). Another relevant technique is related with the coupling of electronic description, obtained through DFT, with the classical description of atomic motion characteristic of the Molecular Dynamics method. Such approach is named Car-Parrinello Molecular Dynamics, after the authors who first worked on it, R. Car and M. Parrinello [73]. The level of detail needed to study the electronic regime limits the feasible system sizes to several hundred atoms.

Methods classified in the atomic regime [70, 74, 75, 76, 77], are related with the analysis of phenomena like atomic motion, formation of defects, diffusion, and phase transitions. Therefore, properties like diffusion paths and correlation functions need to be measured,

which requires time scales larger than the ones allowed by electronic description. To reduce the computational effort, instead of explicitly consider all the quantum phenomena, it is preferable to neglect them and use semi-empirical interatomic potentials to account for the interaction between particles. Such potentials can be parametrized to fit previously measured experimental results. Once defined the interatomic potential, the description of atomic motion can be done through the resolution of the Newton equations of motion, through a technique known as Molecular Dynamics [70, 76]. Another possible approach is to build models with phenomenological rules where the effect of quantum interactions is considered. Doing so, a stochastic description of the system is attempted. The method tailored for such description is the Monte Carlo method [55]. Since the expensive task of electronic properties calculation is avoided, it is possible to consider up-to a billion atoms.

For certain problems instead of attempting an atomistic description is preferable to consider the behavior of sets of atoms. The regime where a set of atoms is considered is denoted as microstructural regime. The system is divided into domains where physical quantities assume the same value inside each one and are limited to a set of possible values/states (based on “cellular automata”). The evolution of each one follows an interaction dynamics or rule. The Ising Monte Carlo model [56], considered later in this chapter is an example of such regime. With such coarse grain approach thousands of domains can be considered.

Phenomena like elastic properties and heat conduction, within certain limits, can be studied through a continuum approximation. In the continuum regime, instead of account for a description of the individual elements of the system, all the system is considered as a continuum. Differential equations are solved to describe the system behavior. Typically, to solve such equations, the system is discretized with a mesh cell and the equations are solved for each one (with boundary conditions). The mesh cell is created in such a way that, the density of cells can increase around areas of particular importance. Examples of this set of methods are the finite elements and the finite difference methods.

More recently [47], multiscale modeling has been considered to describe systems where

relevant phenomena occur at different time and length scales. The idea is to use different methods to solve problems at different scales. For example, it is possible to use electronic methods to compute forces at a certain region of a material and treat the remaining parts with continuum methods. The big challenge of multiscale modeling is related with the choice of the best way to proceed in the interface between different techniques.

Nonetheless, the algorithm to implement a given model is also relevant. It needs to be as efficient as possible [48]. In the history of computer simulations, development of algorithms has been playing a more relevant role than the computer power evolution [56]. The strategy consists in diminish, as much as possible, the number of “irrelevant” instructions leading to a significant reduction in the required computer effort.

In the present chapter we focus the discussion on the Monte Carlo method. Special attention is devoted to this method since it is the one used intensively in the remaining of the thesis. During the discussion we try to emphasize relevant aspects of simulation in Statistical Physics like the influence of the system size and of the number of samples.

2.1 The Monte Carlo method

A probabilistic description of a system is, not only more practical, but also the most accurate way to treat systems with interaction between different degrees of freedom. This type of systems are stochastic in nature, meaning that the effect of certain degrees of freedom shall be analyzed as stochastic variables whose the output follows a particular probability distribution. Monte Carlo (MC) methods, related with the use of a random number generator², are the computational techniques fitted to make such probabilistic description [55].

In 1945, close to the end of the World War II, at the *Los Alamos National Laboratory*, Nicholas Metropolis and co-workers [78], under the consulting of John von Neumann, started to work on a method suitable to the, under development, first electronic computer,

²Formally, since a deterministic algorithm is used to generate “random” numbers, such generator is denoted pseudo random.

named ENIAC. Later, Stanislaw Ulam joined the group [78, 79], and proposed the development of a technique based on statistical sampling. Such methodology was unpopular, at that time, due to the boring task of its calculations. But, with the advent of electronic computer, such long and tedious operations could be done, in a straight manner by it.

In 1949, Metropolis and Ulam [80], published a paper where the “new” method was introduced and coined as Monte Carlo (MC) method. The method is named after the Monte Carlo city in the Principality of Monaco. This connection is related with the casino activity that makes such city famous. But even before that, under the name of statistical sampling, the basic principles of MC method were known. Already in the eighteenth century, a French mathematician, named Georges-Louis Leclerc, *Comte de Buffon*, proposed that the value of π could be estimated by randomly throwing needles to a ground with, equally separated, parallel lines [48].

Hammersley and Handscomb [81] split the applications of the MC techniques into probabilistic and deterministic problems. The former are mainly devoted to the study of stochastic processes, which are problems, intrinsically, random. In the latter case, when, despite being deterministic, the theory is not able to solve the problem, MC can be used to obtain a numerical approach. An example of such, is the use of MC to compute integrals. The technique proved to have special relevance for high dimensional integrals [48, 55]. This set of techniques is, usually, named Monte Carlo Integration [74].

The use of MC techniques to study stochastic systems can be of two different types [48, 74]: direct or based on Markov-chain Monte Carlo. In the former, a direct implementation of the model is performed with uncorrelated configurations. In the latter, configurations are generated according to a Markov-chain, i.e., each new configuration is obtained from the previous one. These two types of generating samples are discussed below.

In the present section, we focus on the use of MC method to study stochastic systems. The main idea is to generate different configurations and compute the average of system properties. The challenge of generating samples according to the proper distribution is discussed in the context of the next subsection.

2.1.1 Standard Monte Carlo

As stated previously, the main idea of MC is to generate different configurations aiming to compute the mean value and distribution of certain properties (observables) on the phase space. Consider a given observable (a phase function, see Chapter 1), $\mathcal{O}(t)$. If we intend to analyze what is the mean value of such observable in the phase space, we need to compute the following integral,

$$\langle \mathcal{O}(t) \rangle = \frac{\int \mathcal{O}(\vec{X}, t) \rho(\vec{X}, t) d\vec{X}}{\int \rho(\vec{X}, t) d\vec{X}} . \quad (2.1)$$

Since it is impossible to directly evaluate the integral, the idea of MC method is to approach such integral by a summation [48],

$$\langle \mathcal{O}(t) \rangle \approx \frac{1}{N} \sum_{i=1}^N \mathcal{O}_i(t) , \quad (2.2)$$

where N is the total number of analyzed configurations. For a large value of N the summation (2.2) converges to the integral (2.1).

To compute the average value of a given observable with the summation referred above, it is important to generate samples with the proper weight. Therefore, the MC technique consists in randomly generate configurations in the phase space, according to a given distribution. A set of random numbers is obtained and used as inputs to further logical operations [70], which makes the method suitable to study stochastic systems through computer simulations.

The proposed sampling techniques can be divided into two different groups: the simple sampling and the importance sampling. Below, both methodologies are discussed. Simple sampling in the context of the percolation model and importance sampling in the context of the Ising model.

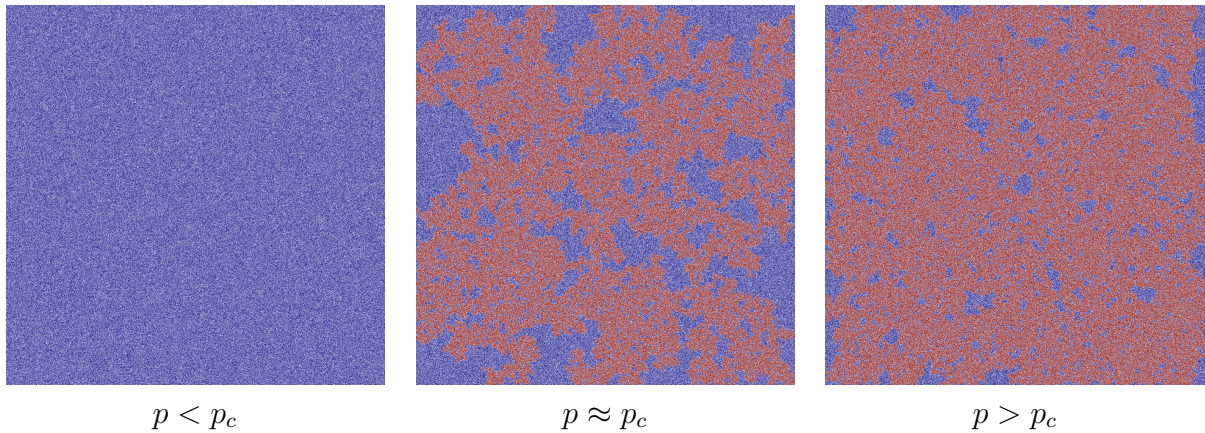


Figure 2.2: Snapshots of percolation model for a square lattice with 4 million lattice sites: before, near, and above the percolation threshold.

Simple sampling: the percolation model

One interesting problem that have called the attention of physicists is the diffusion of liquids in porous medium. Such problem can be addressed through the well known percolation model [82]. Other systems can also be studied with this model like, e.g., the fraction of porous leading to connectivity or the critical concentration of conductive material necessary for conduction. The interest in the percolation model [83] is related with its critical behavior and long-range correlations near criticality.

Consider a square lattice with linear size L (L^2 unit cells). Each lattice site is occupied with probability p and, consequently, empty with probability $1 - p$. What is the critical value of such probability, $p = p_c$, leading to a connected cluster which spans the entire lattice? [56]

In Fig. 2.2 are snapshots of a square lattice with 4 million lattice sites, for three different values of occupation probability: before, near, and above the percolation threshold. With such set of snapshots it is possible to conclude that the percolation cluster, near criticality, is a non-compact cluster.

The main goal of percolation theory is to identify the percolation threshold. Each possible configuration of the lattice has exactly the same probability, therefore, the easiest

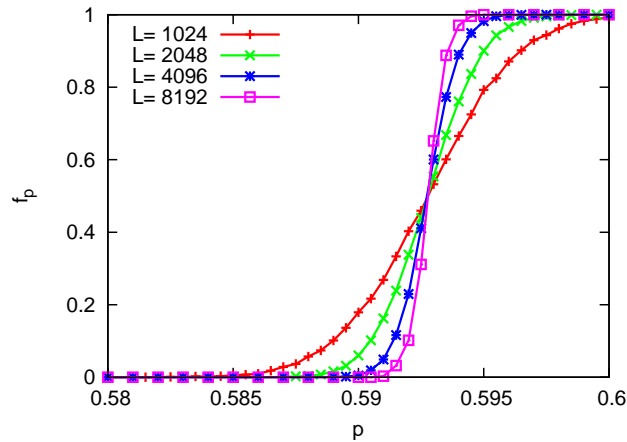


Figure 2.3: Fraction of samples with percolation clusters (f_p) as a function of occupation probability, p , for different linear system sizes, L , namely, 1024, 2048, 4096, and 8192. Results average over 10^4 samples.

way is to generate different samples (configurations) where each site is occupied with probability p and compute the fraction of configurations with a percolation cluster³, f_p . Doing so, for different values of p , it is possible to estimate p_c . Formally, the procedure consists on computing the summation (2.2) where the observable can take two different values. It is equal to one when a percolation cluster exist and zero otherwise.

In Fig. 2.3 are the fraction of configurations with a percolation cluster, f_p , for different system sizes. Results have been averaged over 10^4 samples. With these results we observe that even a simple model like this develops a strong dependence on the system size. So, it is always important to analyze how the system behaves with the size.

The described sampling technique, where different samples are generated in an uncorrelated way, is named simple sampling. As discussed below, for many systems, this is not the proper way of sampling in an efficient manner like, e.g., when different samples have not the same weight to the average, i.e., different configurations occur with different probabilities.

³Clusters can be identified with the Hoshen-Kopelman algorithm [84].

Importance sampling: the Ising model

Recall, from the previous chapter, that according to a fundamental principle of Statistical Physics, for an isolated system, in equilibrium, all the accessible states occur with equal probability. For such systems, the simple sampling technique described above is able to do the job. Samples are generated in an uncorrelated way, with equal probability for each one. However, for certain problems, like a system in contact with a heat reservoir, the probability of each configuration depends on its total energy. Therefore, different configurations occur with different probabilities. Another sampling technique is then required. To discuss further this topic consider the, well known, Ising model. Despite being an equilibrium model, it is taken here as an example, to discuss importance sampling, due to its relevance in the field of equilibrium statistical physics.

Consider a system with spins interacting according to the following Hamiltonian,

$$\mathcal{H} = - \sum_{i,j} J_{ij} \sigma_i \sigma_j - H \sum_i \sigma_i \quad , \quad (2.3)$$

where σ_i and σ_j are the spins and can take the values ± 1 . J_{ij} is related with the strength of the exchange interaction between spin i and spin j and H is the external field. Since interaction between spins decreases with the distance let us consider the summation $\{i, j\}$ only over the first neighbors [2]. For the propose of this section, let us take, also, the simplest case of zero field, i.e., $H = 0$.

Different values of J_{ij} lead to different types of interactions [2]. For $J_{ij} > 0$, the interaction energy is lower when the spins are aligned (parallel). This interaction is coined ferromagnetic interaction. On the other hand, for $J_{ij} < 0$ the interaction energy is lower when the spins are antiparallel, named antiferromagnetic interaction. In the noninteracting case, $J_{ij} = 0$.

If a ferromagnetic system is in equilibrium with a heat reservoir, at temperature T (canonical system), according to the Hamiltonian (2.3), it is possible to predict that, for values of the temperature such that, the thermal energy is much lower than the interaction

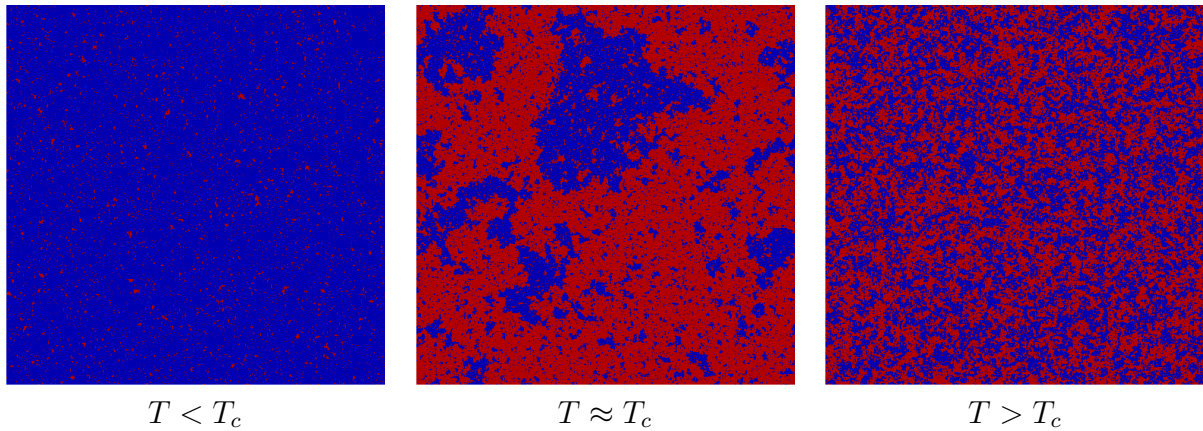


Figure 2.4: Snapshots of the equilibrium configuration for the Ising model: below, near, and above the critical temperature. System with 250 thousand spins interacting according to the Hamiltonian of eq. (2.3). Obtained after L^2 Monte Carlo steps.

energy, the equilibrium configuration of this system is characterized by aligned spins. However, as the temperature rises, the thermal energy becomes dominant and the strength of the interaction insignificant. The system is then characterized by random spins. Such transition occurs for a given critical temperature, T_c .

In Fig. 2.4 are snapshots of typical configurations obtained with the Ising model. Three different temperatures are considered: below, near, and above the critical temperature. Snapshots were obtained for a system size of 250 thousand spins, organized in a square lattice, and after 250 thousand Monte Carlo steps. We remark that, below the critical temperature spins are mainly aligned, since it corresponds to the configuration with the minimal energy. Near the critical temperature, large domains of aligned spins are obtained. Such domains span all over the system. Above the critical temperature, as temperature increases, the thermal energy leads to noise in the system and cooperative effects are not observed.

The Ising model, named after Ernst Ising, who has studied it, in 1924, in the context of his PhD thesis, was first proposed by Wilhelm Lenz⁴, in 1920. The model called the attention of physicists due to its phase transition, occurring at $d = 2$ (not observed at

⁴Wilhelm Lenz was professor of Ernst Ising at the University of Hamburg.

$d = 1$), and played a relevant role in the development of statistical physics techniques. In 1944, L. Onsager [54] has proposed an analytical solution for this model, for $d = 2$, that allows to identify the critical temperature at which the transition occurs.

In principle, the Ising model could be sampled with simple sampling technique. Since different configurations have different weights for the summation (2.2), when simple sampling is considered, each contribution needs to be weighted accordingly. For a system in contact with a heat reservoir, such contribution is given by the Boltzmann factor,

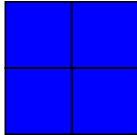
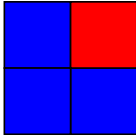
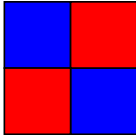
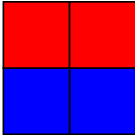
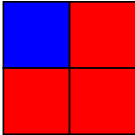
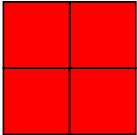
$$\rho(\vec{X}, t) \sim \exp\left(-\frac{H(\vec{X}, t)}{k_B T}\right) . \quad (2.4)$$

However, an uniform random generation of configurations can imply a huge number of samples to converge the summation (2.2) to the integral (2.1).

Consider a square lattice with 2×2 Ising spins with periodic boundary conditions. The total number of possible configurations is $2^4 = 16$. In Table 2.1 are summarized the six different groups of configurations, the fraction of the total configurations belonging to each group, and the Boltzmann factor. Configurations can be divided into six different groups. In fact, due to the up-down symmetry the first group is equivalent to the last one and the second group is equivalent to the fourth one. If samples are generated in an uncorrelated way, like with the simple sampling technique, the configurations which contribute most to the summation (greater Boltzmann factor) are the ones with lower probability of being generated. Therefore, a different sampling technique is needed. Note that, at high temperature, all the Boltzmann factors converge to 1, which means, almost, equal probability for all configurations, and, consequently, the simple sampling can keep doing a good job.

The idea is to randomly generate configurations according to a distribution that allows to concentrate the evaluation of the function in the region where the contribution to the integral is more important [70]. If we consider the system Markovian, i.e., without memory from its past, as expected for an equilibrium model, the evolution of the system can be

Table 2.1: Scheme of all possible configurations in a 2×2 square lattice of Ising spins. For such system $2^4 = 16$ different configurations are possible. For each scheme is the fraction of configurations as well as the Boltzmann factor obtained by considering periodic boundary conditions and an exchange interaction J . The parameter γ_T is defined as $\exp\left(\frac{J}{k_B T}\right)$.

Scheme						
fraction	$\frac{1}{16}$	$\frac{4}{16}$	$\frac{2}{16}$	$\frac{4}{16}$	$\frac{4}{16}$	$\frac{1}{16}$
Boltzmann factor	γ_T^{16}	1	γ_T^{-16}	1	1	γ_T^{16}

described by a Markov-chain based on the Master equation (see eq. (1.19), from previous chapter, and respective discussion). The Master equation is then,

$$\frac{d}{dt}P_s(t) = \sum_r W_{rs}P_r(t) - \sum_r W_{sr}P_s(t) . \quad (2.5)$$

Recall that $P_s(t)$ is the population of the state s and W_{rs} the transition probability from state r to state s . According to the detailed balance condition, for a system in equilibrium with a thermal reservoir,

$$\frac{W_{rs}}{W_{sr}} = \exp\left(-\frac{E_r - E_s}{k_B T}\right) , \quad (2.6)$$

which is the eq. (1.24) from previous chapter. In 1953, N. Metropolis and co-workers [85], proposed the following set of transition rates, leading to what is now known as the Metropolis algorithm,

$$W_{ij} = \exp\left(-\frac{\Delta E}{k_B T}\right) \quad (2.7)$$

$$W_{ji} = 1 \quad (2.8)$$

where $\Delta E = E_j - E_i$ and $E_j \geq E_i$. At this point, it is important to stress that the stochastic trajectory, obtained through the Master equation, with this set of transition rates, does not describe properly the time evolution of the physical system [56, 86, 87]. Recall that our intention is to compute the equilibrium properties of the Ising model and not to characterize the evolution toward equilibrium. Since detailed balance is taken, we only guarantee that the relative weight between configurations is respected. As it is discussed forward, for the proper time description of the system evolution, other transition rates are required.

To apply Metropolis algorithm to the Ising model, for each iteration a spin is chosen randomly. The value of the difference in energy, ΔE , for the spin-flip possibility, is measured. If a spin-flip leads to a decrease in the total energy, $\Delta E < 0$, the transition is accepted with probability 1. Otherwise, if $\Delta E \geq 0$ the transition occurs with a probability obtained with W_{ij} in (2.7). A random number, Y_p , is generated uniformly between 0 and 1 and the transition is accepted if the generated number is lower than the probability, this is

$$Y_p < W_{ij} \quad . \quad (2.9)$$

Time is incremented by $1/L^2$, where L^2 is the total number of spins in the system. The time unit is the Monte Carlo step (MCS).

With Metropolis algorithm, for the purpose of losing memory from the initial configuration, a significant number of “warm-up” iterations need to be performed before starting with the measurements. The first set of steps drags the system to the equilibrium configuration and the following ones describe the fluctuations around equilibrium. Enough time (number of iterations) between different measurements shall be given to avoid correlations. After a MCS, L^2 iterations occur but that does not mean that all the spins were tested for flipping. There is always a correlation between consecutive configurations. A correlation time can be measured which gives the typical time of correlation between states.

It is also important to note that, at high temperature, $W_{ij} \rightarrow W_{ji} = 1$. Therefore,

for each Monte Carlo step all the L^2 spins tested for flipping are changed which means that Metropolis algorithm becomes non-ergodic, since not all possible configurations are accessible and the obtained ones are strongly correlated with the previous states.

Another problem with the implementation of the Ising model is related with the transition probabilities at low temperature. According to the Boltzmann factor (2.4), for low values of temperature, the transition probabilities are low. Therefore, following the methodology described above, most transitions are rejected. In 1975, Bortz and co-workers [88], proposed a different algorithm to avoid such computational bottleneck. Below, we discuss such algorithm as well as the methodologies to properly describe the time evolution of the system.

2.1.2 Kinetic Monte Carlo

In the standard Monte Carlo method, with Metropolis algorithm, the number of rejected transitions increases both with the decrease of the temperature and approach to equilibrium [56]. Besides, the stochastic trajectories obtained through the resolution of the Master equation, with the transition rates (2.7) and (2.8), do not properly describe the time evolution of the system [86, 87, 89]. In the present section we intend to address these two problems.

Aware of the former problem, in 1975, Bortz, Kalos, and Lebowitz [88], proposed a new, rejection free, algorithm for the simulation of Ising spins. The algorithm is coined N -fold way since sites are classified into N different classes, based on their transition probabilities. Each class corresponds to a possible process. For each iteration, the number Q_i is computed for each possible transition, such that,

$$Q_i = \sum_{j=1}^i n_j W_j \quad , \quad (2.10)$$

where n_j is the number of spins in class j and W_j the transition rate of such process. A

random number Y_p is generated and the next transition i is picked, such that,

$$Q_{i-1} \leq Y_p < Q_i \quad . \quad (2.11)$$

With the present algorithm, all the trials are accepted, no rejection occurs, leading to an increase in the algorithm efficiency.

To obtain the same stochastic trajectory and time evolution of the standard method, time needs to be incremented in the appropriate way. Consider the time increment Δt . Let us also define $P(\Delta t)$ as the probability of no transition in the interval Δt after the previous transition. The probability of having a transition in the interval dt is Rdt , where R is the total rate of events, obtained from,

$$R = \sum_{i=1}^N n_i W_i \quad . \quad (2.12)$$

The probability of transition in the interval $[\Delta t, \Delta t + dt]$ is proportional to the probability of no transition during Δt , $P(\Delta t)$, and the probability of transition in the interval dt . Therefore, the probability of no transition in $\Delta t + dt$ is given by

$$P(\Delta t + dt) = P(\Delta t) - P(\Delta t)Rdt \quad . \quad (2.13)$$

Solving the equation above, we obtain,

$$P(\Delta t) = \exp(-R\Delta t) \quad , \quad (2.14)$$

and so,

$$\Delta t = -\frac{1}{R} \ln(1 - Y_t) \quad , \quad (2.15)$$

where Y_t is a random number, uniformly distributed, in the interval $[0, 1[$.

The second problem referred above is related with the description of the time evolution. Solving the Master equation with the transition rates proposed by Metropolis, does not

describe properly the system time evolution [86, 87, 89]. Recall that the obtained rates were computed from the detailed balance and the distribution of states in equilibrium, given by the Boltzmann distribution. Consequently, such rates only guarantee the proper weight for each configuration in equilibrium. It is common to, wrongly, associate the Monte Carlo steps with the enhanced time between transitions in the “real” system [89]. Such consideration is far from realistic, since the transition rates, from Metropolis method, only guarantee that detailed balance is respected. When equilibrium is considered, the main goal is to compute averages over the phase space, i.e., as far as the right weight for each sample is taken, the sequence of events is not relevant. In fact, as explained before, the algorithm shall be able to converge to the equilibrium configuration with the minimum number of iterations. However, as discussed with different models in the previous chapter like, e.g., *Diffusion-limited aggregation* and *Eden growth model*, out-of-equilibrium structures can only be understood through a study of the system kinetic evolution. The obtained configurations are no longer the ones with lower thermodynamic energy, named, thermodynamic configurations but, instead, the kinetic ones. A proper description of the time evolution is required to understand the obtained kinetically trapped structures. It is important to develop methods able to follow the time evolution of the system. The set of Monte Carlo methods where time evolution is relevant are coined kinetic Monte Carlo methods⁵.

The algorithm proposed by Bortz and co-workers is tailored to study kinetic evolution, regarding that the proper set of transition rates is considered. Selecting the proper transition rates to describe the time evolution of the system under study becomes the main challenge during model development. Let us start by considering the simplest case of systems with only one process ($N = 1$). As examples, we have models of deposition without relaxation like *Diffusion-limited aggregation*, *Ballistic Deposition*, and *Random Sequential Adsorption*. Since only one process occurs (deposition), it is possible to measure the time in units of particles arriving to the substrate (deposited ones) and relate

⁵In the literature, specially in the field of chemistry, is also common to find the designation of Dynamic Monte Carlo methods [90].

with physical time through the flux of deposition since, by definition, the flux of deposition is the number of particles arriving to the substrate, per unit time, per unit area.

When more than one process is considered the accurate transition rates becomes a non-trivial issue. Two different methodologies can be followed. A more heuristic one, consisting on the use of phenomenological arguments to tune the transition rates to fit experimental results. Another possibility is to compute the activation energy of each possible transition and respective attempt frequency and, subsequently, use such values to compute the transition rates with harmonic Transition State theory [91]. The activation energy can be computed with different methods, for example: regular Molecular Dynamics with saddle search methods [92, 93, 94, 95], first principles with Density Functional Theory (DFT) [96], and empirical potentials methods like embedded atom (EAM) [39, 40, 97]. To compute the attempt frequency the Vineyard method can be used [98]. We would like to stress that, more important than consider the proper transition rate is to consider the right relation between rates.

One interesting example, addressed in the present thesis, is the island nucleation and growth on crystalline substrates. Atoms are deposited on the substrate with a flux F and are able to diffuse in the substrate. If the activation barrier E_a of diffusive processes is known and much higher than the thermal energy, $k_B T$, since diffusion is a thermal activated process, transition rates can be computed with Arrhenius equation (as explained in the previous chapter) [75, 99]. In Chapter 5, the problem of nucleation and growth of islands is discussed in detail and studied with a kinetic Monte Carlo model.

Chatterjee and Vlachos [90] presented five main challenges during the implementation of the kinetic Monte Carlo method. The first is related with building the catalog of all possible processes since, typically, such list is created in advance. The second is the search and update in the data structure, specifically, when algorithms, like the one proposed by Bortz and co-workers, are applied, hash-table-type data structure is the proper way of dealing with the categorization of processes. As much as possible, update shall be local and not global. The third is the separation of length scales, as explained previously, in

the context of the Ballistic Deposition model, considering periodic boundary conditions is not enough to avoid finite-size effects. Considered system sizes shall be larger than the length scale of the relevant phenomena. Another challenge is the separation of time scales. Being able to differ the “fast” from the rare events can improve the method. Finally, the last challenge is related with the asynchronous dynamics of the method. Considering that one event occurs at a time (no two events occurs simultaneously), becomes a bottleneck to the implementation. An approximation method have been proposed by Gillespie [100], the τ -leap method, were multiple transitions occur in parallel by considering that a single transition does not change, significantly, the population of each class of processes. There are also some effort to avoid such problem through parallel versions of the kinetic Monte Carlo method [101, 102]. Forward, from these five challenges we address two: the catalog of all processes and the separation of time scales.

Building the list of possible transitions in the system, implies an *a priori* knowledge of them all. If not all transitions are known, it is important, at least, to consider the relevant ones to describe the system dynamics. As it is discussed in Chapter 5, kinetic Monte Carlo with a list of possible transitions defined in advance, has shown to be able to describe interesting phenomena. But, on the other hand, recent works (like, e.g., [103, 104]) state that, for certain systems, concerted moves, involving more than one particle, play an important role in the system dynamics. Therefore, considering a static list of processes can become a pitfall, when kinetic Monte Carlo is used. To avoid such difficulty, new methods have been developed to build such list on-the-fly [75]. Henkelman and Jónsson [104], proposed the use of dimer method [92] to search saddle points in the neighborhood of a given state. Transition rates can then be estimated with harmonic Transition State Theory and time evolution simulated according to kinetic Monte Carlo method. Trushin et al. [105] presented a self-learning kinetic Monte Carlo method where, every time a new configuration is found, all the possible transitions are listed, through saddle-point search procedures, and included to a database of possible configurations and transitions. This way, such database is no longer static and defined *a priori*, but built during the simulation

run. Other techniques have been also developed based on Molecular Dynamics method, but are beyond the scope of this thesis [75, 103, 106, 107, 108, 109, 110, 111, 112, 113, 114].

The other challenge that we want to address is related with the existence of different time scales of processes occurring on the substrate. When the difference between the lowest and the highest energy barrier is significant, the system perform a significant number of “fast” processes (the one with low energy barrier) before a rare event occur (highest barrier). Typically, the interesting phenomena are due to these rare events, meaning that methodologies to by-pass “fast” transitions, without any bias, are required. The proposed methods to overtake this obstacle are more problem oriented. According to the specificity of the problem in hand, some techniques can be applied, e.g., Opplestrup et al. [115] presented a kinetic Monte Carlo algorithm for diffusion simulations where space is divided in “protective domains”, each one with one particle, and through first-passage arguments, particles are allowed to diffuse to the boundaries of such domains in a single iteration. Other methods have been also proposed by Novotny, see ref. [116].

As discussed through the present chapter, many computational techniques have been developed. Each one has its own strong and weak arguments. There is no universal method able to solve all possible problems. More important than just start writing codes and implement models, is important to stop, think, and analyze the level of detail, the relevant time and length scales, and then choose the proper method or set of methods.

Part II

Micro- to Nano-Scale

Chapter 3

Competitive adsorption on a line

“Entities should not be multiplied unnecessarily.”

Occam’s razor from William of Occam, in
Merriam-Webster’s Online Dictionary

From the first papers by Flory [117], on the adsorption of dimers on a lattice, and by Rényi [118, 119, 120] on the adsorption of segments on a line, the Random Sequential Adsorption (RSA) model has become a paradigm for the study of phenomena from physical chemistry, biology, ecology, and sociology [121, 122, 123, 124, 125, 126, 127, 128]. This part of the thesis is devoted to the use of the RSA model to study the adsorption of a binary mixture of segments on a line (present chapter) and the effect of a patterned substrate on the adsorption of particles on a surface (next chapter).

The RSA model was also known as car parking problem, since it has been discussed, many times, in the context of parking lots efficiency. However, recent results report that the distribution of distances between particles, obtained with the model, differs, qualitatively, from the typical distribution between parked cars [129]. In the present thesis we discuss the model in the context of adsorption, usually related with proteins and submicron colloidal particles [130]. Notwithstanding, the results can be extended, more or less straightforwardly, to different systems, where the model has been able to

grab interesting phenomena.

In the context of adsorption, different versions of the model have been considered like, e.g., the cooperative sequential adsorption, with adsorption rates dependent on the local environment [121], inclusion of relaxation mechanisms such as detachment [131, 132] and diffusion [133, 134], and multi-layer deposition [135, 136]. More recently, extended versions were considered where particles, after being adsorbed, can shrink or expand [137]. In the present chapter we address the adsorption of particles with different sizes. In fact, in the last 15 years, interest has shifted towards such problem. Research efforts have focused on the study of binary mixtures (two different sizes) of particles undergoing either *competitive* adsorption or *preadsorption*. Regarding the latter case, particles adsorb during two subsequent stages with a single particle species attempting adsorption at a time [138, 139, 140, 141]. For *competitive* adsorption both particle species attempt adsorption simultaneously [142, 143, 144, 145, 146, 147].

Our attention was drawn by some controversial results in the literature about *competitive* adsorption. Bonnier [143], in 2001, for adsorption on a line, reported a lower coverage efficiency for competitive adsorption than for adsorption of segments with single size. On the other hand, in 2002, Hassan and co-workers [145], reported that coverage is larger for binary mixture than for single size adsorption. In the present work we not only address the question above as, we also characterize the jammed-state structure of the obtained film for different values of size ratio.

Despite its illusory simplicity, the one-dimensional version of the RSA model is a source of interesting results [127]. In truth, some properties are independent of spatial dimensionality like, e.g., the existence of a jamming limit, as well as the asymptotic approach to it, and the short-range correlations between adsorbed particles. Besides, the 1D RSA is also amenable for exact treatment [117, 118, 119, 120, 142, 143, 145, 148, 149] since, due to the excluded volume interaction between particles, an empty interval smaller than the minimum particle size, separates the substrate into two disconnected regions where the kinetics of adsorption can be decoupled (shielding effect) [121].

In this chapter we study the competitive adsorption of a binary mixture of segments on a line. Specifically, through extensive Monte Carlo simulations, we analyze the influence of the aspect ratio between the two types of segments in the jammed-state structure. We compute the gap-size distribution function to characterize the interparticle distance and we study the dependence on the size ratio of the first four cumulants of the distance. Since the third and fourth cumulants are straightforwardly related to the skewness and kurtosis, we actually use the latter quantities. Despite our model being one dimensional, our analysis can serve as a guide to interpret and/or compare with similar results at higher dimensions. We also propose a truncated exponential function for the gap-size distribution at the jammed state and compute its parameters from the first moment of the distance. Afterwards, we compute the first four cumulants and, consequently, the skewness and the kurtosis. We report a good qualitative agreement with the Monte Carlo simulational results.

We start with a brief introduction of the model followed by some relevant definitions and relations. In Sec. 3.3 the Monte Carlo simulations are presented with a brief explanation of the implemented algorithm. Then, the gap-size distribution function is discussed in the context of the obtained results, with both computer simulations and with the proposed function.

3.1 Model

The competitive adsorption, on a line, of a binary mixture of segments is considered. A binary mixture is made up of segments with two different sizes: segments A with the smallest size and segments B with the largest one. The only kind of interaction between particles attempting adsorption is the excluded volume interaction: an adsorbing particle cannot overlap an adsorbed one. Such interaction mimics a short-range interaction, where the potential is infinite when an overlap occurs and zero otherwise.

Segments attempt adsorption uniformly all over the line. Once adsorbed, they stick

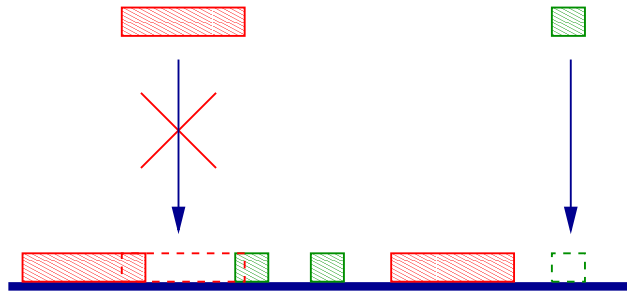


Figure 3.1: Rules of the *Random Sequential Adsorption* model.

irreversibly to the substrate, i.e., no detach or diffusion occurs in the considered time scale. When an adsorption attempt fails, due to the overlap with previously adsorbed segments, the particle is removed from the system. In fact, since the mass transport of matter to the substrate occurs through diffusion in the solution, it would be more realistic to assume that, after failing, particles should attempt adsorption in a nearby position. However, Senger et al. [150, 151] computed the coverage as well as the pair-correlation function for such more realistic process and report that the obtained jammed-state structure is indistinguishable from the RSA one.

Adsorbing particle can only stick to the substrate and not on top of other particles. On that ground, the obtained film is characterized by a single layer adsorbate. The conjugation of the excluded volume interaction and of the irreversible character of adsorption leads to an asymptotic limit, named jammed state, where no more particles can be adsorbed [125]. In Fig. 3.1 is a cartoon of the adsorption rules.

Before going on with the results, in the next section, we make some definitions and discuss some relations.

3.2 Definitions and relations

At this point it is important to clarify some definitions like, e.g., size ratio, deposition flux, coverage, and probability distribution. The first four moments and cumulants are also defined as well as the skewness and the kurtosis.

The present study is focused on the competitive adsorption of a binary mixture of segments on a line. By binary mixture we mean that segments can have two different sizes. It is possible to rescale the length scale of the system so that the smaller segments (A) are of unit length, while the larger segments (B) have size R . Therefore, R can then be defined as the size ratio of the deposited segments, i.e.,

$$R = \frac{\text{Length of a B segment}}{\text{Length of an A segment}} . \quad (3.1)$$

Segments attempt adsorption on a line. One important parameter to characterize the system is the relative population of A and B segments, performing such attempts. The deposition flux is defined as the number of incoming segments per unit length per unit time. We denote by Φ_A the corresponding deposition flux of A segments and by Φ_B the deposition flux of B segments. Therefore, the total incoming flux of segments, Φ , is

$$\Phi = \Phi_A + \Phi_B . \quad (3.2)$$

For each attempt, the probability, q_A , of having an A segment attempting deposition on the line during an interval of time dt is,

$$q_A = \frac{\Phi_A}{\Phi_A + \Phi_B} , \quad (3.3)$$

while the probability, q_B , of having a B segment is,

$$q_B = \frac{\Phi_B}{\Phi_A + \Phi_B} , \quad (3.4)$$

so $q_B = 1 - q_A$, as expected.

To make possible the comparison with experimental results, the time should be measured in terms of the number of layers of segments that attempted deposition, even when the deposition fails. As soon as the total size of the segments, which attempt adsorption on the line, equals the size of the system, we increase the time by one unit, regardless

of the fact that the segments actually adsorb, or not. Specifically, for each adsorption attempt, time is incremented by a factor Δt , such that

$$\Delta t = \frac{\text{Length of the segment}}{\text{Length of the line}} . \quad (3.5)$$

In the remaining of this section, we introduce some parameters to characterize the obtained film. For sake of simplicity, such definitions are made for the jammed state. However, extension to intermediate states at specific times can be, straightforwardly, obtained through the explicit time dependence taken into account and, also, by set the upper limit of integration to infinity to consider gap sizes of all lengths.

The most common parameter to characterize the obtained adsorbate is the coverage (θ), defined as the fraction of the line occupied by the adsorbed segments. The coverage is a function of time. Since a jammed state exists as an asymptotic limit of the adsorption process, a jamming coverage (θ_J) is given by,

$$\theta_J = \lim_{t \rightarrow \infty} \theta(t) . \quad (3.6)$$

More insight of the morphology is obtained through the analysis of the empty space between adsorbed segments. Since adsorption occurs on a line (continuum), due to the stochastic nature of the model, the coverage efficiency is lower than 100%. The jammed-state structure is made up of segments separated by a distance lower than one (length of the smaller segment attempting adsorption). To characterize the gaps we define the probability distribution of empty space as,

$$P_\emptyset(x)dx = \frac{\text{Number of empty intervals of size } x \text{ within } dx}{\text{Total number of empty intervals}} dx , \quad (3.7)$$

in the limit of dx being an infinitesimal quantity and the number of ensembles going to

infinity. Thus, $P_\emptyset(x)dx$ for the jamming state has the property

$$\int_0^1 P_\emptyset(x)dx = 1 \quad . \quad (3.8)$$

Discriminating all gaps between pairs of consecutively adsorbed segments by AA , AB , BA , and BB and defining density distribution functions $P_b(x)$, with $b \in \{AA, AB, BA, BB\}$, one obtains the relation,

$$P_\emptyset(x) = P_{AA}(x) + 2P_{AB}(x) + P_{BB}(x) \quad , \quad (3.9)$$

where we exploited the fact $P_{AB}(x) = P_{BA}(x)$ due to symmetry reasons. Note from eqs. (3.8) and (3.9) that the $P_b(x)$ are not normalized.

Higher moments of the gap-size distribution functions are defined as

$$\langle x^n \rangle_a = \frac{\int_0^1 x^n P_a(x)dx}{\int_0^1 P_a(x)dx} \quad , \quad (3.10)$$

with $a \in \{\emptyset, AA, AB, BA, BB\}$.

Using eq. (3.9) one can relate the moments of the gap distribution functions with the corresponding moment of the global distribution function given by eq. (3.10), yielding

$$\begin{aligned} \langle x^n \rangle_\emptyset &= \langle x^n \rangle_{AA} \int_0^1 P_{AA}(x)dx \\ &\quad + 2 \langle x^n \rangle_{AB} \int_0^1 P_{AB}(x)dx \\ &\quad + \langle x^n \rangle_{BB} \int_0^1 P_{BB}(x)dx \quad , \end{aligned} \quad (3.11)$$

defined for all values of $n = 0, 1, 2, \dots$

We also compute the cumulants, κ_m^a , of a distribution function defined as,

$$\ln G_a(k) = \sum_{m=1}^{\infty} \frac{(ik)^m}{m!} \kappa_m^a \quad , \quad (3.12)$$

where $G_a(k)$ is the so called characteristic function [36] defined by

$$G_a(k) = \langle e^{ikx} \rangle_a = \frac{\int_0^1 e^{ikx} P_a(x) dx}{\int_0^1 P_a(x) dx} . \quad (3.13)$$

The function above is a moment generation function, since the coefficients of its Taylor expansion contain the moments,

$$G_a(k) = \sum_{m=0}^{\infty} \frac{(ik)^m}{m!} \langle x^m \rangle_a . \quad (3.14)$$

From eqs. (3.10), (3.12), (3.13), and (3.14), one derives the first four cumulants as

$$\kappa_1^a = \langle x \rangle_a , \quad (3.15)$$

$$\kappa_2^a = \langle x^2 \rangle_a - \langle x \rangle_a^2 , \quad (3.16)$$

$$\begin{aligned} \kappa_3^a = \langle x^3 \rangle_a - 3 \langle x^2 \rangle_a \langle x \rangle_a \\ + 2 \langle x \rangle_a^3 , \end{aligned} \quad (3.17)$$

$$\begin{aligned} \kappa_4^a = \langle x^4 \rangle_a - 4 \langle x^3 \rangle_a \langle x \rangle_a \\ - 3 \langle x^2 \rangle_a^2 + 12 \langle x^2 \rangle_a \langle x \rangle_a^2 \\ - 6 \langle x \rangle_a^4 , \end{aligned} \quad (3.18)$$

where κ_1^a is just the mean value and κ_2^a the variance. The third and fourth cumulants are used in the definition of the skewness,

$$S_a = \frac{\kappa_3^a}{(\kappa_2^a)^{3/2}} , \quad (3.19)$$

and kurtosis,

$$K_a = \frac{\kappa_4^a}{(\kappa_2^a)^2} , \quad (3.20)$$

respectively [36].

3.3 Monte Carlo simulations

In this section we present the results obtained through extensive Monte Carlo simulations. The algorithm and simulations are introduced in Secs. 3.3.1 and 3.3.2, respectively. In Sec. 3.3.3 results are presented and discussed.

3.3.1 Algorithm

In Chapter 2 we stress that an efficient algorithm shall minimize, as much as possible, the number of irrelevant instructions in the code. A naive trial and error algorithm, where for each iteration an adsorption attempt occur blindly all over the substrate, is an inefficient one to simulate the adsorption of segments on a line. Therefore, to fully attain the jammed state and be able to perform enough samples it is mandatory to develop a more tailored algorithm.

For the present study, only the jammed-state structure is important so, the description of the kinetics toward the jammed state is not relevant. On that ground, the algorithm presented here is not capable of describing the evolution toward the jammed state, it only deals with the jammed state itself. We leave the discussion about an algorithm to study the kinetic behavior to the next chapter.

When a segment is adsorbed, on a given gap, the substrate is divided into two smaller gaps. Due to the shielding property, the adsorption on each gap is independent, meaning that the kinetic of adsorption can be decoupled. The jammed-state structure can be generated for each gap independently. We use such concept to develop the algorithm.

To start, a segment type is randomly selected, according to the probabilities q_A and q_B , and adsorbed on the center of the substrate. Then, for each iteration, for all gaps larger than unitary size, a particle size is generated. If the size of the gap is smaller than the larger particle size, the size is trivially one, otherwise, the segment size is selected according to the fluxes. A position for adsorption inside the gap is randomly chosen. If adsorption do not leads to overlap with previously adsorbed segments, the adsorption is

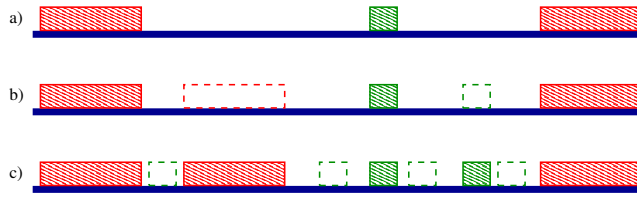


Figure 3.2: Algorithm cartoon for three consecutive steps (a), (b), and (c). The dashed particles represent segments adsorbed during the elapsing step.

successful and two new gaps are obtained. The process is repeated till no gap larger than one is found. In Fig. 3.2 is a cartoon of such algorithm for three consecutive iterations.

With the scheme described above, the jammed-state structure of the film is obtained. It is important to stress, once again, that this algorithm is tailored to generate asymptotic configurations. No information can be obtained about the kinetics toward the limiting state.

3.3.2 Simulations

To characterize the dependence of the jamming coverage and jammed-state structure on the size ratio, we performed a series of Monte Carlo simulations. For simplicity, we consider the case of equal fluxes of incoming segments, i.e., $q_A = q_B$.

To obtain the results, discussed below, we implemented the algorithm presented previously, except to study the time dependence, where a different algorithm was considered. The latter requires more computational time than the former and it is discussed in the next chapter.

We simulated a system size of 10^7 units and generated 10^2 samples to characterize the jammed state. For the study of time dependence, since the algorithm is computationally more demanding, we simulated a smaller system size, 10^6 , and obtained 10^2 samples.

In a recent paper, Hassan et al. [145], consider that particle, attempting adsorption, has the smaller size with probability q and the larger size with probability $1 - q$. In the present case, we consider equal fluxes for both segment sizes, meaning that our study

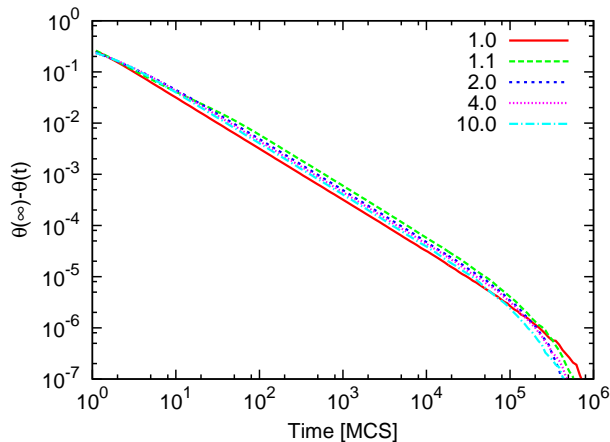


Figure 3.3: Coverage dependence on the size ratio for equal depositing fluxes of each segment size, for various values of the size ratio, namely, 1, 1.1, 2, 4, and 10. Results obtained for a system size of 10^6 and averaged over 10^2 samples.

represents the particular case of $q = 1/2$. However, results of this reference are only valid for values of R below two. We, not only, consider a wider range of size ratios as, our study, also includes quantities, such as dispersion and fraction of empty space, which are not possible to compute by their method.

We perform a wide range of values of size ratio, namely for values of 1, 1.05, 1.1, 1.2, 1.25, 1.3, 1.4, 1.5, 1.6, 1.75, 2, 2.1, 2.25, 2.5, 2.75, 3, 3.25, 3.5, 3.75, 4, 4.5, 5, 5.5, 6, 7, 8, 10, 12, 14, 16, 18, and 20.

3.3.3 Results

We presently discuss the results obtained with the Monte Carlo simulations. We split the discussion in two different parts. A first one where the jammed state is discussed based on the coverage, the fraction of empty space, and the population of each gap type, and a second one where the cumulants up to the fourth order are reported and analyzed. We leave for the next section the study of the gap-size distribution function.

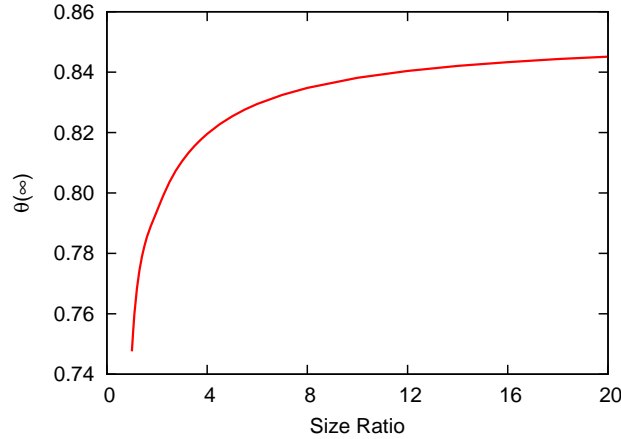


Figure 3.4: Coverage dependence on the size ratio for equal depositing fluxes of each segment size. Plot showing the jamming coverage dependence on the size ratio.

Jammed state structure

To analyze the jammed state we start with the analysis of the coverage. In Fig. 3.3 we plot the time dependence of the coverage, $\theta(t)$, for some values of size ratio, namely, 1.0, 1.1, 2.0, 4.0, and 10.0. We observe that, the approach to the jamming limit scales according to a power-law, with exponent 1, independent of the size ratio.

Since the first works of Rényi, for deposition of segments with unit size on a line, the value of the coverage has been discussed in the literature. Our model boils down to such limit when the size ratio is equal to one. We obtain the value of $74.75958\% \pm 0.0067\%$ which is quite close to 74.75979202% , first obtained by Rényi and subsequently calculated with larger precision by Blaisdell and Solomon [118, 143, 145].

As referred previously, regarding the effect of a binary mixture on the coverage efficiency, two contradictory analytical results, were reported in the literature. According to Bonnier [143], the coverage efficiency decreases with the size ratio and, the case of unit segment size, is a higher bond of coverage efficiency. On the other hand, Hassan and co-workers [145] reported the adsorption with size ratio equal to one as a lower bond and an increase of the coverage efficiency with the size ratio. In Fig. 3.4 we plot the jamming coverage as a function of the size ratio. A monotonically increase of the efficiency is ob-

Table 3.1: The table presents the coverage, θ_J , as a function of the size ratio, R , while σ represents the associated error. These results are for a system size of 10^7 and for 10^2 samples.

R	θ_J	σ
1.00	0.7475958	0.000067
1.05	0.7544753	0.000062
1.10	0.7599829	0.000063
1.20	0.7683652	0.000058
1.25	0.7716358	0.000063
1.30	0.7744377	0.000054
1.40	0.7789946	0.000063
1.50	0.7825520	0.000064
1.60	0.7854349	0.000053
1.75	0.7890016	0.000066
2.00	0.7941038	0.000058
2.10	0.7961414	0.000053
2.25	0.7991661	0.000058
2.50	0.8036444	0.000060
2.75	0.8073996	0.000065
3.00	0.8105172	0.000066
3.25	0.8131850	0.000060
3.50	0.8155590	0.000065
3.75	0.8176675	0.000073
4.00	0.8195500	0.000070
4.50	0.8227540	0.000063
5.00	0.8253667	0.000067
5.50	0.8275848	0.000074
6.00	0.8294481	0.000076
7.00	0.8324537	0.000076
8.00	0.8347729	0.000094
10.00	0.8381112	0.000097
12.00	0.8403695	0.00010
14.00	0.8420603	0.00011
16.00	0.8433187	0.00013
18.00	0.8443186	0.00012
20.00	0.8451377	0.00012

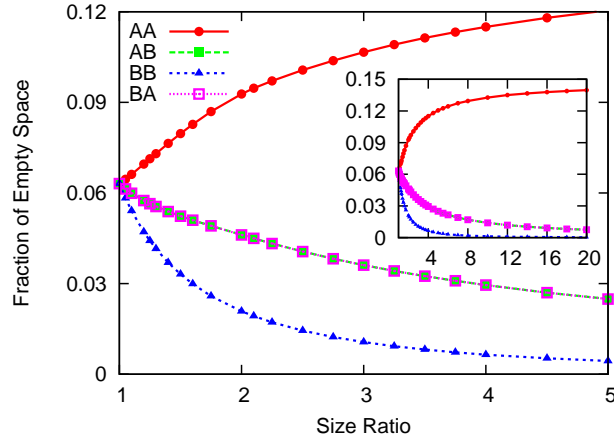


Figure 3.5: Fraction of available empty space, at the jamming state. In the insets the size ratio varies between 1 and 20. One has the AA -, AB -, and BB -gap types represented by circles, squares, and triangles, respectively. Due to symmetry reasons, the BA case (non filled squares) is equal to the AB one.

served (see Table 3.1). Therefore, our results support the ones from Hassan et al. [145], which it is not entirely surprising, since for equal relative fluxes of incoming segments and large asymptotic values of the size ratio, a stretch of the line is either fully covered by a large segment or paved by the small, unit size, segments with an upper limit of the coverage given by the Rényi value. As both segment sizes can attempt deposition with equal probability, we get $1/2(1 + 0.7476) = 87.38\%$. However, this upper limit is not attained as one increases the values of the size ratio, the limiting value of the coverage around 84.5%, obtained for a size ratio of 20, remains lower as one can observe in Fig. 3.4.

In the Fig. 3.5 is the fraction of empty substrate, at the jamming state, as a function of the size ratio. We differentiate each pair of consecutive segments, namely of type AA , AB , BA , and BB . As explained before, the case of BA overlaps the AB case due to the model symmetry. At the jammed state, a monotonic increase of the fraction of empty space with the size ratio, for AA -gap type, is observed as well as a decrease of the remaining gap types. To understand such behavior we plot, in Fig. 3.6, the normalized population of the gap types. The sum of the contributions of the four gap types adds up to the unit for every values of the size ratio. The fraction of empty space due to the AA

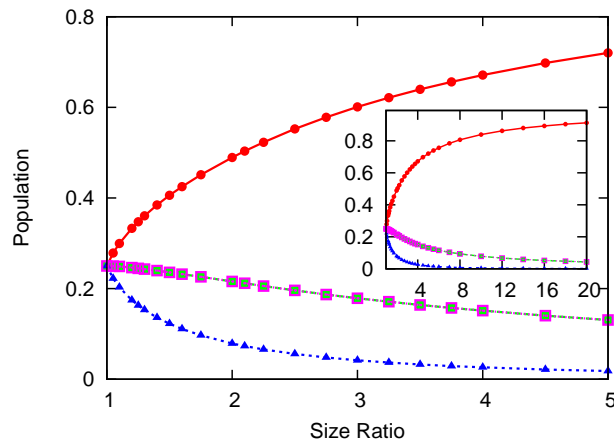


Figure 3.6: Normalized population of gaps at the jamming state. In the insets the size ratio varies between 1 and 20. We use the same legend as in Fig. 3.5.

gaps increases monotonically with the size ratio. This can be understood by considering the significant drop in the population of BB gaps at the jammed state as the size ratio increases, since these gaps must be smaller than unit. The probability of having two consecutive B segments adsorbed on the line decreases with size ratio since adsorption of two, neighboring, large segments imply a gap larger than their size and both being adsorbed at a distance smaller than unit to prevent an A segment to fit in between. Such probability decreases with size ratio. Increasing the size ratio, rise the number of small segments (A) that can adsorb between two B segments, which implies an increase of AA population. The diminishment of AB population and of the fraction of corresponding empty space, indicates, for large size ratios, a jammed state constituted by alternating streaks of A segments by a single B segment. This argument is consonant with the drop of BB population. With the increase of size ratio, the relative population of AB and BB gap types, as compared to the corresponding population of the AA gaps becomes less and less relevant, therefore leaving, in this limit, long streaks of A segments.

Table 3.2: The table summarizes the estimated values of R , where the first four cumulants take maximum and minimum values, all measured with an error of ± 0.005 . The corresponding values of the cumulants are also included. Cells marked with $(*)$ means that the BB -gap is strictly monotonic.

gap types		minimum		maximum	
		R	Value	R	Value
Distance					
	AA	1.31	0.2924895		
	AB	1.22	0.3291302		
	BB		(*)		(*)
Dispersion					
	AA	1.55	0.2681662	1.02	0.2825507
	AB	1.55	0.2788692	1.05	0.2825593
	BB	1.01	0.2815730	-	-
Skewness					
	AA	-	-	1.34	0.9227950
	AB	-	-	1.29	0.7253401
	BB		(*)		(*)
Kurtosis					
	AA	-	-	1.40	-0.2290402
	AB	-	-	1.36	-0.6281340
	BB		(*)		(*)

Cumulants up to the fourth order

Above, the jammed state was characterized by its coverage, population of gaps, and fraction of empty space. To analyze further, it is important to obtain more information about the distribution of gaps. We compute quantities involving cumulants up to the fourth order and propose the use of them to describe the film structure.

In Fig. 3.7(a-d) are the mean distance (Fig. 3.7(a)), dispersion (Fig. 3.7(b)), skewness (Fig. 3.7(c)), and kurtosis (Fig. 3.7(d)), as defined in eqs. (3.15)-(3.20). We study, at the jammed state, the dependence of these quantities on the size ratio. We observe that, both the AA and AB gap types have rich nonmonotonic behavior, for the mean gap size, dispersion, skewness, and kurtosis. Despite such nonmonotonic behavior, the critical

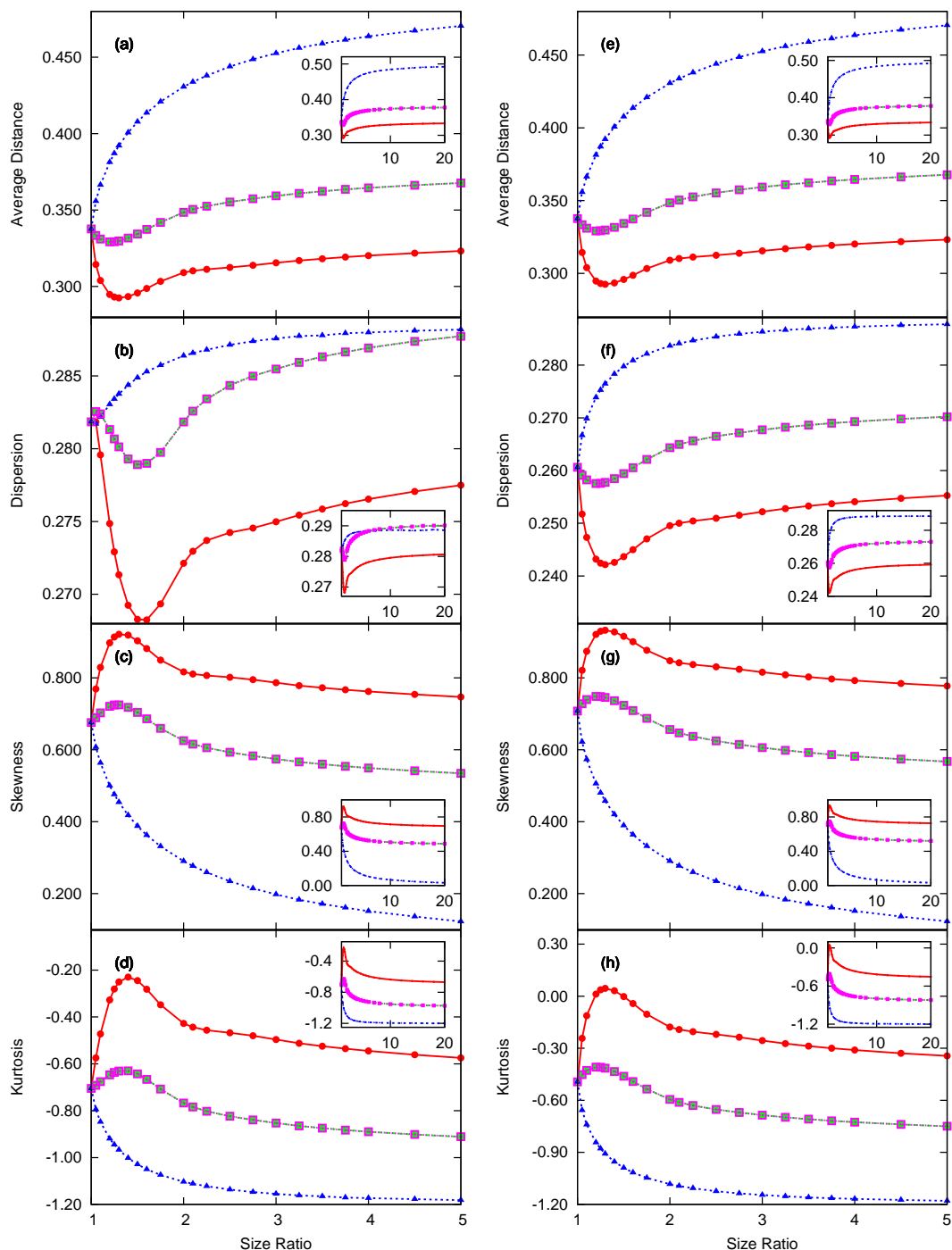


Figure 3.7: Plots involving cumulants up to the fourth order of the gap-size distribution functions for each gap type as a function of the size ratio. Results obtained through Monte Carlo simulations (a, b, c, and d) and from proposed function to the gap-size distribution (e, f, g, and h). We use the same legend as in Fig. 3.5. (a) and (e) Average distance between pairs of segments. (b) and (f) Dispersion of the distance between pairs of segments. (c) and (g) Skewness. (d) and (h) Kurtosis.

values for AA and AB gaps are not coincidental. As summarized in Table 3.2, for most cases, the critical values for AA gaps occur at a slightly higher value of the size ratio. The behavior of the dispersion shows the presence of both a minimum and a maximum values. It is only for the maximum value of the dispersion that the opposite happens. The value of the size ratio at which it occurs is slightly lower for the AA gap type than for AB one. In fact, the minimum values occur, within the error bounds, at the same values of R . The skewness shows a maximum occurring at different R values, namely, 1.34 and 1.29 for the AA and AB gap types, respectively. The kurtosis reveals a single maximum for these two gap types, once again noncoincidental in their size ratio value, with the maximum for the AA gaps, once again, slightly above, the corresponding one for the AB gaps.

Regarding the BB type, we observe a less rich behavior. The mean gap size strictly increases, monotonically, with R , and the skewness and the kurtosis decreases. The exception regards the dispersion. For the dispersion, a minimum occurs for $R = 1.01$ as evident in Fig. 3.7(b) and stated in Table 3.2. Note also, from the inset of the same figure, that the dispersion of BB and AB intersect at $R = 6$.

If only large segments were deposited, then all gap sizes up to R would be present. Since we are depositing a binary mixture with unit segments, all gap sizes larger than unit must disappear at the jamming limit due to the adsorption of unitary segments. As soon as the typical sizes of gaps drops below R , the large segments stop adsorbing on the line. The smaller, unit segments (A), contrary to larger segments (B), have to fit into all available spaces (gaps larger than unit). For size ratios $R < 1.55$ the population of BB gaps remains significant, as compared to the AA gap one, with the consequent formation of BB gaps close to unit. Some of this gaps, are strictly larger than unit, in size, and we call this events of *snug fits*, regarding the adsorption of a smaller segment on such space. As R increases the number of BB gaps decreases, to form AA and AB gaps, therefore, increasing the probability of *snug fit* events. With larger R the probability of a BB *snug fit* decreases and, therefore, a monotonic behavior of the various cumulants for this regime is observed. On the other hand, the larger number of these events for values of $R \lesssim 1.55$

accounts for such rich behavior of the cumulants up to the fourth order. On that ground, the minimum values of the AA and AB gap sizes can now be understood as events from the late stage kinetics close to the jamming state and the same for the minimum values of the dispersion, since such events tend to lower the uncertainties of adsorbed segments.

For values of $R < 1.05$ there is a maximum value for both AA and AB gaps and a minimum of the BB gaps. Since the size difference of both segments is small, they compete until coverage values become close to the jammed state, which leads to *snug fit* events of the BB gap. Consequently, the uncertainty for the BB gaps diminish and for the AA and AB gaps intensify.

For values of $R \geq 1.55$, the significant drop in the population of BB gaps can be understood of the early onset of a mean gap size smaller than R at low coverage values, which effectively blocks the adsorption of large segments. We obtain a flatter distribution function of the BB gap type with increasing values of the size ratio, since the net effect of increasing the size ratio is to diminish the asymmetry of the BB gap distribution. The monotonic behavior for $R > 1.55$ stems from the absence of a competing mechanism.

For large size ratios, the jamming state follows, therefore, the picture of alternating streaks of A segments, interfaced with a single B segment referred above. The presence of such streaks prevents the AB gap population to decrease slower than that of the BB gap one. The *snug fits* also favor small gap sizes, and this effect makes the distribution function less *flat* and more skewed, thus increasing the value of the kurtosis and skewness of both AA and AB gaps in the region where the effect is manifest, specifically, for $R < 1.5$.

3.4 The gap-size distribution

So far we considered the first four cumulants to characterize the distribution of empty size on the line. Another way is to analyze the distribution itself. In the present section we start with a description of the gap-size distribution, defined in eq. (3.7), obtained through computer simulations. Then, based on heuristic arguments, a function is proposed

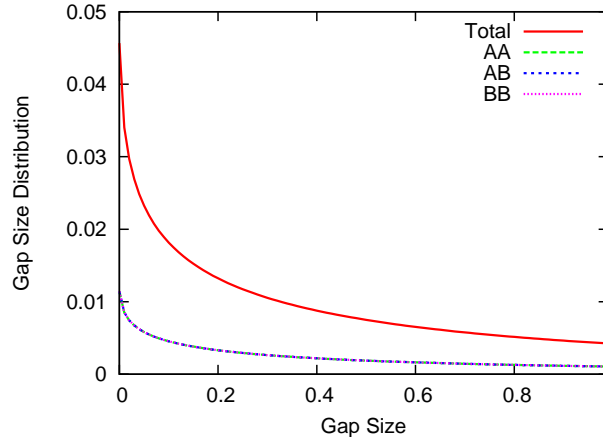


Figure 3.8: Gap-size distribution functions at the jamming state: For a size ratio of one, the solid curve represents $P_\emptyset(x)$, while the remaining AA -, AB -, and BB -gap types are identical, and therefore fall onto a single curve.

and cumulants are computed with it. We report results obtained with such function in agreement with the computational results.

3.4.1 Computational results

In Figs. 3.8 and 3.9, we plot the gap-size distribution for size ratio of one and two, respectively. For each case we differ the contribution of each gap type. Results were obtained with Monte Carlo simulations in the conditions described above.

The distribution functions, $P_\emptyset(x)$, $P_{AA}(x)$, $P_{AB}(x)$, and $P_{BB}(x)$, at the jammed state, for a size ratio of one, are in Fig. 3.8. As expected, for this size ratio, all gap types are equal since there is a single segment size. Therefore, a collapse of the $P_{AA}(x)$, $P_{AB}(x)$, and $P_{BB}(x)$, onto a single curve, is observed. The distributions satisfies the relation $P_\emptyset(x)/4 = P_{AA}(x) = P_{BB}(x) = P_{AB}(x)$ in agreement with eq. (3.9) for a size ratio of one.

In Fig. 3.9, we merely change the value of size ratio to 2.0. Due to the difference in size between the two types of segments, A and B, the symmetry between the various gap types is broken. The only symmetry that remains is the one between AB and BA gap types. Adding the various gap distributions, for every value of gap size, according to

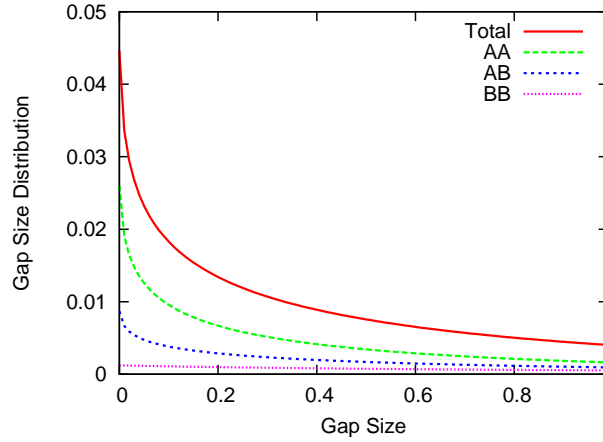


Figure 3.9: Gap-size distribution functions at the jamming state: For a size ratio of 2.0, one observes the splitting of the various gap types. Please, refer to the text for further details.

eq. (3.9), actually reproduces $P_\emptyset(x)$. As compared with size ratio of one, the AA gap type increases its dominance and, consequently, the AB gap slightly lowers its contribution and the BB gap significantly drops its influence. As stated before, with size ratio, becomes less probable to have consecutive deposition of B segments with gap lengths smaller than unit.

3.4.2 Proposed function

The probability that a segment is deposited in a given gap is proportional to the size of the gap, therefore, the probability distribution shall be an exponential distribution. Besides, at the jammed state, the probability of having a gap with size larger than one is zero. Consequently, we propose, for the gap-size distribution, at the jammed state, an exponential function truncated between zero and one, i.e.,

$$P_a(x) = \begin{cases} A_a(\alpha_a)e^{-\alpha_a x}, & 0 < x < 1 \\ 0, & x > 1 \end{cases}, \quad (3.21)$$

where α_a is the single parameter used to characterize the distribution function. As defined, only $P_\emptyset(x)$ must be normalized so,

$$A_\emptyset^{-1}(\alpha_\emptyset) = \int_0^1 e^{-\alpha_\emptyset x} dx = \frac{1 - e^{-\alpha_\emptyset}}{\alpha_\emptyset} . \quad (3.22)$$

With eq. (3.10) it is possible to obtain the first two moments of the distribution as a function of α_a ,

$$\langle x \rangle_a = \frac{1}{1 - e^{\alpha_a}} + \frac{1}{\alpha_a} \quad (3.23)$$

and

$$\langle x^2 \rangle_a = \frac{2 + \frac{\alpha_a(2+\alpha_a)}{1-e^{\alpha_a}}}{\alpha_a^2} . \quad (3.24)$$

The first and the second cumulants are obtained with eqs. (3.15) and (3.16), so

$$\kappa_1^a = \frac{1}{1 - e^{\alpha_a}} + \frac{1}{\alpha_a} \quad (3.25)$$

and

$$\kappa_2^a = \frac{1}{\alpha_a^2} + \frac{1}{2 - 2\cosh(\alpha_a)} . \quad (3.26)$$

Skewness and kurtosis

To better characterize the distribution function it is important to compute the higher-order moments and cumulants. With them it is possible to compute the skewness and the kurtosis. The former is related with the asymmetry of the distribution. The kurtosis, since we assume that we compare the kurtosis of functions of the same type, can be used to relate the peakness or flatness of each one.

To compute these two parameters, it is necessary the third and fourth moments. Following, once again, the definition given by eq. (3.10), for the proposed function (3.21), we obtain,

$$\langle x^3 \rangle_a = \frac{6 - 6e^{\alpha_a} + \alpha_a(6 + \alpha_a(3 + \alpha_a))}{(1 - e^{\alpha_a})\alpha_a^3} \quad (3.27)$$

and

$$\langle x^4 \rangle_a = \frac{24 - 24e^{\alpha_a} + \alpha_a(24 + \alpha_a(12 + \alpha_a(4 + \alpha_a)))}{(1 - e^{\alpha_a})\alpha_a^4} . \quad (3.28)$$

From eqs. (3.27) and (3.28), through the definitions (3.17) and (3.18), we obtain,

$$\kappa_3^a = \frac{2}{\alpha_a^3} - \frac{1}{4} \coth\left(\frac{\alpha_a}{2}\right) \operatorname{csch}^2\left(\frac{\alpha_a}{2}\right) \quad (3.29)$$

and

$$\kappa_4^a = \frac{6}{\alpha_a^4} - \frac{1}{8} (2 + \cosh(\alpha_a)) \operatorname{csch}^4\left(\frac{\alpha_a}{2}\right) . \quad (3.30)$$

The skewness and the kurtosis can then be obtained, according to eqs. (3.19) and (3.20), so

$$S_a = \frac{4 - 4\cosh(\alpha_a) + \alpha_a^3 \coth\left(\frac{\alpha_a}{2}\right)}{\alpha_a \sqrt{\frac{1}{\alpha_a^2} + \frac{1}{2 - 2\cosh(\alpha_a)}} (2 + \alpha_a^2 - 2\cosh(\alpha_a))} \quad (3.31)$$

and

$$K_a = -\frac{2((24 + \alpha_a^4)\cosh(\alpha_a) + 2(-9 + \alpha_a^4 - 3\cosh(2\alpha_a)))}{(2 + \alpha_a^2 - 2\cosh(\alpha_a))^2} , \quad (3.32)$$

for the distribution function previously defined by eq. (3.21).

Results with proposed distribution function

With the Monte Carlo results and the first moment defined by eq. (3.23) we determine the values of the parameter α_a for all type of gaps and for values of size ratio ranging from 1.0 to 20.0. In Fig. 3.10 are the values of α_a as a function of the size ratio. For *BB* gap type a monotonic decrease is observed. For *AA* and *AB* gap types a nonmonotonic behavior is reported, with a maximum at 1.30 ± 0.05 to the *AA* type and at 1.20 ± 0.05 to the *AB*.

Following the eqs. (3.25), (3.26), (3.31), and (3.32), and the obtained values of α_a , we compute the mean size, dispersion, skewness, and kurtosis, of the gap sizes. The results are plotted in Figs. 3.7(e-h). For *AA* and *AB* gap types, we observe a nonmonotonic behavior for all parameters. For *BB* gap type, we obtained a monotonic increase for the

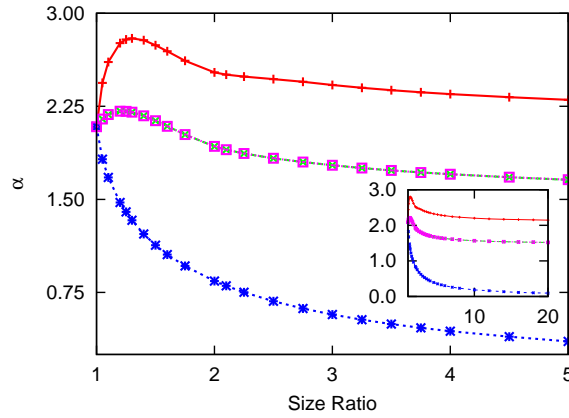


Figure 3.10: Plot of α_a as a function of size ratio obtained from the first moment of Monte Carlo simulations. We use the same legend as in Fig. 3.5

mean size and dispersion, and a monotonic decrease for the skewness and kurtosis. For the mean size and dispersion, the minimum for the *AA* gap type occurs at 1.30 ± 0.05 , and for the *AB* gap occurs at 1.20 ± 0.05 . For the skewness and kurtosis, there is a maximum for the *AA* type at 1.30 ± 0.05 and at 1.20 ± 0.05 for the *AB* type.

In Fig. 3.7(e-h), these results can be compared with simulational ones, in Fig. 3.7(a-d). For all parameters the same qualitative behavior is obtained. For the dispersion, the proposed probability distribution (3.21), does not reproduce simulational results, for size ratio near one. The difference can be due to the *snug fit* events explained previously. These events destroy the exponential behavior of *AB* gap type distribution functions. Recall that *snug fit* events are only relevant for values of R close to unit.

3.5 Conclusions

In this chapter we studied the competitive sequential adsorption of a binary mixture of segments on a line. The considered binary mixture is made up of segments with two possible sizes. Both segments arrive to the substrate with the same flux. Specifically, we characterized the morphology of the jammed state and its dependence on the size ratio.

Monte Carlo simulations were performed, for different values of size ratio, and the

cumulants, up to the fourth order, of the size of empty spaces, computed. We propose the use of four parameters to describe the structure of the jammed state, namely, the mean size, dispersion, skewness, and kurtosis, of the hiatus between adsorbed segments. For values of the size ratio below two, the behavior of such parameters, for the AA , and AB types are nonmonotonic due to the presence of *snug fit* events. For large values of size ratio, the jamming state is characterized by streaks of A interrupted by a single B .

We also presented a different approach with potential for a more detailed analysis. The first moment, obtained from simulation, can be used to grab information about the other three. A truncated distribution was proposed for the gap-size distribution and parametrized from the mean gap size. Then, with the obtained function, the dispersion, skewness, and kurtosis were computed. The results are in qualitative agreement with Monte Carlo simulations and the specific differences in the dispersion can be explained by *snug fit* events.

Chapter 4

How can a pattern change the irreversible adsorption?

“Order is repetition of units. Chaos is multiplicity without rhythm.”

M. C. Escher, in *Thinkexist.com*

In the previous chapter we discussed the implementation of the random sequential adsorption (RSA) model to study the adsorption of a binary mixture of segments on a line. In the present one, the same model is considered to characterize the effect of pre-treated substrates on the irreversible adsorption of colloids. By pre-treated we mean that a pattern is constructed on the surface such that adsorption can only take place inside well defined regions.

The study of monolayer and multilayer fine-particle deposits (e.g., colloids) at surfaces is of interest for a wide range of applications, including photonic crystals, quantum dots, heterogeneous catalysts, sensors, and microarrays [152, 153, 154, 155, 156, 157, 158]. The control of the film properties requires a quantification of the kinetics of synthesis, aggregation, and surface interactions of particles. Furthermore, the surfaces with which fine particles interact can now be pre-treated to control and modify the particle attachment

kinetics and the resulting deposit morphology [149, 152, 159, 156, 160, 161, 162, 163]. Specifically, it is possible to build well defined, regular, and reproducible patterns on a substrate with different shapes and distributions [160, 163, 164, 165, 166, 167, 168]. It is important to stress that, recent experiments have produced pattern with a typical size of the order of the particle size. Thus, deposition kinetics will be affected by such adsorption constrain which can improve the properties of the obtained film. From a theoretical perspective, such processes pose interesting challenges, including identification of the parameters that control the properties of the resulting structure.

We report a detailed study of the influence of a pattern consisting of cells, with square shape, in which centers of circular particles can land (e.g., projections of spherical fine particles depositing in a monolayer), distributed in a square lattice array. The adsorption process is considered to be fully irreversible and particles are considered to have fixed size and interact solely through excluded volume. Therefore, we develop an extended version of the random sequential adsorption (RSA) model for rigid disks adsorption on patterned substrates.

So, with RSA model [121, 122, 125, 142, 143, 146, 148, 169, 170, 171, 172, 173, 174] we assume that particle-particle interactions and particle-substrate interactions can be accounted for, approximately, by purely geometrical restrictions and features. Furthermore, the details of the particle transport to (and, for rejected particles, away from) the surface are lumped into the assumption of uniform flux of deposition attempts per unit surface area¹. Despite its simplicity, the RSA model provides a surprisingly rich set of limiting behaviors and morphologies [120, 121, 122, 123, 125, 126, 128, 137, 147, 149, 175, 176, 177, 178, 179, 180, 181, 182, 183].

As already discussed in the context of the previous chapter, the hard-core interaction between particles, as well as the irreversibility of the adsorption process, leads to a jammed state in the asymptotic limit, where no more particles can be adsorbed (see, e.g., [125]).

¹As already discussed in Chapter 3, a more realistic description of mass transport to the substrate shall account with particles diffusion in the solution. However, Senger et al. [150, 151], report that the obtained structure would be similar to the RSA one.

Such jammed state is made up of a single layer since particles cannot adsorb on top of other particles. In the present chapter, we characterize the influence of the pattern on the structure of the obtained single-layer deposit and in the kinetic evolution of the film during adsorption.

Computer simulations able to fully attain the jammed state are far-from trivial, due to the stochastic nature of the adsorption process in the continuum. We also present an algorithm to perform Monte Carlo simulations of such model. Due to the relevance of RSA model in different fields [128, 137, 147, 184, 185, 186, 187, 188, 189], we attempt a general discussion of such implementation for cases with and without the pattern. From now on, for sake of simplicity, the substrates without pattern are denoted as clean or regular substrates.

The chapter is organized in the following way. We start with a brief description of the model and some definitions in Sec. 4.1. A diagram of the system based on the pattern parameters is presented and its main regions are discussed in Sec. 4.2. The jammed-state structure and the adsorption kinetics are discussed in the Secs. 4.3 and 4.4, respectively. In the Sec. 4.6, we draw some conclusions.

4.1 Model and definitions

Our goal is to study irreversible adsorption of identical hard-core spherical particles on flat patterned substrates, which is equivalent to the deposition of disks with excluded volume interaction. As explained in the preceding chapter, such type of interaction means that the interacting potential is infinite when overlap occurs and zero otherwise.

To characterize the effect of a pattern in the adsorption process we consider that particles can only adsorb on well defined regions on the substrate. For simplicity, such regions are considered to have square shape. But, in fact, other shapes could also be considered, therefore, from now on, we refer to such square regions as cells, since most of the general conclusions can be straightforwardly map to different cell shapes. Cells are

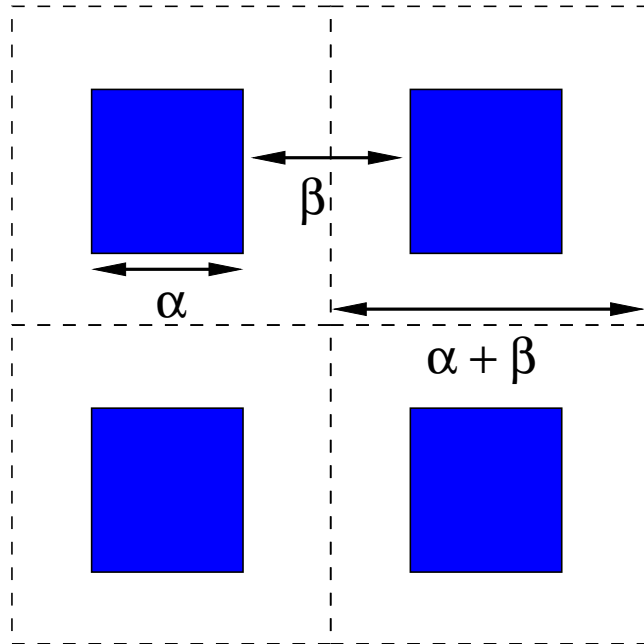


Figure 4.1: Scheme of four pattern unit cells. Dashed lines delineate the square lattice unit cells. Adsorption of disks can only take place when their geometrical center lands inside the blue regions. Two parameters characterize the pattern, the size of the cell and the cell-cell separation.

considered to be distributed in a square lattice array, i.e., one cell per vertex of a square lattice. Such configuration of cells in a lattice leads to the concept of *unit cell* which is larger than the landing cell (represented by dashed lines in Fig. 4.1).

In the present work, we consider particles of fixed radius, r_0 . Experimentally, the particles size and shape are always characterized by some dispersion. For dispersions above $\mathcal{O}(10\%)$ of the mean size, particles are considered polydispersed. Syntheses of uniform spherical colloids and polydispersity as low as 4% have been reported [190, 191, 192, 193, 194, 195, 196, 197, 198, 199, 200, 201, 202, 203, 204, 205], so that the monodisperse approximation is quite realistic for many systems of interest. Notwithstanding, studies were also performed for particles with gaussian-size distribution [188], but are beyond the scope of the present thesis.

We assume that particles arrive with flux F . Recall that flux is the rate, per unit

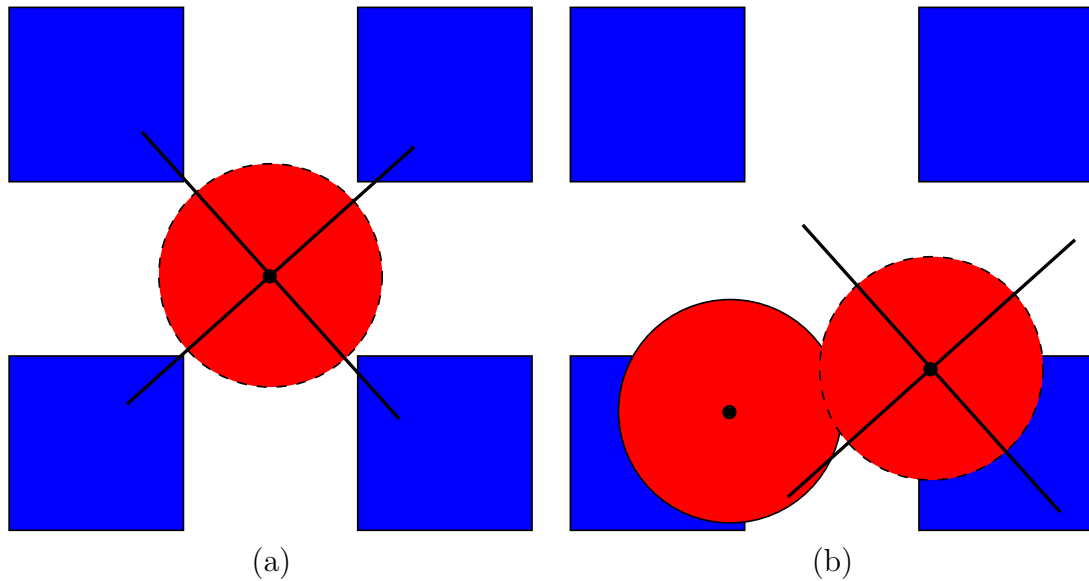


Figure 4.2: A disk fails adsorption onto the substrate because (a) its center does not fall within an allowed-landing cell, or (b) it overlaps with a previously adsorbed disk.

time, of deposition attempts of disk centers at the substrate, per unit area. Particles arrive to the surface randomly and uniformly. If the disk (geometrical) center falls outside the cell or overlap a previously adsorbed particle, adsorption fails, see Fig. 4.2. Otherwise, if adsorption is successful, particles stick, irreversibly, to the substrate. Irreversible means that, after being adsorbed, particles cannot detach or diffuse, which is a very good approximation for colloid deposition [125, 126], but can be questioned, e.g., for protein deposition: indeed, studies of RSA-type models with particle rearrangement on the surface have also been reported [206, 207, 208, 209, 210, 211, 212, 213, 214]. Particles can only bind to the substrate and not on top of other particles, leading to a single layer deposit, a jammed state is then obtained where no more particles can be adsorbed² [130, 217].

The conditions described above can be well mimicked by the RSA model. The deposition rules are then summarized in Fig. 4.2. In the irreversible RSA model, the deposit density initially grows linearly with time, t . However, as the particle density increases,

²Multilayer adsorption was studied in various experimental and theoretical contexts [135, 136, 169, 215, 216].

the hard-core exclusion leads to slowdown of the adsorption process. Ultimately, for large times the jammed state is approached, at a density lower than that of close packing and with no long-range order in the particle positioning, but no gaps left for any additional particle deposition. The density of particles can be characterized, as in the previous chapter, by the coverage, $\theta(t)$, i.e., the fraction of the total surface covered by the particles. The jammed state coverage is defined, as discussed in eq. (3.6), as

$$\theta_J = \lim_{t \rightarrow \infty} \theta(t) . \quad (4.1)$$

Time is defined in a way that, when a unit time elapses, the total area of the particles that attempt adsorption is equal to the area of the substrate (L^2). Meaning that, for adsorption of particles with radius r_0 , everytime a particle attempt adsorption time is incremented by

$$\Delta t = \frac{\pi r_0^2}{L^2} . \quad (4.2)$$

Therefore, the time is rescaled by a factor inversely proportional to the flux and particle “volume”, here $(\pi r_0^2 F)^{-1}$.

As stated previously, we consider as a pattern, equal size cells regularly distributed over the substrate, in a square lattice arrangement (see Fig. 4.1). The pattern is characterized by two different parameters: the size of the cell a and the cell-cell distance b . Meaning that, the unit cell has size $a + b$. Since all the particles, attempting adsorption, are considered to have the same size, is preferable to use adimensional parameters to characterize the pattern. Without loss of generality, we rescale the substrate lengths relative to the diameter of the disks. Specifically, we define

$$\alpha = \frac{a}{2r_0} , \quad (4.3)$$

and

$$\beta = \frac{b}{2r_0} . \quad (4.4)$$

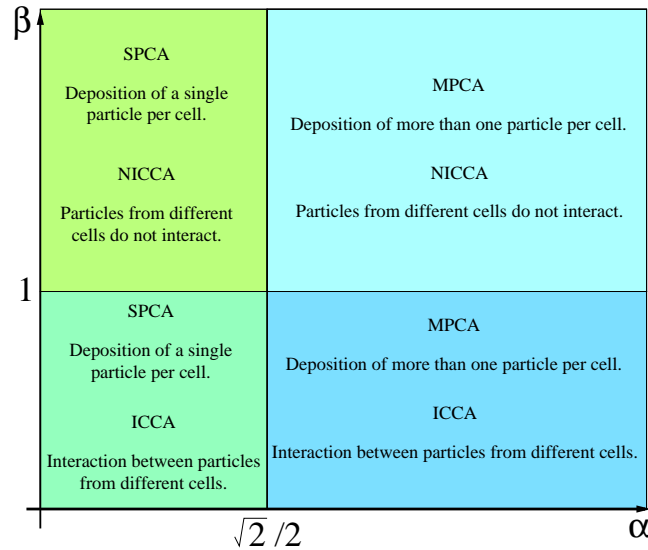


Figure 4.3: The major subdivisions in the two-parameter space. For cell-cell separation $\beta < 1$ we have the *interacting cell-cell adsorption* (ICCA), while for $\beta \geq 1$ we have the *noninteracting cell-cell adsorption* (NICCA). For cell sizes $\alpha < 1/\sqrt{2}$ we have a *single-particle-per-cell adsorption* (SPCA), while for $\alpha \geq 1/\sqrt{2}$ we have *multiparticle-per-cell adsorption* (MPCA).

The present model is a generalized version of lattice RSA [117, 118, 121, 122, 125, 126, 127, 128, 141, 169, 217], on par with such generalizations as RSA of mixture (see previous chapter) [146, 143, 144, 145, 137, 147, 148, 149, 218, 219, 220, 221] or deposition on finite-size substrates [142].

4.2 The “Phase Diagram”

Based on the cell size (α) and the cell-cell separation (β) we propose a diagram in the two-parameters space (α, β) , to categorize the typical regimes of adsorption. In the horizontal axis is the parameter α , related with the cell size and, in the vertical axis, is the parameter β , related with the cell-cell separation. The diagram is in Fig. 4.3.

For values of cell size such that only one particle can be adsorbed per cell ($\alpha < \frac{1}{\sqrt{2}}$), stands the *single-particle-per-cell adsorption* regime (SPCA). On the other hand, for $\alpha \geq \frac{1}{\sqrt{2}}$, the regime is denoted *multiparticle-per-cell adsorption* (MPCA). Regarding

the cell-cell separation, vertical axis, two different regimes can also be identified. For $\beta < 1$, particles attempting adsorption on a given cell can be constrained by particles previously adsorbed on neighboring cells. Such regime is denoted *interacting cell-cell adsorption* (ICCA). For $\beta \geq 1$, cell-cell distance is such that adsorption on each cell can be decoupled, yielding the *noninteracting cell-cell adsorption* regime (NICCA).

Interesting limit cases can be identified in the diagram. For large values of the cell size, $\alpha \rightarrow \infty$, or small values of cell-cell separation, $\beta \rightarrow 0$, adsorption conditions are similar to the case without the pattern, so we denote as continuum limit. On the other hand, when SPCA and NICCA are considered, only one particle can be adsorbed per cell and there is no “interaction” between cells. This adsorption regime is similar to the adsorption of particles on a lattice (lattice like limit). For vanishing values of cell size ($\alpha \rightarrow 0$) and values of cell-cell separation above 1 ($\beta \geq 1$), the system is equivalent to a square lattice with a lattice constant of β . Another limit occurs for $\beta < 1$ and $\alpha \rightarrow 0$, which corresponds to a well-defined square lattice structure for the deposition of disk centers. Since each adsorbed particle effectively “shades” a circle of unit radius, which is larger than the lattice constant $\beta < 1$, deposition does not correspond to that of monomers as compared to the NICCA-SPCA case discussed above, as the adsorbed particle will surely block neighboring cells, and possibly more remote ones, depending on the value of β . For values of $\beta = 0$ the system no longer has a pattern, regardless of the value of α . The corner of the phase diagram near the point $(\alpha, \beta) = (0, 0)$ is special, but we did not consider this region because it is more mathematically interesting than physically relevant: see recent literature on the kinetics of this type [143, 144].

Throughout the next two sections, the effect of the considered pattern on both the jammed-state structure and adsorption kinetics is discussed.

4.3 The jammed state

The considered system is not in equilibrium, therefore the obtained structure is dependent on the kinetic evolution of the system. In the present section the jammed-state structure of the film for different regions of the diagram is described and the discussion of the kinetic evolution is postponed to the next section.

Let us focus on the jammed-state structure. As discussed in Sec. 4.2, depending on the cell-cell distance, two different regions of the two-parameter diagram can be defined: NICCA and ICCA. The first two subsections are devoted to the jammed-state coverage and to a general discussion of the morphology, based on snapshots, for these two different regions. In the third one, the interparticle distribution function is defined to analyze the effect of the pattern on the particle-particle correlations.

4.3.1 Noninteracting cell-cell adsorption

If cells are too far apart from their nearest neighbors, then particles at different cells will not be able to “see” each other through excluded volume. Specifically, for a cell-cell distance $\beta \geq 1$, particles (disks) attempting adsorption cannot overlap other disks, previously adsorbed, in neighboring cells. We denote such regime *Noninteracting cell-cell adsorption* (NICCA) in opposition with the *Interacting cell-cell adsorption* (ICCA) where adsorption attempts can fail due to the excluded volume interaction with particles adsorbed on other cells.

In this subsection we consider the NICCA case defined by $\beta \geq 1$. Since no interaction occurs between particles on different cells, the kinetics of adsorption decouples into independent local kinetics at each landing cell. Therefore, for this range of β values, the model is equivalent to continuum RSA on finite-size substrates, with somewhat unusual boundary conditions that a particle can “stick out” of the finite $\alpha \times \alpha$ region as long as its geometrical center is within the cell.

As explained above, based on the number of particles that can fit inside a cell, two

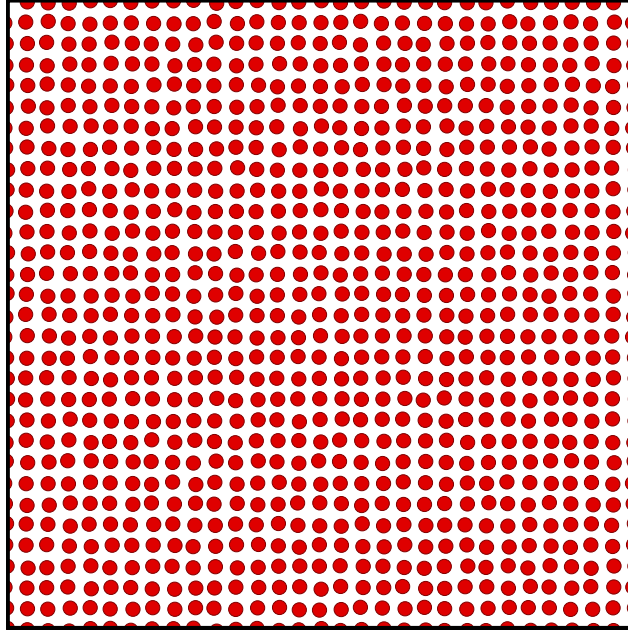


Figure 4.4: Typical configuration of a region of 30×30 unit cells, for $\alpha = 0.6$ and $\beta = 1.2$ at the jammed state. This snapshot corresponds to the NICCA-SPCA, upper-left, region in Fig. 4.3.

different regimes can be described, the SPCA, for $\alpha < 1/\sqrt{2}$ and the MPCA, for values of $\alpha \geq 1/\sqrt{2}$. For the SPCA and NICCA, kinetics corresponds to that of lattice RSA of monomers, since each cell is certain to have a single particle at the jammed state. The difference relative to the lattice RSA is in the particles position, which here are uncertain within the order of the size of the cell. In Fig. 4.4 is a snapshot of a typical configuration for such region of the two-parameter diagram. While perhaps theoretically least interesting, such patterning provides for the most “controlled” particle adsorption in applications. Since each cell ends up having a single particle, the jammed-state coverage, defined by eq. (4.1), is simply

$$\theta_J(\alpha, \beta) = \frac{\pi}{4(\alpha + \beta)^2}, \quad (4.5)$$

which holds for $\beta \geq 1$ and $0 \leq \alpha < 1/\sqrt{2}$.

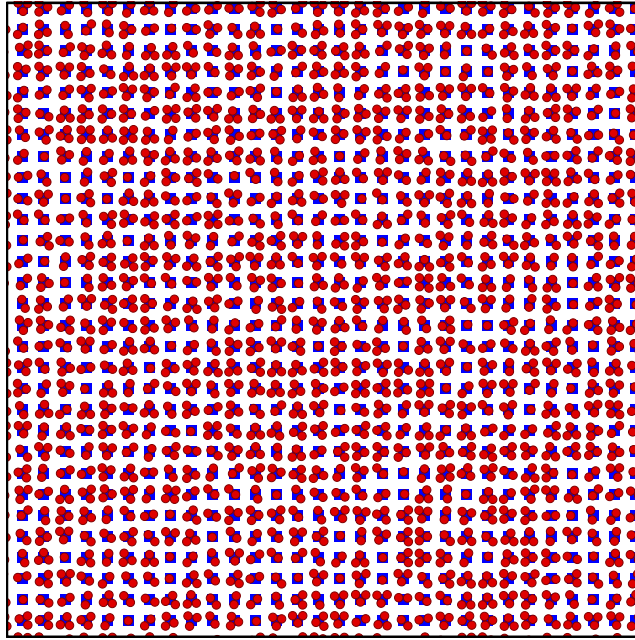


Figure 4.5: Typical configuration of a region of 30×30 unit cells, for $\alpha = 1.2$ and $\beta = 1.2$ at the jammed state. Particles attempting adsorption never overlap previously adsorbed ones in different cells, but contrary to Fig. 4.4 each cell can now adsorb more than one particle. Since $\beta = 1.2 > 1$, the kinetics of adsorption at each cell is decoupled from that at other cells. This snapshot corresponds to the NICCA-MPCA, upper-right, region in Fig. 4.3.

In the regime of NICCA with MPCA, a possibility opens up for having more than one particle being adsorbed in each cell. In Fig. 4.5 is a snapshot of a configuration for such regime. As in the SPCA case, kinetics of adsorption is *decoupled* in the sense explained above, therefore one can make some conclusions regarding the coverages for a given number of particles. Let us consider the case up-to-two particles per cell as an example, which is obtained for values of α in the range $1/\sqrt{2} \leq \alpha < (1 + \sqrt{3})/2\sqrt{2}$. The coverage of the close-packed (maximally packed) configuration is given by $\pi/2(\alpha + \beta)^2$ for two particles per cell and for $\beta \geq 1$. The closed packed means that all the cells have exactly the maximum number of particles adsorbed in (in the present case each cell accommodates two particles). Such closed-packed coverage will change discontinuously at $\alpha = (1 + \sqrt{3})/2\sqrt{2}$, as illustrated in Fig. 4.6. However, our numerical results, also in the

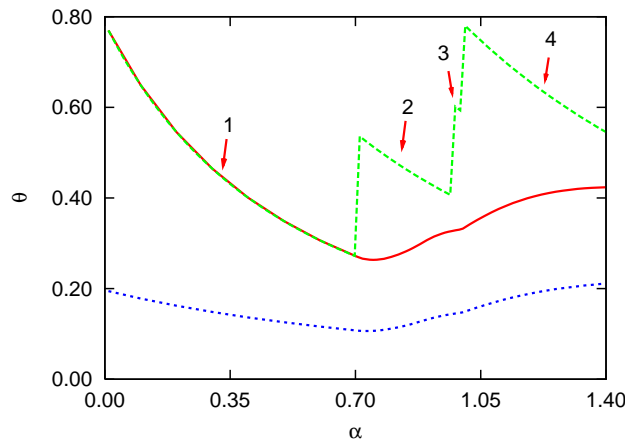


Figure 4.6: Coverage values obtained by Monte Carlo simulation of our RSA model (red solid line, the jammed-state coverage) and by direct calculation for the close-packed configurations (green dashed line), both for $\beta = 1$. Notice the discontinuities in the values of the close-packed coverage as opposed to the smooth variation in the RSA case. The jammed-state coverages for $\beta = 2$, calculated according to relation (4.6), are also shown for comparison (blue dotted line).

same figure, indicate that the value of the jamming coverage for the RSA model, which for more than one particle per cell, is less than the maximal coverage (closed-packed one), remains continuous at such value of cell size and also at $\alpha = 1/\sqrt{2}$, for which more than one particle can adsorb. This behavior continues for larger number of particles per cell, see Fig. 4.6. In the close-packed problem, the highest coverage, at fixed β , occurs for the smallest cell, i.e., the smallest value of $\alpha = \alpha_n$ allowing the prescribed number of particles, n . As expected, Fig. 4.6 illustrates the discontinuous coverage increments at α_n , followed by a decrease $\propto (\alpha + \beta)^{-2}$.

The simulated results for θ_J in the SPCA regime follow the close-packed values, since the two problems coincide in this α range. However, at $\alpha = \alpha_2$ the RSA coverage is continuous, since the probability of having a second adsorbed particle in any given cell remains small for values of cell size slightly above α_2 . This property reflects the stochastic nature of the RSA model, i.e., in most cases the first particle adsorbs at a position inside the cell that blocks the chance for the second particle to adsorb later. A similar observation

Table 4.1: The table shows the jammed coverage values in the NICCA-MPCA case, i.e., for $\beta \geq 1$ and $\alpha \geq 1/\sqrt{2}$. In the first column, n is the number of particles per unit cell of the close-packed situation. The values of α_n , defined in the text, are shown in the second column. The third column gives the close-packed coverage values for the range of up-to- n particles per cell. In the fourth column, the jamming coverage values, θ_J , from simulations are presented. These values are for a representative choice $\beta = \beta^* = 1.2$ (see text), and for the α values shown in the second column. Finally, in the fifth column, the standard deviation, σ_J , of the jamming coverages is given.

n	α_n	θ_n	$\theta_J(\alpha_n, \beta^*)$	$\sigma_J \times 10^4$
2	$\frac{1}{\sqrt{2}}$	$\frac{\pi}{2(\alpha+\beta)^2}$	0.21594	0
3	$\frac{1}{2\sqrt{2}}(1 + \sqrt{3})$	$\frac{3\pi}{4(\alpha+\beta)^2}$	0.26901	1.7
4	1	$\frac{\pi}{(\alpha+\beta)^2}$	0.27471	1.7
5	$\sqrt{2}$	$\frac{5\pi}{4(\alpha+\beta)^2}$	0.36148	1.0
∞	∞	$\frac{\pi}{2\sqrt{3}}$	0.547067	0.38

applies as α crosses $\alpha_{n=3,4,\dots}$. Our numerical results for θ_J were actually obtained for a representative β value, $\beta^* = 1.2$. The coverage for any other $\beta \geq 1$, for a given fixed value of α , can then be calculated from

$$\theta_J(\alpha, \beta) = \left(\frac{\alpha + \beta^*}{\alpha + \beta} \right)^2 \theta_J(\alpha, \beta^*) . \quad (4.6)$$

The standard deviation of the coverage is given by

$$\sigma_J(\alpha, \beta) = \left[\frac{\sum_{i=1}^N \theta_{Ji}^2}{N} - \left(\frac{\sum_{i=1}^N \theta_{Ji}}{N} \right)^2 \right]^{\frac{1}{2}} , \quad (4.7)$$

where the index i numbers the Monte Carlo runs, and N stands for the total number of runs. From this definition, after some algebra one can show that

$$\sigma_J(\alpha, \beta) = \left(\frac{\alpha + \beta^*}{\alpha + \beta} \right)^2 \sigma_J(\alpha, \beta^*) . \quad (4.8)$$

The above observation and the appropriate parameter and coverage values are summarized in Table 4.1, which in particular gives jamming coverage values $\theta_J(\alpha_n, \beta^*)$.

The jamming coverage values, obtained through simulation, for varying α are given in Table 4.2. In the present RSA problem, for $\beta = \beta^* = 1.2$ the minimum of the coverage is $\theta_{J_{\min}} = 0.21199 \pm 0.00006$, and it occurs for $\alpha_{\min} = 0.745 \pm 0.005$. Finally, in the limit $\alpha \rightarrow \infty$ one recovers the well-known RSA of disks on continuum substrates [121, 125, 126, 128, 175, 180, 222, 223, 224, 225].

Our value for the coverage is 0.5470669 ± 0.0000012 , which should be compared to the range 0.54700 ± 0.00006 recently estimated in [226]. Our estimation was obtained with a system size of 4096×4096 particle diameters and averaged over 10^3 samples. The respective close-packed value is $\pi/2\sqrt{3}$, corresponding to the α_∞ case in Table 4.1.

4.3.2 Interacting cell-cell adsorption

In the previous subsection we discuss the NICCA regime. In the present one, we discuss the ICCA case where adsorption is constrained not only by the pattern but also by particles, previously, adsorbed. Such particles can be adsorbed either within the same cell, where adsorption attempt takes place, or in different cells. Due to the interaction between particles in different cells, correlation can develop beyond single cells.

At this point, the discussion focus in the jammed-state coverage and morphology snapshots. A more detailed description of particle-particle correlations is postponed to the next subsection where the interparticle distribution function is discussed in detail.

To analyze the effect of the pattern on the jammed state structure in the ICCA regime, as was already done for the NICCA case, we perform extensive Monte Carlo simulations of our extended version of the RSA model. A system size of 500×500 unit cells is considered, unless otherwise stated, and periodic boundary conditions were applied both horizontally and vertically to reduce the finite-size effects. Results have been average over 10^2 samples. As stated in the beginning of the present chapter, we leave the discussion of the efficient algorithm to an individual section in the end of the chapter. At this point we just want

Table 4.2: Tabulation of numerically simulated RSA jammed-coverage values, at fixed $\beta = \beta^* = 1.2$, for the range of α from 0.72 to 1.40. The standard deviations are also shown.

α	θ_J	$\sigma_J \times 10^4$
0.72	0.21360	0.2
0.74	0.21204	0.5
0.75	0.21208	0.6
0.76	0.21259	0.8
0.78	0.21486	1.1
0.80	0.21856	1.3
0.82	0.22346	1.5
0.84	0.22934	1.6
0.85	0.23257	1.6
0.86	0.23598	1.5
0.88	0.24339	1.6
0.90	0.25130	1.7
0.92	0.25820	1.8
0.94	0.26332	1.6
0.95	0.26596	1.9
0.96	0.26794	1.7
0.97	0.26969	1.7
0.98	0.27117	1.6
0.99	0.27262	1.5
1.02	0.28321	1.8
1.04	0.29127	1.6
1.05	0.29518	1.9
1.06	0.29893	1.8
1.08	0.30621	1.9
1.10	0.31291	2.0
1.12	0.31918	1.9
1.14	0.32486	1.8
1.16	0.33013	1.9
1.18	0.33484	1.8
1.20	0.33908	1.4
1.22	0.34290	1.8
1.24	0.34624	1.4
1.26	0.34918	1.6
1.28	0.35178	1.4
1.32	0.35593	1.3
1.34	0.35755	1.3
1.36	0.35889	1.2
1.38	0.36002	1.2
1.40	0.36096	1.3

Table 4.3: The table shows simulated values of the coverage, θ_J , and the corresponding standard deviation σ_J , for several values of α and β , in the ICCA-SPCA and ICCA-MPCA regions of the “phase diagram” shown in Fig. 4.3.

α	β	θ_J	$\sigma_J \times 10^4$
0.1	0.14	0.5377	13
0.2	0.2	0.50866	7.6
0.2	0.28	0.54865	6.7
0.2	0.5	0.46563	5.0
0.2	0.8	0.54499	3.1
0.3	0.42	0.48338	5.2
0.4	0.2	0.52428	5.2
0.4	0.56	0.54519	3.9
0.5	0.7	0.54326	0.6
0.6	0.2	0.53444	3.9
0.8	0.2	0.55103	2.9
0.8	0.8	0.33358	1.5
1.0	0.2	0.53529	2.5
1.0	0.8	0.39362	2.4
1.2	0.2	0.53725	2.3
1.2	0.8	0.45497	2.4

to stress that the used algorithm allow a detailed study of the jammed-state structure.

In Table 4.3 are reported the values of coverage and the corresponding standard deviations for the various cases studied in the present regime. The ICCA regime is obtained for $\beta < 1$. As opposed to the NICCA case, in ICCA the kinetics of adsorption is no longer “decoupled”, and particles, or clumps of particles, that belong to the same landing cell, not only follow the square positioning pattern of the landing cells but can also become correlated with particles in other cells. The resulting film morphology and degree of ordering will depend on the geometrical parameters, as well as on the fully irreversible nature of the RSA model. In fact, depending on the values of α and β , particles attempting adsorption can overlap others that belong to cells more distant than the nearest-neighbor cells of the landing one. Therefore, in addition to the jammed-state coverage, a more detailed study in the ICCA regime should also involve consideration of particle-particle

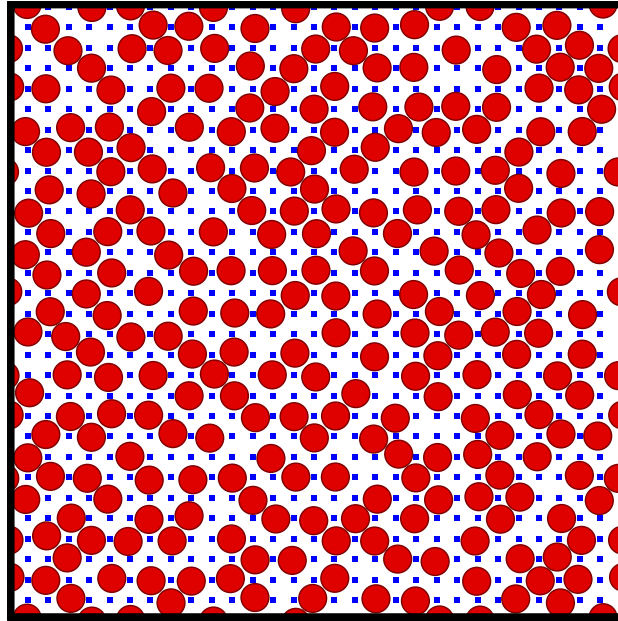


Figure 4.7: Configuration of a region of 30×30 unit cells, for $\alpha = 0.2$ and $\beta = 0.5$, at the jammed state. A particle attempting adsorption can overlap a previously adsorbed particle in a different cell. This excluded volume interaction is responsible for correlations which result in locally-diagonal, semi-ordered domains as seen in this snapshot. Such snapshots corresponds to the ICCA-SPCA, lower-left, region of the diagram (Fig. 4.3).

correlations in the jammed state, as addressed in the next subsection.

Following the strategy of NICCA discussion, we split the ICCA regime into two different subregions of the two-parameter diagram: SPCA and MPCA. Combining ICCA with SPCA, which holds for parameter values $\beta < 1$ and $\alpha < 1/\sqrt{2}$ and corresponds to the lower-left region in Fig. 4.3, can lead to particle configurations correlated beyond the pattern cell. Therefore, the obtained film yields nontrivial local particle arrangements. The resulting morphologies stem not only from the pattern, but also, from the cooperative interaction between particles during adsorption. Visually, see Fig. 4.7, the “crystallites” are oriented along the diagonal direction of the square lattice of pattern cells. However, it is well known [175, 177, 178] that the RSA process alone (i.e., without the pattern) cannot impose long-range ordering. Indeed the particle correlation in RSA are usually rather short range. The obtained order can extend over several lattice spacings. More generally,

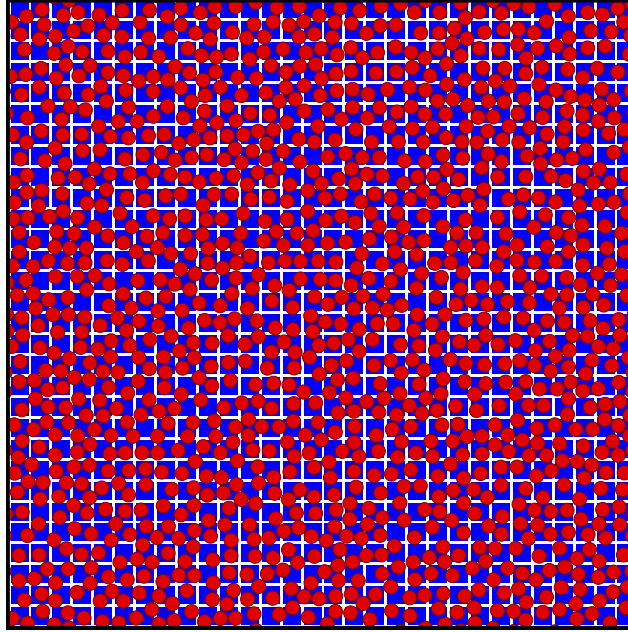


Figure 4.8: Configuration of a region of 30×30 unit cells, for $\alpha = 1.2$ and $\beta = 0.2$, at the jammed state. Such snapshots corresponds to the ICCA-MPCA, lower-right, region of the diagram (Fig. 4.3). For this low β value, the probability of a particle attempting adsorption to overlap with one in a neighboring cell is appreciable, thus building up a somewhat longer range diagonal semiordering than that seen for the parameter values of Fig. 4.7.

the ordering should also depend on the shape of the deposited objects [135, 179]. The pattern does influence the creation of ordered structures in an otherwise uniform deposition process. However, the stochastic RSA dynamics and the adsorption irreversibility tend to prevent the long-range order of the pattern from being fully “imprinted” in the deposited particle configuration, as observed in Fig. 4.7.

Combining ICCA with MPCA, which stands for $\beta < 1$ and $\alpha \geq 1/\sqrt{2}$, corresponds to the lower-right region of the diagram in Fig. 4.3. In this regime, the excluded volume interaction can lead to deposit morphology with semiordering beyond a single cell. However, the overlap with particles in the neighboring cells can extend at most up to the second-nearest-neighbor cells (diagonally neighboring cells). Consequently, smaller the cell size more relevant the cell-cell exclusion effect. The cell-cell exclusion leads to a

further reduction of the average cell population, illustrated in Fig. 4.8, where $\alpha = 1.2$ and $\beta = 0.2$. For these values of the parameters, each cell has enough area to accommodate up to four particles, but excluded volume interaction due to nearest-neighbor cells for this low value of β substantially lowers the average cell population, as compared, e.g., with that of Fig. 4.5 for $\alpha = 1.2$ and $\beta = 1.2$: the average number of particles per cell in the case of $\beta = 1.2$ is 2.487 ± 0.001 , while that of $\beta = 0.2$ is 1.3407 ± 0.0006 . Notwithstanding, the case of $\beta = 0.2$ still has a higher value of the coverage, 0.5373 ± 0.0002 , while for $\beta = 1.2$ the value of the coverage is lower, 0.3391 ± 0.0001 , because of more void space in the inter-cells region.

4.3.3 Interparticle distribution function

So far, discussion was focused on the coverage efficiency and qualitative descriptions of the structure based on representative snapshots. To further characterize the jammed state, we introduce the distribution function of the distances, r , between the centers of adsorbed particles, $P_{rad}(\alpha, \beta; r)$.

The system is translationally invariant in terms of the integer multiples of the unit cell size (α, β) , because we use periodic boundary conditions both horizontally and vertically. Therefore, instead of particle centers positions, only displacement vectors between particle centers matter when studying particle-particle correlations. For convenience, in order to avoid discussion of the “connected” part vs. the full correlation function, we normalized the correlations by counting only distances between pairs of particles within a cutoff distance, R . The distances r and R will be assumed dimensionless, measured in units of the particle diameter. We found it appropriate to limit our study to separations up to $R = 5(\alpha + \beta)$.

Since we are interested in the tendency for semi-ordering on length scales of several unit cells, we found it convenient to define

$$P_{rad}(\alpha, \beta; r) = \frac{\text{Number of pairs of particles with distances in } (r, r + dr)}{r dr (\text{Total number of pairs of particles at distances } < R)} . \quad (4.9)$$

This distribution function is normalized as follows,

$$\int_0^R P_{\text{rad}}(\alpha, \beta; r) r \, dr = 1 \quad . \quad (4.10)$$

The shape of the distribution function at the jammed state depends on the values of α and β . The position of the first peak measures typical distances between the closest particles. To better understand the role of α and β , we considered three families of distribution functions, as defined in the following subsections: effect of varying α , effect of varying β , and behavior along $\beta = \sqrt{2}\alpha$.

Effect of varying α on the distribution function

We start by studying the influence of varying the cell size, α , on the semi-ordering of the jammed state. We carried out a series of simulations at fixed $\beta = 1.2$ and varied α . The results are shown in Fig. 4.9(a). The dimensionless center-center distance, r —the horizontal axis of the plot—was further rescaled in terms of the unit cell size, to $r/(\alpha+\beta)$, see Fig. 4.9.

Keeping $\beta \geq 1$, here $\beta = 1.2$, corresponds to the NICCA case. In the NICCA-SPCA case, the first peak appears at a unit (rescaled) distance, since the distance to the closest particle, on average, is that to the nearest-neighbor cell. For NICCA-SPCA, well-defined peaks also appear that correspond to other underlying lattice distances defined by the square-lattice pattern. This is apparent in the distribution functions for $\alpha = 0.2, 0.4$, shown in Fig. 4.9(a), with peaks at distances of 1.0, $\sqrt{2} \approx 1.4$, 2.0, and $\sqrt{5} \approx 2.2$, etc. Increasing the value of α in the NICCA-SPCA regime increases the uncertainty in the position of the particle within the cell, i.e., it leads to peak broadening.

Now, in the NICCA-MPCA case, the position of the first one or more peaks depends on the value of α for a given value of $\beta = 1.2 > 1$; also shown in Fig. 4.9(a). Additional peaks will reflect the intra-cell particle distribution and can be positioned well below the unit-cell size. Peak broadening and peak-peak overlap are superimposed in this case, but the pattern-induced tendency for semi-ordering is still quite visible in the appropriate

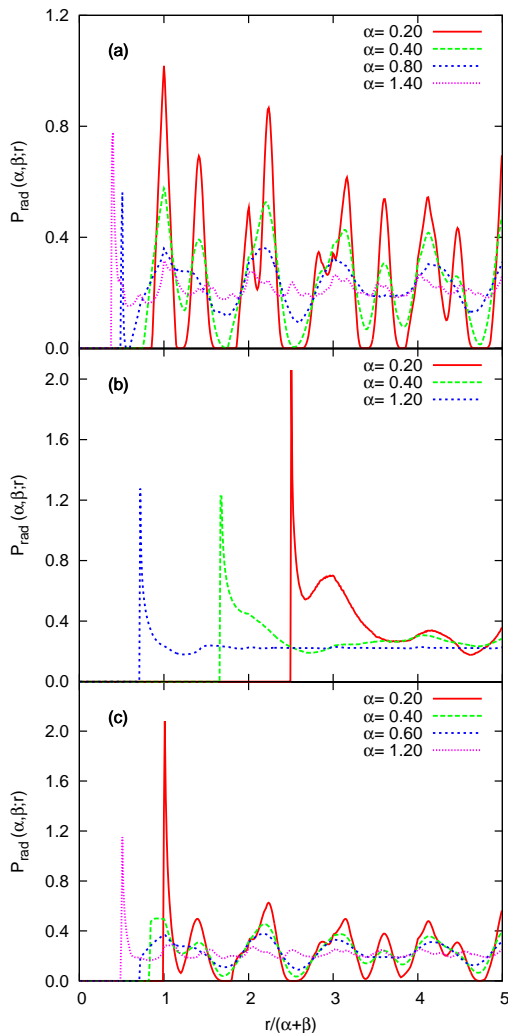


Figure 4.9: Plots of the distribution function for various values of α , at fixed values of β : (a) $\beta = 1.2$, with $\alpha = 0.2, 0.4, 0.8$, and 1.4 ; (b) $\beta = 0.2$, with $\alpha = 0.2, 0.4$, and 1.2 ; (c) $\beta = 0.8$, with $\alpha = 0.2, 0.4, 0.6$, and 1.2 .

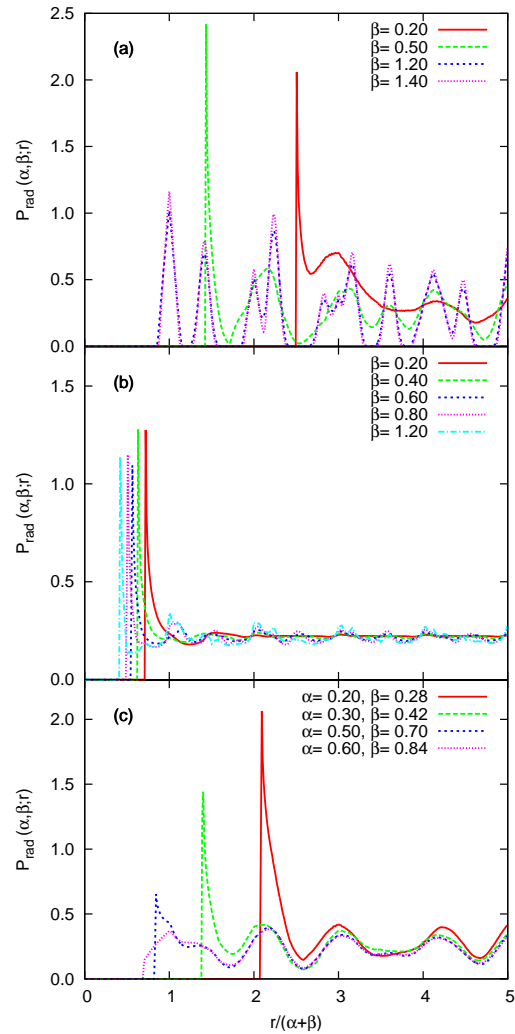


Figure 4.10: The distribution function (a) for constant $\alpha = 0.2$, with $\beta = 0.2, 0.5, 1.2, 1.4$; (b) for constant $\alpha = 1.2$, with $\beta = 0.2, 0.4, 0.6, 0.8, 1.2$; (c) along the diagonal line $(0, 0) - (1/\sqrt{2}, 1)$ in the ICCA-SPCA region of the (α, β) “phase diagram,” Fig. 4.3, with $(\alpha, \beta) = (0.2, 0.28), (0.3, 0.42), (0.5, 0.70), (0.6, 0.84)$.

curves for $\alpha = 0.8, 1.4$ in Fig. 4.9(a).

In the ICCA case, the structure and the position of the first peak will be more complex due to the possibility of overlap of an incoming particle with others belonging to neighboring cells. In terms of the distribution function, the presence of the excluded volume interaction has an interesting effect of smoothing out the lattice-induced tendency for ordering, as shown in Fig. 4.9(b). The effect is particularly noticeable when one compares these plots with those for the same values of α in Fig. 4.9(a). The features of the distribution function seem to be determined primarily by the particle-particle jamming effects, rather than by the underlying landing-cell pattern.

Finally, for $\beta = 0.8$, though the interaction between particles at different cells is present, it is not as prominent as for $\beta = 0.2$, and one observes an intermediate behavior, as shown in Fig. 4.9(c). The distribution function is still smoothed out due to the jamming effects between particles at different cells, but traces of the lattice-induced ordering remain, specially for $\alpha = 0.2, 0.4$.

Effect of varying β on the distribution function

To discuss the effect of the value of β on the structure of the jammed state, let us first consider fixed $\alpha = 0.2$, with varying $\beta = 0.2, 0.5$, and 1.2 , as shown in Fig. 4.10(a). One observes that, as β increases, the distribution function becomes more detailed with peaks becoming sharper. There is also peak splitting, related to a lesser degree of excluded volume interaction between a particle attempting adsorption and another one from a different cell. We comment that for values of $\beta \geq 1$ the general shape of the radial distribution function is no longer changing, since particles cannot overlap.

The excluded volume interaction with particles belonging to neighboring cells also reduces the number of particles effectively adsorbed in a cell as observed in snapshots of the jammed state in Figs. 4.5 and 4.8, with α fixed at 1.2 , while β changing from 1.2 to 0.2 , respectively.

For $\alpha = 1.2$ and for increasing values of β in the interval $(0, 1)$, one observes that the

radial distribution function reflects more structure from particle arrangements inside the cells, see Fig. 4.10(b). As β increases, the position of the first peak also shifts to lower values. However, as far as the pattern-induced ordering is concerned, very little trace is left of it, and the curves are relatively flat, dominated by particle-particle jamming effects.

Jammed-state structure along $\beta = \sqrt{2}\alpha$

As our last example, we consider the effect of changing both α and β along the diagonal of the ICCA-SPCA region, which corresponds to values of $0 < \alpha < 1/\sqrt{2}$ and $0 < \beta < 1$. Here particles are larger than the cells and they can overlap particles from neighboring cells, not necessarily the nearest-neighbor ones. In the ICCA-SPCA regime, particle deposition leads to highly correlated jammed structures.

Though not specifically taken along the diagonal line, a snapshot of such a highly-correlated jammed state can be seen in Fig. 4.7. As a rule, the tails of the distribution functions, see Fig. 4.10(c), mostly coincide regardless of the values of both α and β . This simply reflects the fact that these correlations are dominated by the excluded-volume jamming effects, rather than by the landing-cell pattern. However, correlations up to (scaled) distances of ~ 2.5 units do show parameter-dependent features. Specifically, the position of the first peak shifts to lower values of the distance, since the relative size of the particles compared to that of the unit cells decreases for increasing values of α (or β).

4.4 Adsorption kinetics

Previously, we have discussed the jammed-state structure obtained through adsorption under the constrain of a pattern. In the present section, we discuss the influence of the pattern on the adsorption kinetics. As stressed in Chapter 1, the obtained structures in far-from-equilibrium systems are strongly dependent on the time evolution of the film growth.

The kinetic evolution of the coverage toward the jammed-state value, in the RSA

model, is characterized by different functional dependence on- and off-lattice. For the lattice case, the coverage approach to the jamming limit is known to scales according to an exponential law [121],

$$\theta(\infty) - \theta(t) \sim \exp(-kt) \quad . \quad (4.11)$$

Off-lattice [175, 177, 178, 179, 227, 228], since vanishing-small areas available for adsorption can occur, the approach extends in a power-law,

$$\theta(\infty) - \theta(t) \sim t^{-\frac{1}{d}} \quad . \quad (4.12)$$

Such result was observed by Feder through computer simulations [175] and later explained by Pomeau [177] and Swendsen [178]. For disks with equal size, adsorbing on a clean/regular substrate, $d = 2$.

The pattern allows to interpolate between the continuum limit and the lattice like behavior, therefore it is important to identify where the transition occurs for the considered pattern as well as characterize it. The transition is expected to occur when there is no minimum finite area available for adsorption, meaning that vanishing-small areas can be obtained, with non-zero probability. In the ICCA-SPCA limit, since only one particle can fit per cell, the existence of minimum finite area is related with particles previously adsorbed on neighboring cells. When a particle is successfully adsorbed, due to excluded volume interaction, no more particles can adsorb in a circle with radius equal to 1 (units of particle diameter) centered in the particle center (“shadowed” region). If the “shadowed” region of four particles adsorbed on neighboring cells can completely overlap the cell (blocking adsorption), there is no minimum finite area available to accommodate one particle (see Fig. 4.11). On the other hand, if particles adsorbed on neighboring cells cannot lock adsorption inside the cell, a minimum finite area is obtained in the interception of the four “shadowed” regions. The transition occurs for values of α and β such that

$$\frac{\alpha}{2} + \beta = 1 \quad , \quad (4.13)$$

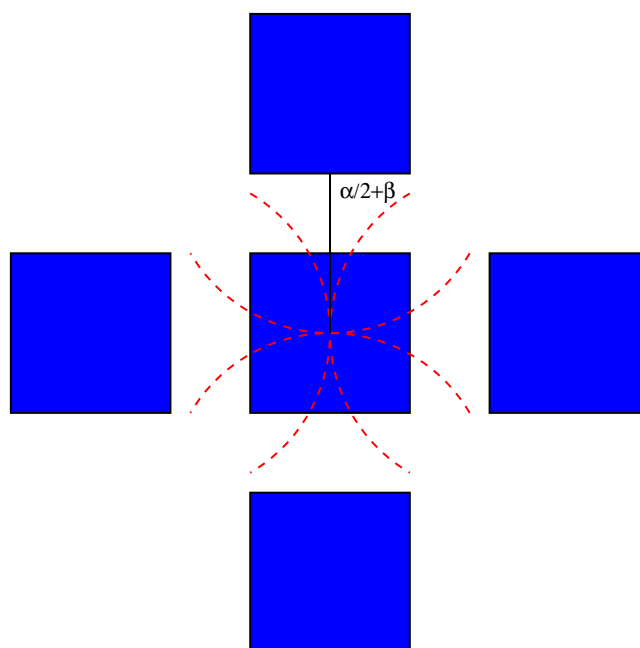


Figure 4.11: For ICCA-SPCA, a particle adsorbed in a neighboring cell can constrain particles adsorption on the central cell. For each adsorbed particle there is a “shadowed” region where no other particle center can adsorb. If the overlap of the shadowed regions of the four neighboring particles completely overlap the central cell, there is no minimum finite area available for adsorption and the average number of particles per cell will be less than one.

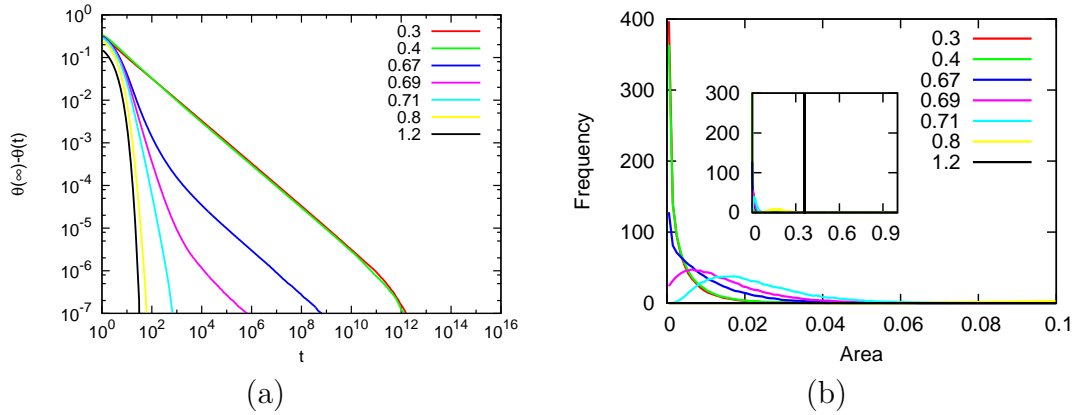


Figure 4.12: For fixed value of cell size ($\alpha = 0.6$) and different values of the distance between cells ($\beta = \{0.3, 0.4, 0.67, 0.69, 0.71, 0.8, 1.2\}$): (a) Approach of the coverage to the jamming limit as a function of time. (b) Distribution of empty, depositable, areas, before the jammed state.

where no minimum available area can be defined in the interception of four “shadowed” regions.

To characterize the transition, we fix the value of the cell size (α) in the SPCA regime and range the value of the cell-cell distance (β). For $\alpha = 0.6$, the critical value of β , given by equation (4.13) is 0.7. In Fig. 4.12(a) is the approach of the coverage to the jamming limit, for different values of β , as a function of time. For values of β below the critical value the approach scales as a power-law. Up to four particles adsorbed on neighbor cells are able to completely block the adsorption on the cell. Approaching the critical value, the power-law is only recovered for later times. The exponent is always $1/2$ as expected for adsorption of monodisperse particles on a clean substrate [175, 177, 178]. For values of β above the critical value, the coverage approaches the jammed state exponentially. A minimum finite area occurs in the interception of the four particles “shadowed” region. It is important to stress that we are reporting lattice like behavior even in the ICCA regime.

More insight into the system can be obtained with the distribution of empty, depositable, area (gaps). Such gaps are defined as regions where the geometrical center of a particle can land without overlapping a previously adsorbed particle. In Fig. 4.12(b)

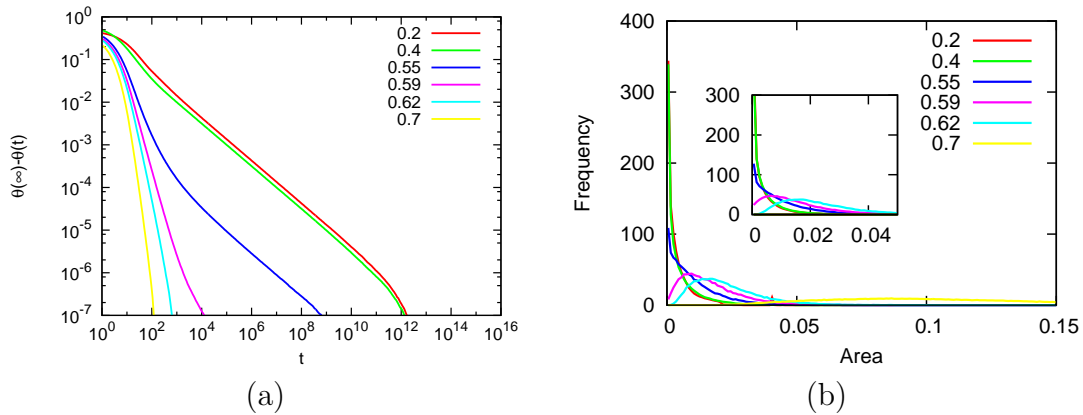


Figure 4.13: For fixed value of cell-cell separation ($\beta = 0.7$) and different values of the cell size ($\alpha = \{0.2, 0.4, 0.55, 0.59, 0.62, 0.7\}$): (a) Approach of the coverage to the jamming limit as a function of time. (b) Distribution of empty, depositable, areas.

is plotted the probability distribution of gaps available for adsorption before the jammed state is attained, for $t = 100$ for all values of β , except $\beta = \{0.8, 1.2\}$, where $t = 30$. Such difference is due to the fact that, for the exponential behavior, the jammed state is attained much earlier than in the power law side. When power law holds, a vanishing-small area can be obtained with non-zero probability. In the exponential side, the distribution is characterized by a minimum finite area. The minimum finite area corresponds to the interception of the four “shadowed” regions, eq. (4.13).

The same transition is observed when we fix the cell-cell separation (β) and range the values of cell size (α). We keep the value of $\beta = 0.7$ and range the values of α from 0.2 to 0.7, all in the SPCA regime, see Fig. 4.13. According to eq. (4.13), for such value of β the value of α where the transition occurs is 0.6. All the observed behavior for fixed cell size is observed (see Figs. 4.12 and 4.13).

As previously stated (see Sec. 4.3) [187], ranging the values of α and β , a rich set of morphologies is obtained at the jammed state. Consider the SPCA, in the NICCA regime, since adsorption on an empty cell is not constrained by particles previously adsorbed on a neighboring one, adsorption can occur, with equal probability, all over the cell. On the contrary, in the ICCA regime, the adsorption inside the cell is non-uniform. In Fig. 4.14 is

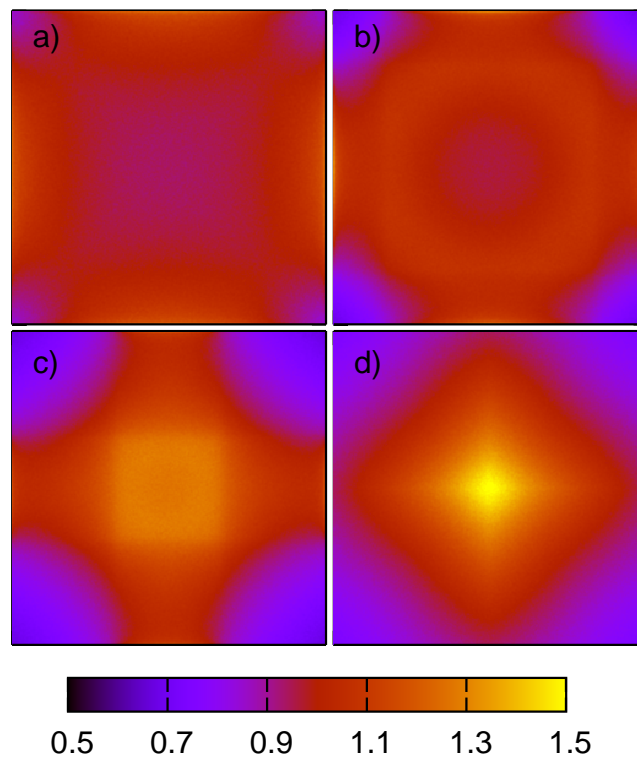


Figure 4.14: Spatial distribution of particles inside the cell, at the jammed state, for $\alpha = 0.6$ and for different values of β : (a) 0.4, (b) 0.5, (c) 0.6, and (d) 0.7.

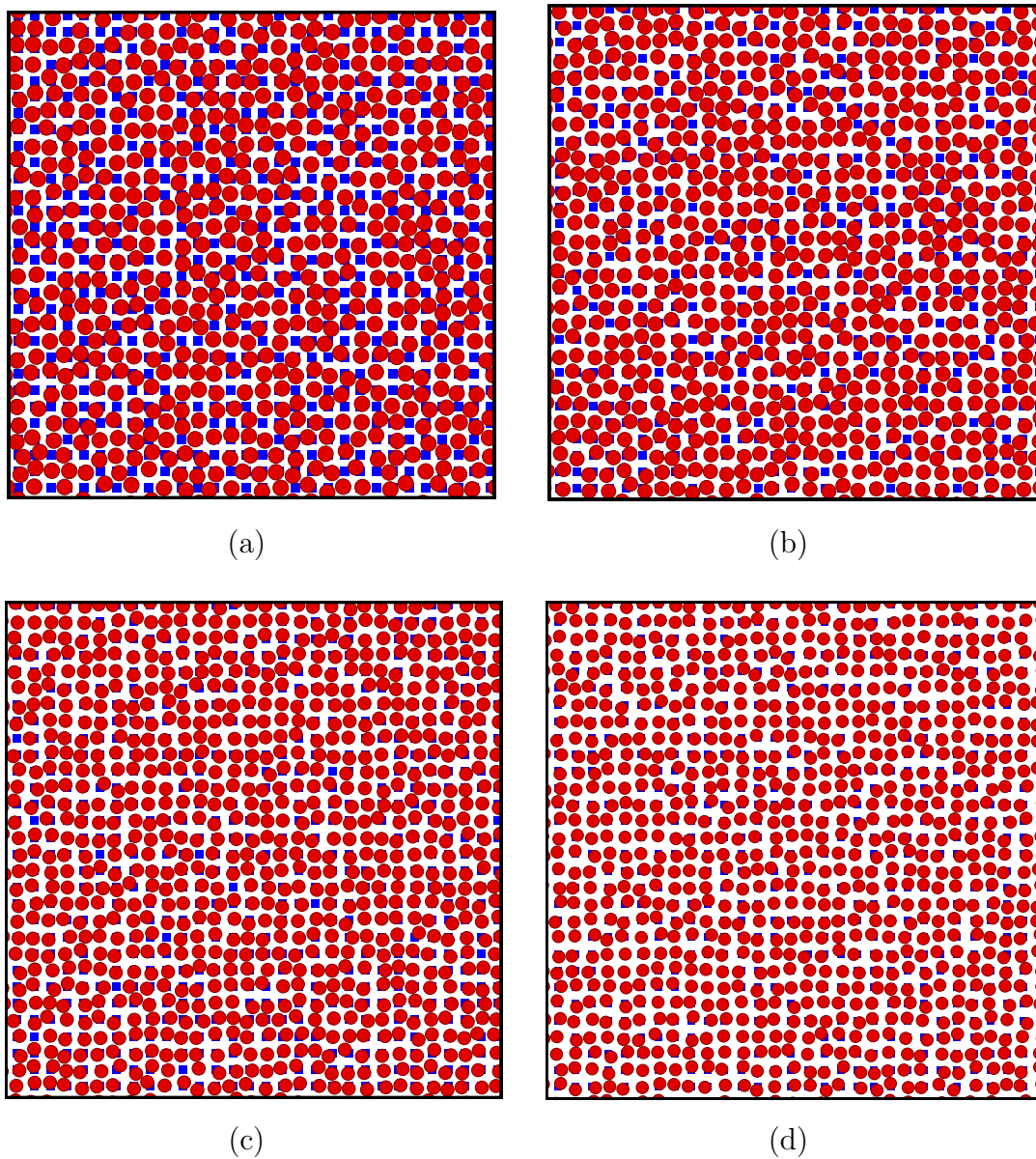


Figure 4.15: Snapshot of the jammed state with 30×30 unit cells, for $\alpha = 0.6$ and for different values of β : (a) 0.4, (b) 0.5, (c) 0.6, and (d) 0.7.

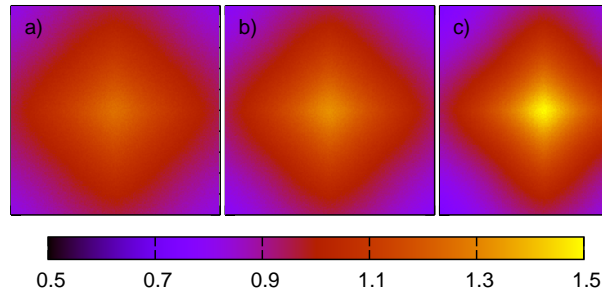


Figure 4.16: Spatial distribution of particles inside the cell for $\alpha = 0.6$ and $\beta = 0.7$ for different values of coverage: (a) 80%, (b) 90%, and (c) 99.9% of the jamming coverage.

plotted the spatial distribution of particles inside the cell, at the jammed state, for $\alpha = 0.6$ and different values of $\beta = \{0.4, 0.5, 0.6, 0.7\}$. Snapshots of the system, for different values of the two parameters, are in Fig. 4.15. For $\beta = 0.4$, particles adsorb preferentially at the cell edges. Approaching the critical value of $\beta = 0.7$, the probability of adsorption in the cell center increases. It is then relevant to understand how such behavior emerges in time.

For RSA on a clean substrate (without the pattern), Pomeau [177] proposes two steps for the dynamics. An initial stage where large holes are filled up so the progress is exponential, and a later one where small holes are filled, being power law. Particles adsorbed during the former step are distributed randomly in the cell. The structure of the spatial distribution of particles inside the cell is, then, defined by the latter step. When the adsorption constrain, due to the interaction between cells, is significant, the spatial distribution of particles inside the cell reveals preferential regions. In Fig. 4.16, are the spatial distributions of particles inside the cell for $(\alpha, \beta) = (0.6, 0.7)$, and for different values of the coverage, namely, 80%, 90%, and 99.9% of the jamming coverage. In Fig. 4.14(d) is the distribution at the jammed state. The preferential region in the center of the cell only becomes bold for later times, close to the jammed state.

The present results were obtained with computer simulations. A system size of $10^3 \times 10^3$ unit cells (of the pattern) was considered. Periodic boundary conditions were applied both horizontally and vertically. Regarding the number of samples, for the distribution of

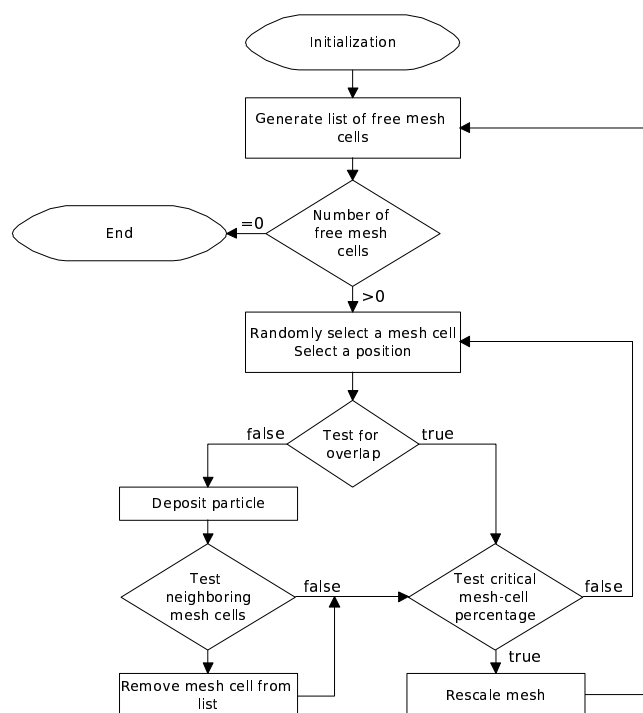


Figure 4.17: Scheme of the algorithm.

empty, depositable, area, it was different from case to case, based on the frequency (numbers) per bin of the distribution, such that a frequency of 10^3 cases per bin are obtained, assuming uniform distribution. For the remaining data, results have been averaged over 10^3 samples. Distributions were computed with 80 bins per unit area, yielding a resolution of 1.25% of the unitary area.

4.5 An efficient algorithm

In the present section, the algorithm developed to obtain the results discussed above, is presented (the algorithm is summarized in Fig. 4.17). Given the relevance of the RSA model, a general description is considered, which includes both the clean and patterned substrates.

Two different stage of the RSA process can be identified. At early times, the excluded

volume condition plays a weak role, since particle adsorption takes place almost uniformly on the substrate. At late times, the typical scenario involves a myriad of disconnected regions where adsorption can take place with areas (volume in general) varying across different orders of magnitude [177, 178] (see Figs. 4.12(b) and 4.13(b)). Therefore, a naive trial and error algorithm is far from efficient since the number of failed trials will drastically rise with the coverage.

Several algorithms have been introduced in the literature [179, 180, 225], which go beyond the naive trial and error one. For example, in the case of the adsorption of oriented squares on a surface, Brosilow et al. [179] were able to write a fail proof algorithm. In contrast, Privman et al. [180] and later Wang [225] introduced non-fail proof, though efficient versions for the deposition of disks on surfaces. Other studies included, for example, different particle shapes and size distributions [179, 180, 188, 224, 229, 230], competitive adsorption of different particle types [146, 224, 229], pre-treated substrates [128, 187, 217, 231], etc. Efficient algorithms are, thus, paramount to perform extensive simulations, particularly near the jammed state. Though we did not explicitly include the possibility of detachment [232], such a process can be effectively accounted for by performing the reverse actions necessary for a successful adsorption attempt.

An algorithm able to reach the jammed state is bound to offer more significant digits for the same amount of sampling and system size. In the present section, we introduce one such algorithm used and tested across a substantial set of study cases, which allows us to extend previously reported results and present new ones [121, 127, 128, 225, 146, 187, 188, 189]. The event-driven algorithm outlined in this work makes the attainment of the jammed state possible, since we use overlap conditions up to four particles. These overlap rules are general enough to allow size dispersion to be considered, regarding that a minimum and a maximum size is defined. The substrates can also be either clean, patterned, or pre-adsorbed.

4.5.1 Clean substrate

The main feature of the RSA problem regards its ability to describe physical phenomena that do not have mobility within experimental timescales. However, in order to make further progress, we adopt a terminology used in the field of colloidal particle adsorption, but the ideas and concepts are more general.

As described in the section about the model, the RSA model assumes that particles land uniformly (i.e., without any spatial dependence) on a substrate (in two dimensions). Everytime a particle attempts adsorption, such an attempt only succeeds if the landing particle does not overlap a previously adsorbed one. Once adsorbed, a colloidal particle will 'stick' to the substrate, i.e., it will not diffuse on or detach from the substrate [125], a regime known in the literature as irreversible adsorption.

Though the present chapter is devoted to the adsorption on patterned substrates, previous research have focused on studies of the irreversible adsorption on 'clean' (i.e., non-patterned or pre-treated) substrates [180, 184, 225]. Recall that studies of the jammed state require algorithms, which remain efficient at late times, i.e., the number of adsorption failures is as few as possible, without biasing the results. Therefore, a naive trial and error algorithm is a far-from-good option since it would blindly attempt adsorption of particles in the 'physical' perspective, i.e., without regard to substrate areas blocked from further adsorption by previously adsorbed particles.

The existence of a jammed state implies that the available area for adsorption decreases each time an adsorption occurs. Consequently, one naturally expects the time for such an algorithm to be limited by the smallest available area for adsorption at late times and, since such an area can be several orders of magnitude smaller than the total area, the efficiency decays by a factor of the order of the ratio of the total and the available areas. One cannot expect such algorithms to reach the jammed state, so coverage results represent lower bounds. To overcome such shortcomings, more efficient algorithms have been proposed [179, 180, 225]. The main idea is to perform adsorption attempts only at those regions where the available area for adsorption is maximized (we describe below how

this can be accomplished). We also point out that such improved algorithms are still of the trial and error type, but with a much better efficiency.

Finally, it is of interest to describe how the system approaches the jammed state. To this end, the time unit is naturally defined in terms of the number of particles necessary to cover the substrate, so that if a adsorption event for a particle of area a fails, the clock still ticks on average by a/A , where A is the substrate area. For example, for the specific case of adsorption of disks the time increment is obtained by eq. (4.2) as discussed above [121, 128]. The time increment after every adsorption attempt in the naive trial and error algorithm is proportional to such ratio. Using the idea of available areas for adsorption, the time increment between consecutive adsorption attempts is

$$\Delta t = -\frac{\ln(1 - Y_t) a}{\Lambda} , \quad (4.14)$$

where Λ represents the area engulfing all available areas for adsorption and Y_t is a uniformly distributed random variable in the interval $[0, 1[$. The former quantity includes not only the available area for adsorption, but also already blocked areas. Ideally, one would like to prevent blocked areas to be taken into account, but we show below that there are situations where the presence of such areas is either unavoidable or too cumbersome to be completely eliminated.

The equation above can be understood in the following way: the average number of landing attempts within the area Λ is proportional to Λ/A , while the time per attempt is given by a/A . Consequently, the time for a particle to land within the Λ region is given by a Poisson process with average time of a/Λ , i.e.,

$$P(\Delta t) = \exp\left(-\frac{\Lambda}{a}\Delta t\right) , \quad (4.15)$$

see eq. (2.15) and respective discussion. Similar ideas were also used by other authors [88, 179, 225].

The basic algorithm

For the sake of simplicity, we now present a basic description of the algorithm, while leaving more specific cases to later subsections of this section. Let us consider the continuum adsorption on a two-dimensional substrate (surface), but our considerations can be straightforwardly extended to higher spatial dimensions.

As above-mentioned, a simple minded overlap test based on previous adsorbed particles becomes particularly unfeasible at late times from the computational perspective. Using the idea of making deposition only on the available areas can actually increase the computational efficiency of the algorithm. A practical implementation includes the notion of a mesh cell, i.e., a discretization of the substrate into an array of square cells arranged in square lattice pattern. Such mesh cells are virtual in the sense that no physical meaning is associated with them, but they provide for an efficient way of identifying neighboring particles (i.e., previously adsorbed particles) [179, 184, 223, 225, 233]. The size of a mesh cell is such that a single particle completely inscribes it. As an example, in the case of disks of unit diameter, the linear size of the mesh cell, c , has to be $c < \sqrt{2}/2$, so we choose, $c = 1/2$ for simplicity.

To provide for a fast identification of neighboring mesh cells, each mesh cell can have three different states, namely, *occupied*, *shadowed*, or *free*. *Occupied* mesh cells are those with the center of an adsorbed particle inside it, while *shadowed* ones are those completely overlapped by one or more neighboring, adsorbed particles. *Free* mesh cells have, at least, a region within where adsorption is possible. It is clear that the area of all *free* mesh cells is simply Λ , which amounts to $n_f c^2$, where n_f is the number of *free* mesh cells. Up to this point we introduced the basic terminology necessary to understand how the basic algorithm works.

Let us now proceed towards the full description of the basic algorithm, especially in what concerns the role of the mesh cells. A list of all *free* mesh cells is used to draw adsorption attempts. A mesh cell belonging to this list is randomly chosen with uniform probability, with uniform random coordinates within the cell also drawn for the particle

center. If the particle does not overlap any previously adsorbed one, the attempt is successful. Otherwise, it fails and the substrate remains unchanged. In either cases, time is incremented using equation (4.14), which gives the appropriate time increment for each adsorption attempt. Here, we comment that Λ represents an area that is at least equal to the available area for deposition, but it is usually larger as some of the *free* mesh cells can be partially shadowed by neighboring (previously) adsorbed particles. This is why one still needs to test the landing particle for overlap. Nonetheless, such a procedure maximizes the number of successful trials.

In the event of a successful attempt the chosen *free* mesh cell becomes now *occupied* and neighboring mesh cells are tested for shadowing. In the latter case, shadowed mesh cells are all those where adsorption is no longer possible, which includes not only the ones overlapped by the adsorbing particle, but also the ones provided by the excluded volume interaction. For example, for the case of adsorption by disks of fixed radius, the overlapped cells are all those fully within a distance equal to the radius of the disk, but the excluded volume interaction eliminates also those within a radius twice that of the disk. Partially covered cells are kept *free*. It is now straightforward to observe that more stringent rules can be made on the classification of partially shadowed mesh cells. We will return to this subject later on.

The above procedure is iterated until one reaches a pre-defined critical number of *free* mesh cells, usually defined as a fraction of the initial total number of mesh cells. The actual value depends on the particularities of the problem at hand and the iteration level of the mesh cells. As one approaches the critical value, the population of *free* mesh cells are those with a reasonable shadowed area inside them. Upon reaching such a critical value, one rescales the size of each mesh cell by halving its linear size, i.e., the rescaled value of c is $c/2$. This procedure multiplies by four the initial number of mesh cells. However, in the new mesh, some of the mesh cells previously reported as *free*, will now have part of their offspring classified as *shadowed*. Consequently, the entire procedure removes shadowed areas from the pool of *free* mesh cells, thus enhancing the probability

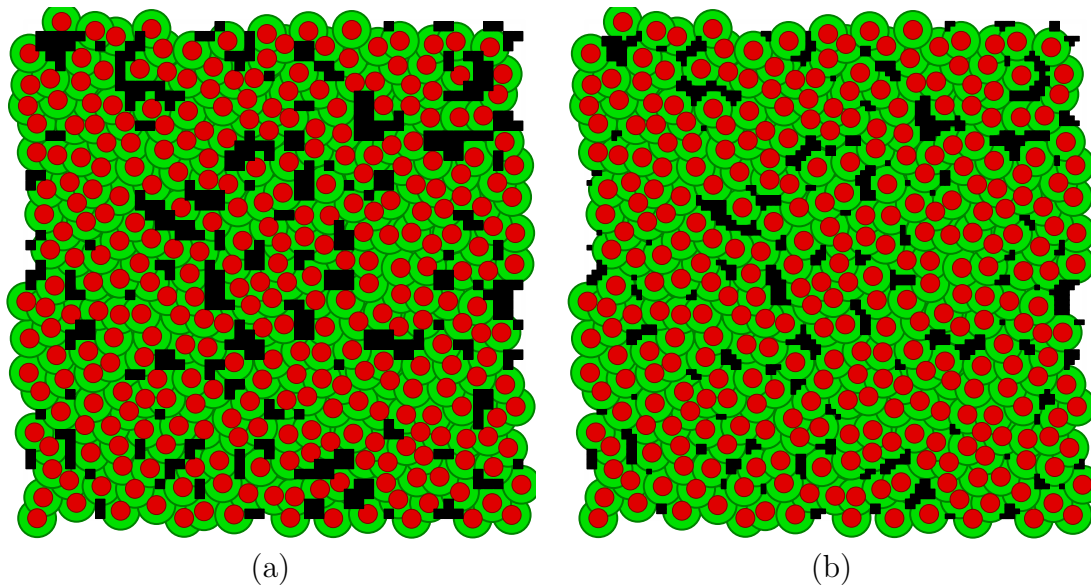


Figure 4.18: Snapshot of the system before and after rescaling. The black squares represent the free mesh cells. Without changing the coverage, a rescale of the mesh cell reduce the total area where adsorption attempts take place.

for successful attempts each time such a mesh cell is chosen from the list of *free* mesh cells (see Fig. 4.18).

As the adsorption attempts proceed, it is important to rescale the mesh size, if the number of failed attempts becomes high enough to favor the rescale procedure. Otherwise, it is computationally more efficient to remain at that iteration level of the mesh. This finalizes the explanation of the basic algorithm and we now proceed to describe the sufficient conditions for the elimination of mesh cells.

4.5.2 Mesh-cell test conditions

As mentioned previously, the conditions for changing the status of mesh cells from *free* to *shadowed* are fundamental to the efficiency of the algorithm. To this end, the set of overlap test rules must be as inclusive as possible. We mention that they can be applied to any particle size distributions as far as they allow for a positive minimum value of the radius, r_{\min} , and also a finite maximum value of the radius, r_{\max} .

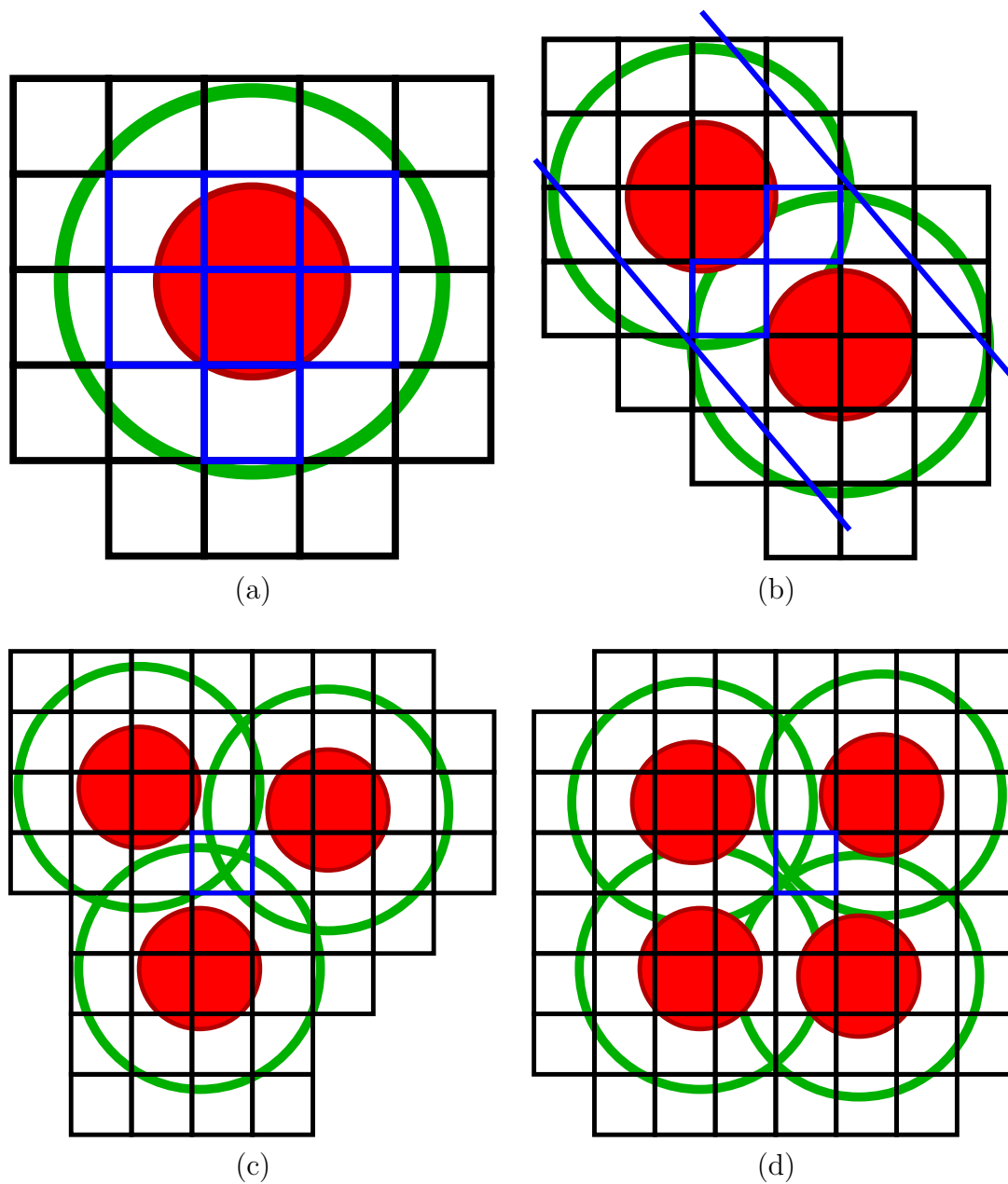


Figure 4.19: Scheme of shadow tests for (a) one particle, (b) two particles, (c) three particles, and (d) four particles. The blue cells are the ones that become shadowed due to the mesh-cell test.

Each rule involves a given number of particles, and in the present case we define rules involving up to four particles. In the case of a single particle, the condition is simply to have the four corners of the mesh cell inside the circle of radius $r + r_{\min}$, where r is the radius of the adsorbed particle, see Fig. 4.19(a). The two particles condition, Fig. 4.19(b), allows for further elimination of mesh cells. Such rule applies only to mesh cells partially shadowed by a particle with another one within a distance of $r + r_{\max} + 2r_{\min}$. The idea is to define a band consisting of two parallel straight lines along the centers connecting both particles and passing through the intersection points of the circles. All mesh cells with the four corners within the band and the center of the circles are eliminated. The rule involving three particles, Fig. 4.19(c), compounds on the previous one involving two. At the intersection of the two circles the two-particle rule fails, but the mesh cell can still be shadowed by the presence of a third particle at a distance $r + r_{\min}$. Finally, the case involving four particles, requires that the intersection points between two particles lie within the same mesh cell. The fourth particle must be a distance $r + r_{\min}$ across the band relatively to the third particle, see Fig. 4.19(d). The set of rules can be applied to various commonly studied cases such as the monodisperse, truncated Gaussian distribution, and binary mixtures [128, 187, 188].

4.5.3 Pre-patterned substrate

In the context of the present thesis, we consider as a pattern equal-size cells regularly distributed (see Fig. 4.1). Despite that, other patterns can also be considered as well as other arrangements. For example, a pattern can also consist of randomly placed regions like the hexagonal pits appearing on InGaN/GaN [234]. Another possibility is the study of adsorption on pre-adsorbed substrates [141, 217]. Meaning that film growth takes place in two stages, an initial one consisting of adsorption of one type of particles followed by a second stage where a different type attempts adsorption (see previous chapter). Typically, particles have different sizes and shapes, and the coverage at the end of the first stage does not necessarily have to reach the jammed-state value.

The presence of a pattern puts some restrictions in the algorithm by reducing the initial number of *free* mesh cells. Those mesh cells falling outside the pattern cells are immediately considered as *shadowed*. In terms of performance, it is important to eliminate adsorption attempts outside of any given cell by performing such test first and only consider the overlap test after. Everytime rescaling occur, the presence of the pattern must be considered when testing mesh cell offsprings for shadowing.

In the specific case of the pattern consisting of square cells mentioned above, one can perform the overlap test of the mesh cells by considering the actual available area for deposition instead that of the original mesh cell. This can be easily implemented by considering the vertices of the resulting rectangle after the original mesh cell being clipped by a given cell and use such coordinates as the effective ones for the overlap tests.

Contrary to the basic algorithm, to study adsorption on substrates without pattern, the pattern can fundamentally change its efficiency. As discussed above, the considered pattern can change the functional dependence of the coverage approach to the jamming limit from power-law to exponential. Note that, for certain regions of the two-parameter diagram (see Fig. 4.3) some more tailored algorithms can be developed. For example, when NICCA case is considered, the decoupling of the kinetics in different cells can be used to develop parallelized versions of the present algorithm.

4.5.4 Some results

The algorithm described allows us to obtain more significant digits for previously calculated results in the literature. Of course, apart from the intrinsic efficiency of the algorithm, there is also the gain in computer power since the time of their publication. Nonetheless, our results are truly pushed to the jammed state for each of the samples, i.e., no large enough space is left to accommodate one more particle. Otherwise stated, the number of samples for each data point is 10^3 samples and periodic boundary conditions apply both horizontally and vertically.

The first case regards adsorption of monodisperse disks on a clean substrate for a

Table 4.4: The table presents the jammed state coverage (θ_∞), the coverage error (σ_θ), and the computational run time (t_{CPU}), as a function of the linear system size (L), for 10^3 independent runs of monodisperse particles adsorption on clean/regular substrate.

L	θ_∞	σ_θ	$t_{\text{CPU}}(\text{s})$
16	54.670	0.031	47
32	54.673	0.015	318
64	54.6941	0.0080	1559
128	54.6985	0.0039	2577
256	54.6993	0.0019	9081
512	54.70054	0.00098	31889
1024	54.70612	0.00048	152672
2048	54.70650	0.00024	819996
4096	54.70669	0.00012	2047776

linear system size, L , of 4096 particle diameters. We obtain the value of the coverage as 54.70669 ± 0.00012 at a full jammed state. This value is substantially more precise than previously values of 54.70690 ± 0.00007 by Wang [225], 54.67 ± 0.03 by Meakin and Julien [224], 54.6 ± 0.2 by Hinrichsen et al. [223], and 54.73 ± 0.09 by Tanemura [222].

We present in Table 4.4 the values of the coverage as a function of the linear size of the system together with their respective statistical errors. In Fig. 4.20(a), it is plotted the coverage vs the linear size of the system. The inset shows the coverage vs $1/L$, which implies that in the thermodynamic limit, $L \rightarrow \infty$, 54.71% is a reasonable upper bound value. We do not only present the value of the coverage, but also the second cumulant of the distribution $P(\theta)d\theta$, i.e., the variance of the coverage. This is accomplished in Fig. 4.20(b), where the log-log plot of the variance of the coverage as a function of the system size (L^2) is shown.

We also showed that the algorithm provides for accurate time evolution towards the jammed state (see Sec. 4.4). Recall that, according to Feder's law, the approach to the jammed state in continuum RSA scales according to a power-law, eq. (4.12), where d represents the effective dimensionality of the problem [175, 177, 178]. For monodisperse particles, $d = 2$, while for polydisperse particles, $d = 3$. In fact, the approach to the

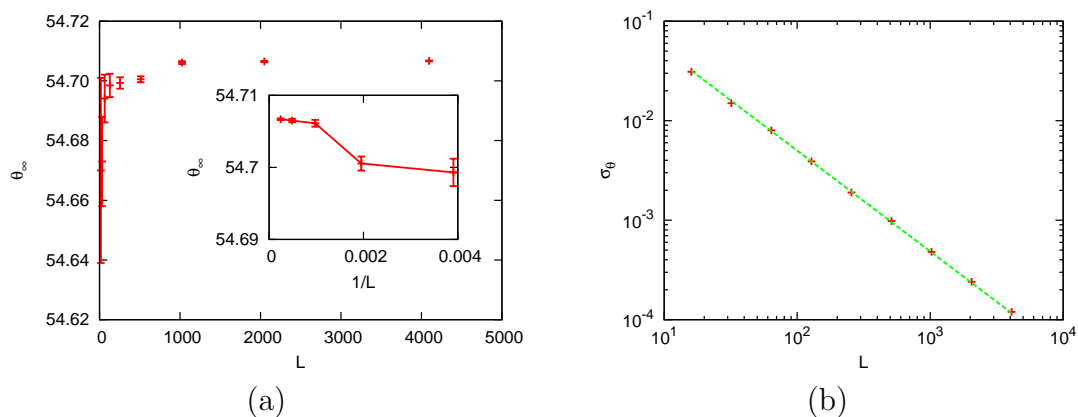


Figure 4.20: For the irreversible adsorption of monodisperse disks. (a) Coverage, θ_∞ as a function of the linear size of the system. (b) Error of the coverage as a function of the system size.

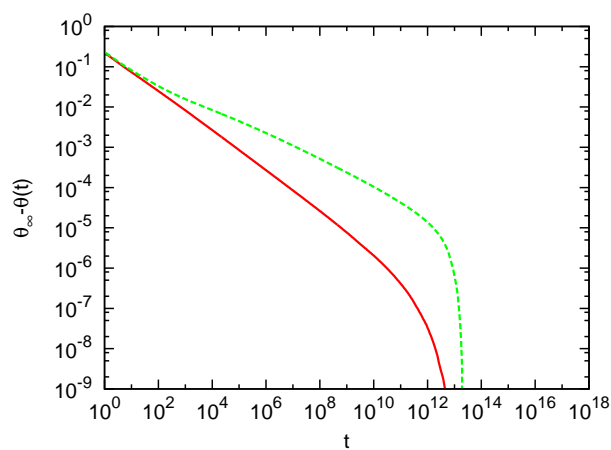


Figure 4.21: Coverage as a function of time for adsorption on clean/regular substrates. On clean substrates, adsorption of monodisperse particles for a system size of $L = 4096$ (red solid line) and truncated gaussian-size distributed particles with size dispersion of 1% and $L = 2048$ (green dashed line). Sampled over 10^3 independent runs for the monodisperse case and 10^2 samples for adsorption of particles with truncated gaussian-size distribution.

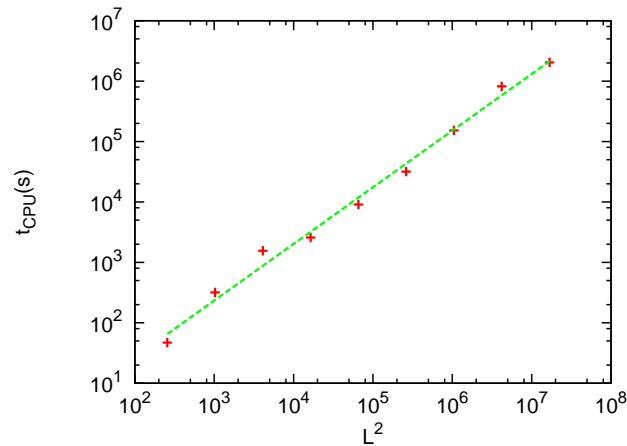


Figure 4.22: Run time as a function of substrate area for 10^3 independent runs of monodisperse particles adsorption on clean/regular substrates.

jammed state is characterized in the latter case by a crossover from $d = 2$ to $d = 3$ [224, 228] with the crossover time shifting to later time with decreasing values of the size dispersion. Consequently, on finite systems and at low size dispersions the crossover to $d = 3$ can actually not be observed. The only way is to simulate larger system sizes and be able to reach the jammed state, a feature easily achieved with the present type of algorithms [224, 235]. Figure 4.21 shows plots of the time dependence of the coverage at late times for the cases monodisperse and polydisperse particles on (clean) substrates. In specific case of the polydisperse adsorption of disks, the linear size of the systems is $L = 2048$ mean particle diameters. A truncated Gaussian size distribution is used to simulate a 1% spread around the mean value, where truncation means that values outside the interval $]r_{\min}, r_{\max}[$ with $r_{\min} = \langle r \rangle - 2\sigma$, $r_{\max} = \langle r \rangle + 2\sigma$, where σ represents the dispersion around the mean, are neglected. Such a value of the polydispersity is considered highly monodisperse in experimental terms, where size dispersions of $\lesssim 4\%$ are considered highly monodisperse. Finally, we point out that the simulation results do confirm Feder's law.

We now address more technical details as they do not contribute directly to the physics of the problem, but more into the properties of the algorithm, e.g., the CPU time depen-

dence with the linear size of the system. The CPU time dependence is shown in Fig 4.22 and in Table 4.4. Figure 4.22 shows a power-law dependence of the CPU time, t_{CPU} , with the system size, L^2 , i.e.,

$$t_{\text{CPU}} \approx L^{2\eta} \quad , \quad (4.16)$$

where³ $\eta = 0.94 \pm 0.03$.

We point out that the dependence of the t_{CPU} on the linear size of the system should also depend on, at each iteration of the mesh, the critical *free*-mesh cell number, i.e., the number of available *free*-mesh cells below which rescaling of the mesh occurs. This can be understood as follows: a large critical value of *free*-mesh cell number favors an 'early' rescaling of the system mesh, i.e., without a significant number of failed adsorption attempts, thus leading to extensive overhead on the rescaling process. On the other hand, if the critical *free*-mesh cell number is low, the number of failed adsorption attempts can become high.

Pair correlation function

As discussed above, the interparticle distribution function is an important statistical parameter to characterize the morphology of the jammed state (see Sec. 4.3.3). In Fig. 4.23 are the distribution functions for three different cases of adsorption on a regular substrate: monodisperse particles on a system with size $L = 4096$; binary mixture of particles⁴ with size ratio 2 for a system size of $L = 2048$; and truncated gaussian-size distributed particles with size dispersion of 1% for a system size of $L = 2048$. These results are in agreement with previous theoretical [236] and experimental results [176, 237, 238].

Since the present algorithm allows characterization of the jammed state, it is possible to compute the pair correlation function in more detail. Our numerical results also reproduce the logarithmic divergence expected at $r \rightarrow 1$ [177, 178]. The observation of such divergence

³The machine characteristics are Dual Intel Xeon (64-bits, 3.2 GHz, 2MB L2 Cache) with 8 GB RAM and 80 GB Sata disk.

⁴As in the previous chapter, binary mixture is a mixture of particles with two different particle sizes. An aspect ratio of two, means that the radius of the larger particle is twice the radius of the smaller one. Both particle types arrive to the surface with the same flux.

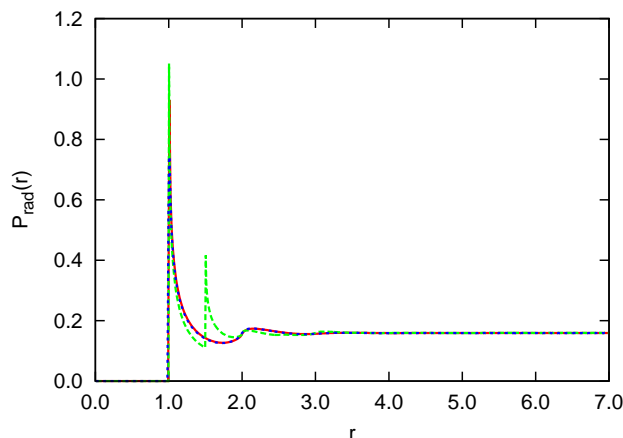


Figure 4.23: Pair correlation function of distance between particles at the jammed state for adsorption on clean/regular substrate. Adsorption of monodisperse particles on a system with size $L = 4096$ (red solid line), binary mixture of particles with size ratio 2 for a system size of $L = 2048$ (blue dashed line), and adsorption of truncated gaussian-size distributed particles with size dispersion of 1% for a system size of $L = 2048$ (green dotted line). Sampled over 10^3 independent runs to the monodisperse and binary mixture cases and 10^2 to the other system. The curves for monodisperse and truncated gaussian-size distribution are almost overlapped.

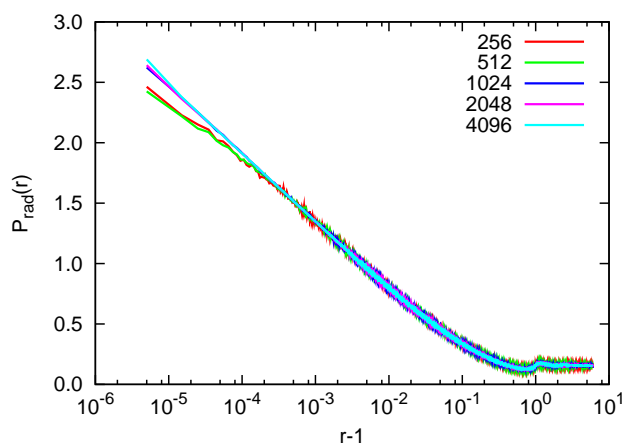


Figure 4.24: Pair correlation function of distance between particles at the jammed state for adsorption on clean/regular substrate for system sizes ranging from $L = 256$ to $L = 4096$. The logarithmic divergence at $r \rightarrow 1$ is strongly dependent on the system size. Sampled over 10^3 independent runs.

is strongly dependent on the system size, see Fig. 4.24, since the contact singularity is difficult to observe.

4.5.5 Measurement of empty area distribution

To characterize the kinetic behavior of the system is important to compute the distribution of empty area (see Sec. 4.4). A simple method is presented.

Clusters of empty mesh cells are identified with Hoshen-Kopelman algorithm [84]. For each cluster, mesh cells are iterated (divided) k_c times (only for cells of the cluster). Then, for each offspring mesh cells, single particle overlap test is performed. If a mesh cell is not completely shadow it contributes for the size of the empty area. Therefore, the size (area) is obtained with a precision of $(1/4)^{k_c} c^2$.

4.6 Conclusions

We present a study of the random sequential irreversible adsorption of particles with disk shape on patterned substrates. For simplicity we consider as a pattern equal-size cells with square shape positioned in a square-lattice matrix, such that we have one particle per vertex of a square lattice.

To characterize such pattern two parameters are used: the cell size and the cell-cell separation. Therefore, a two-dimensional diagram was presented and several adsorption regimes identified. We characterize the influence of the pattern on both the jammed-state structure and the kinetic evolution of the film. We report that by tuning the values of the pattern parameters, it is possible to control the jammed-state morphology. Specifically, it is possible to range from a completely ordered structure, revealing the order of the pattern, to an homogeneous structure qualitatively similar to the one obtained with the regular RSA model. In between, interesting, non-trivial, morphologies are observed, with local order resulting not only from the constrain of the pattern but also due to the cooperative interaction with particles previously adsorbed. Such particles can be adsorbed in the same

cell or in a neighboring one.

Through the pair correlation function we characterize the particle-to-particle correlation and systematize the influence of each parameter in the jammed-state structure. We observe that, in the presence of the pattern, the distribution is characterized by a sequence of peaks. The cell size is related with the dispersion of the peak and the cell-cell separation with the distance between peaks.

To perform such extensive Monte Carlo simulations we develop an extended version of algorithms previously proposed by Privman et al., Brosilow et al., and Wang et al. [179, 180, 225]. Specifically, the main advantage of the present one relies on the overlap rules as well as on its straightforward extension to different patterns. As discussed in Sec. 4.5, such algorithm has been applied to different study cases, not only the adsorption of monodisperse particles [128, 187, 189] but also to the adsorption of particles with truncated gaussian-size distribution [188] and a binary mixture.

The algorithmic approach is also amenable to be extended to include other geometrical or even complex particle shapes. However, in such cases overlap rules become different and have to be redefined. Besides, is also straightforward to adapt the same set of concepts to other types of patterns. The same algorithm can be applied to different system dimensions. For example, we develop the same algorithm to study the kinetic evolution of the coverage during adsorption on a line. Notwithstanding, as referred in the Chapter 3, to study the jammed-state structure, other more tailored algorithms have been developed [146].

Part III

Down to the Atomic Scale

Chapter 5

Islands nucleation and growth: submonolayer epitaxial deposition

“The individual organs follow the same pattern as the whole organism, i.e. they have their period of growth, of stationary, maximum activity and then of aging decline.”

W. Ostwald, in *Nobel Lecture (1909)*

So far, the discussion about films growth has been focused on the irreversible adsorption regime, i.e., after being adsorbed, particles cannot detach or diffuse, at least within experimental time scales. Besides, landing particles have been considered much larger than the ones from the substrate, leading to a continuum description of particles position on the substrate. However, for certain films, diffusion of particles can no longer be neglected, so the relaxation process is fundamental to understand the physical phenomena.

Understanding how relaxation affects film growth is the main goal of this chapter. The film evolution is a balance between the deposition process, that kicks the system to out-of-equilibrium conditions, and the diffusion process driving the system to equilibrium, therefore, the system is kept out of equilibrium during deposition. If the deposition of particles stop, the system relaxes towards equilibrium and, eventually, after a typical

relaxation time, the equilibrium configuration is obtained.

Example of such systems is the growth of films on crystalline substrates, e.g., the growth of Ag/Ag(100) that is addressed in this chapter. Specifically, we focus on the formation of the first layer of atoms (layer with one atom thickness). At such length scales, an atomistic description of the system is required. Thiel and Evans [239], in a recent review of the key energetic parameters of diffusion on Ag/Ag(100), refer a set of reasons to study silver. We stand out the fact of being representative for investigation of the main mechanisms in higher melting point metals like, e.g., Pt and Fe, which are more difficult to study.

Metals like silver tend to arrange on a FCC lattice [240]. Such structure is characterized by a lattice constant a_{lc} that differs from metal to metal. Consequently, the description of the growth needs to take into account if the deposited atoms (film atoms) are of the same type of the surface atoms (substrate atoms) [77, 241]. If the film atoms and the substrate ones are of the same type, the natural distance between particles is the same, both in the film and in the substrate. Therefore, a strain-free structure can grow. Such deposition regime is known as homoepitaxial¹ [243, 244, 245]. On the other side, in heteroepitaxial regime [246, 247, 248, 249], the deposited atoms and the surface ones have different typical distances (lattice constant) so, a mismatch occurs and, consequently, the film grows under strain. Besides, different interactions between particles lead also to interesting phenomena not observed within homoepitaxial growth [250, 251, 252].

Typically, the obtained films have a thickness larger than the atomic size (multilayer growth)[16, 77, 241, 247, 253]. Though, since the first layer works as a template for the multilayer growth, it is important to study the submonolayer regime [254, 255].

We start with the discussion of the diffusion process and we describe the type of models that have been developed to study islands nucleation and growth. Following, we introduce our model and characterize the submonolayer growth of Ag/Ag(100) at 200K. Specifically, we discuss the influence of the flux in the density of islands, in the mean island size, and

¹The term epitaxial was coined by L. Royer [242] and comes from the Greek, where *epi* means “on” and *taxi* means “order”.

in the island size distribution.

5.1 Surface diffusion

For films growth on crystalline substrates, two different types of processes are relevant: the deposition and the diffusion. The former consists of the flux of particles randomly and uniformly all over the substrate, while the latter one is the subject of the present section.

Atoms, after being deposited, hop on the surface between different lattice positions. Such hopping process is a thermally activated process. Due to this phenomenon of mass transport, particles nucleate and islands (cluster of atoms) are obtained. Therefore, the morphology of the film is sensitive to the surface temperature [253].

The process of mass transport is known as diffusion. Two types of diffusion coefficients can be identified [256]: collective diffusion and tracer diffusion coefficients. The collective diffusion coefficient² (D_c) describes the collective movement of matter due to concentration gradients. Specifically, the mass transport can be described by,

$$\frac{\partial N_p}{\partial t} = D_c \nabla^2 N_p \quad , \quad (5.1)$$

where N_p is the density of particles. The tracer diffusion coefficient (D), describes the mean square displacement of one isolated random walker per unit time (see Chapter 1). As discussed below, such diffusion coefficient can be studied through the island size density. At low coverage, when the interaction between film atoms can be neglected, these two diffusion coefficients become equivalent. From now on, the latter coefficient is denoted just as diffusion coefficient.

In Chapter 1, we have referred that the transition state theory (TST) can be applied to compute the hopping rate of an adatom on a periodic substrate (see eq. (1.10) and discussion therein). At that point, we have just referred the Arrhenius equation to obtain the rate of the process from the temperature, the activation barrier, and the attempt

²In the literature is also possible to find other terms like chemical or Fickian diffusion.

frequency. Though, TST can be formulated in a more general description to obtain more insight of the attempt frequency. Generically, for harmonic TST, the hopping rate between two different states is given by

$$\nu = \frac{k_B T}{h} \exp\left(-\frac{\Delta\mathcal{F}}{k_B T}\right), \quad (5.2)$$

where $\Delta\mathcal{F}$ is the difference in the Helmholtz free energy between the saddle point (transition site) and the local minimum of the potential energy surface (binding site), and h is a constant. Using the Helmholtz free energy definition [2], $\mathcal{F} = E - TS$, we separate the energy term from the entropic one, in eq. (5.2), and arrive to the Arrhenius equation (1.10),

$$\nu = \nu_0 \exp\left(-\frac{E_a}{k_B T}\right), \quad (5.3)$$

where the attempt frequency (ν_0) is given by,

$$\nu_0 = \frac{k_B T}{h} \exp\left(\frac{\Delta S}{k_B}\right). \quad (5.4)$$

To a very good approximation, attempt frequency can be considered temperature independent, since the decrease of the entropy variation with the temperature increase does counterbalance the temperature increase in the prefactor of eq. (5.4) [256]. In the present work, for the considered temperature of 200K and all possible transitions, the attempt frequency is taken temperature independent and equal to 10^{13}s^{-1} .

The Einstein relation developed for the Brownian motion on a square lattice [256], allows to relate the attempt frequency with the diffusion coefficient D by,

$$D = \frac{1}{2d} \nu, \quad (5.5)$$

where d is the dimension of the motion. The diffusion coefficient can then be obtained by,

$$D = D_0 \exp\left(-\frac{E_a}{k_B T}\right), \quad (5.6)$$

where

$$D_0 = \frac{1}{2d} \nu_0 \quad . \quad (5.7)$$

To apply TST we assume that diffusion occurs through jumps between neighboring sites and with atoms being most of the time at the binding sites. The latter assumption allow us to consider that atoms have enough time to thermally equilibrate, with the substrate, between transitions. Such consideration is fundamental to treat the system evolution as a Markov process where successive transitions are uncorrelated. Voter and Doll [257] demonstrate that TST and molecular dynamics yield similar results with considerable computational savings in the case of TST. The efficiency of TST increases with the decrease in the temperature. The lower the temperature, the greater the typical resting time at the binding sites. On that ground, for low values of temperature, the time increments between transitions are typically larger.

5.2 Definitions

Before going on with the model and the results, let us make some definitions like, e.g., the concept of island, density of islands, and mean island size.

Islands are defined as clusters with more than one atom. If s defines the number of atoms in the cluster, then an island is characterized by $s > 1$. To characterize the number of islands in the substrate, the density of islands (N_{isl}) is considered, which is defined as the number of islands per unit lattice site. For a square lattice with lateral length L (in units of lattice constants),

$$N_{isl} = \frac{\sum_{s>1} n_s}{L^2} \quad , \quad (5.8)$$

where n_s is the number of islands of size s . The density of adatoms (N_1) is, in a similar way, given by

$$N_1 = \frac{n_1}{L^2} \quad , \quad (5.9)$$

where n_1 is the number of monomers. It is also possible to define the density of islands

of size s (N_s), as

$$N_s = \frac{n_s}{L^2} . \quad (5.10)$$

Together with the density of islands, to characterize the morphology of the surface at the submonolayer regime, it is relevant to define the mean island size (s_{av}) as the average size of the islands,

$$s_{\text{av}} = \frac{\sum_{s>1} n_s s}{\sum_s n_s} . \quad (5.11)$$

The out-of-equilibrium nature of the problem is related with the balance between the flux of incoming atoms (Φ) and the diffusion of adatoms on the substrate (D). A relevant parameter is the relation between these two, so we define R_M as

$$R_M = \frac{D}{\Phi} . \quad (5.12)$$

5.3 Modeling islands nucleation and growth

As discussed in Chapter 2, physical phenomena occur at different time and length scales. Based on the problem at hands, it is important to define what are the phenomena that we want to understand and the required level of detail to study them. The analysis of the thin-film evolution and, specifically, the influence of the flux in such evolution, requires, at least, time scales of the order of the second. Moreover, to attempt a statistical description, in order to avoid statistical errors, large system sizes need to be considered. Therefore, with Molecular Dynamics, it is not possible to achieve the required time scales and system sizes. Theoretical models have been developed to analyze the island nucleation and growth and results have been obtained with rate equations and/or direct simulation [77].

In this section we describe the types of models that have been developed and, briefly, discuss the use of rate equations to study such models. We leave to a later section the use of kinetic Monte Carlo method to implement our own model.

Evans and Bartelt, in ref. [254], classify models into four different categories: *models*

with critical size s^* , models with prescribed bond scission, nearest-neighbor pair-interaction models, and classical “exact” treatments. In models with critical size s^* [255, 258, 259, 260], islands with size $s > s^*$ are, assumed, stable and never dissociate. When such type of models are studied with a rate equations formalism, substable ($s \leq s^*$) clusters are considered in quasiequilibrium (discussion below). For models with prescribed bond scission [261], two possible choices can be followed: no breaking of any (single or multiple) bonds or breaking of single, but not multiple bonds. This produces a model similar to $s^* = 2$ on a triangular lattice and $s^* = 3$ on a square lattice. Since such type of models can be mapped to the ones related with critical size, they lead to similar results. The previous two types of models are only valid for regimes where the shape of the island does not, significantly, affect the capture of particles in the neighborhood of the island. In fact, the morphology of the island can influence, e.g., the density of adatoms and island size distribution [262, 263, 264, 265]. Therefore, the study of restructuring is also relevant [266, 267, 268, 269, 270].

The other two type of models account for relaxation phenomena. In the nearest-neighbor (*NN*) pair-interaction models [271, 272], adatoms hop to empty nearest neighbor sites with an activation barrier that depends on the number of intralayer *NN* adatoms before hopping, specifically, activation energy is considered to be given by

$$E_a = E_d + nE_{\text{bond}} \quad , \quad (5.13)$$

where E_d is the activation barrier for the adatom diffusion (terrace diffusion), E_{bond} is a measurement of the strength of interaction, and n the number of nearest-neighbors before hopping. Other similar models have also been developed with n being the difference between the number of nearest-neighbors before and after the hop [266, 267, 268, 269]. In the classically “exact” treatments of surface diffusion, a “catalogue” of all possible processes [39, 97, 239] and respective rates is required. Values of activation barriers can be computed with different techniques like, e.g., embedded adatom method (EAM) or density functional theory (DFT), as discussed in Chapter 2. Typically, instead of considering all the possible

transitions, phenomenological arguments are used to select the fundamental ones. In fact, no one can guarantee that all the relevant processes are considered in the system, however, for homoepitaxial growth, the use of a predefined list of processes has been leading to satisfactory results. Notwithstanding, as discussed in Chapter 2, new methods based on accelerated Molecular Dynamics [75, 114] and kinetic Monte Carlo with dimer methods [104], are being developed to avoid a predefined, static, list of processes.

5.3.1 Rate equations

The most common analytical method to study submonolayer growth, specially nucleation problems, is the use of rate (master) equations. A set of differential equations is written and solved to describe the time evolution of the system. We follow the methodology used by Venables [273] to discuss the method. Such description is intended to put forward the limitations of this treatment and stress where the computational methods can bring more insight into the problem.

Atoms arrive to the substrate with flux Φ . Once deposited, they can diffuse, with a diffusion coefficient D , or evaporate with a rate τ_a . Due to the diffusion process, adatoms can collide with islands, with size s_i , at a rate U_i . Therefore, an ensemble of different islands sizes is obtained on the substrate.

The density of adatoms (isolated walkers), N_1 , increases due to the deposition event and decreases due to evaporation, collision between two adatoms leading to dimers, or capture of adatoms by an i -island with size s_i . Generally, the rate equation for the density of adatoms can be written as

$$\frac{dN_1}{dt} = \Phi - \frac{N_1}{\tau_a} - 2U_1 - \sum_{i>1} U_i \quad , \quad (5.14)$$

where the $2U_1$ refers to the collision between two adatoms and the $\sum_{i>1} U_i$ to the capture by i -islands of size s_i .

The rate equation for the density of islands of size s_i , N_i , is

$$\frac{dN_i}{dt} = U_{i-1} - U_i \quad (i \geq 2) \quad , \quad (5.15)$$

with a gain contribution from the capture of adatoms by islands of size s_{i-1} and a loss contribution from the capture of atoms by i -islands.

It is now necessary to find an expression for the capture of atoms by i -islands, U_i . To simplify the problem we consider two assumptions: islands with a size $s > s^*$ are stable and subcritical islands ($s \leq s^*$) are in local equilibrium with adatoms population. The former consideration means that, usually, another adatom arrives before the island decay. If we define N_x as the density of stable islands, then

$$\frac{dN_x}{dt} = \sum_{i>i^*} (U_{i-1} - U_i) = U_{i^*} \quad , \quad (5.16)$$

where all the other terms cancel in pairs. It is also possible to subtract another term related to other phenomena, like loss of islands due to coalescence. The second consideration leads to the Walton equation [273],

$$N_i = (N_1)^i \sum_m C(m) \exp\left(\frac{E_i(m)}{k_B T}\right) \quad (5.17)$$

where the sum is over all the possible configurations m for islands of size s_i and $E_i(m)$ is the binding energy of the m configuration. Such relation comes from the detailed balance of local equilibrium

$$\frac{N_i}{N_{i-1}} = N_1 C \exp\left(\frac{\Delta E}{k_B T}\right) \quad , \quad (5.18)$$

where C is a weight, which is constant for a particular size.

The rate of capture, U_i , shall include the growth term, $\sigma_i D N_1 N_{i-1}$, related to adding a single atom to an island of size s_{i-1} by diffusion of the atom, and the decay term ($i \rightarrow i-1$), $-\nu_0 N_i \exp\left(\frac{-(E_d + \Delta E)}{k_B T}\right)$, where ΔE is the difference in binding energy between islands with size i and $i-1$. The term σ_i represents the capture number of an island with size i .

The rate equation to single atoms, eq. (5.14), must simplify,

$$\frac{dN_1}{dt} = \Phi - \frac{N_1}{\tau_a} - \left(2U_1 + \sum_{i < i^*} U_i \right) - \sigma DN_1 N_x, \quad (5.19)$$

where the term $2U_1 + \sum_{i < i^*} U_i$ is almost always numerically unimportant³ and the capture of atoms by stable islands, $\sigma DN_1 N_x$, can be written as $\frac{n_1}{\tau_c}$, where τ_c is the rate of capture. Recall that τ_a is the evaporation rate.

The density of stable islands, N_x , is then

$$\frac{dN_x}{dt} = \sigma DN_1 N_x - U_C \quad (5.20)$$

where U_C is due to coalescence of islands and proportional to $N_x \frac{d\theta_{s^*}}{dt}$ (θ_{s^*} is the coverage of the substrate by stable islands) [273], and σ is the capture number related to the size, stability, and spatial distribution of islands [264].

Generally, the density of atoms, N_1 , is

$$\frac{dN_1}{dt} = \Phi - \frac{N_1}{\tau} \quad (5.21)$$

where $\tau^{-1} = \tau_a^{-1} + \tau_n^{-1} + \tau_c^{-1} + \dots$, with τ_a related with evaporation, $\tau_n^{-1} = \frac{2U_1 + \sum_{i < i^*} U_i}{N_1}$ related with capture by subcritical-size islands (almost numerical unimportant), and $\tau_c^{-1} = \sigma_x DN_x$ related with capture by stable islands.

As stated previously, island morphology, as well as the local configuration, affects the capture of adatoms. The capture number, σ_i , is not only size dependent but also spatially dependent. Yet, the rate equations method eliminate spatial fluctuations leading to uncontrolled approximations and problems are limited to simple models. Therefore, different methods need to be applied to deal with such cases. In the next section, we present a model to mimic the submonolayer growth of Ag/Ag(100) that is simulated based on the kinetic Monte Carlo method, which has been introduced in Chapter 2.

³Bartelt and Evans considered, without proof, that $s^* = 1$ to Ag/Ag(100), see e.g. [258].

5.4 Model

We intend to study the submonolayer growth of Ag/Ag(100). In the present section, we present our model to simulate such system.

An atomistic description needs to be considered. Atoms are deposited in the substrate with a given flux, Φ , and after being deposited they are able to diffuse. The energy landscape of the surface, is characterized by a set of basins denoted as binding sites. As discussed in Chapter 1, atoms stay most of the time vibrating within the basin and, eventually, due to thermally activated processes, they hop to different ones.

Ag atoms are deposited randomly on the substrate with equal probability for all lattice sites. Since the Ehrlich-Schwoebel barrier is very low for Ag(100), when a deposited particle lands on top of an occupied site it diffuses, in a random walk, to an empty one. It is due to such low value of the barrier that Ag/Ag(100) is known to grow in a layer-by-layer way (Frank-van der Merwe mode of growth). Besides, it is also reasonable to assume that, in the considered time scale, silver atoms are not able to detach from the substrate [77].

Silver, as other metals, tend to order in a FCC crystal [240]. So, when it is cut in the (100) crystal orientation, it has the atoms organized on a square lattice. Therefore, a square lattice is considered. We decouple the atoms vibration (within the basin) and the atoms diffusion (hops between basins) and, instead of attempting a detailed description of the vibration, we only account for the thermal fluctuations of the kinetic energy. As explained in the context of eq. (5.3), based on the activation barrier, it is possible to compute the frequency of each considered process in the system.

Build up the list of relevant processes is a far-from-easy task. Different techniques to “catalogue” such processes were already discussed in Sec. 5.3. Keeping in mind the main goal of computing the activation barriers, and consequently the rate of each process, and since such barriers are dependent on the local configuration, we consider the cell of 12 lattice sites schematized in Fig. 5.1. Note that, a given adatom on a square lattice, can move to, up-to, four different neighbors, meaning that the periodicity of the lattice

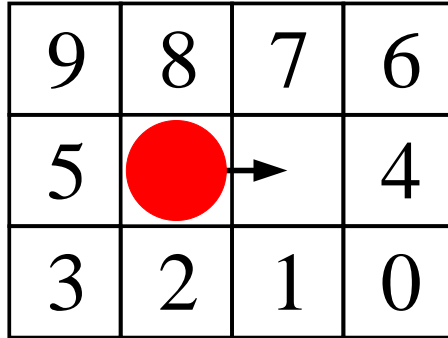


Figure 5.1: Basic cell of 12 lattice sites. The central sites are the initial and final position and the numerated ones are their first and second neighbors.

is characterized by a $\pi/2$ rotation symmetry. The two central lattice sites represent the initial and final position of a given hop. For all considered processes, the initial position needs to be occupied and the final one empty. On that ground, only the states of the 10 lattice sites change from process to process.

If such set of 10 lattice sites is considered, and since each one can be occupied or empty (two possible states), with a naive (without symmetry operations) construction of the list, $2^{10} = 1024$ processes are obtained. In fact, symmetry operations can be applied to reduce the number of processes in the list. For example, consider two different configurations A and B . Each one characterized by its 10 lattice-site states. If $A_4 = B_4$ and $A_5 = B_5$, where the index is related with the site number in Fig. 5.1, then an obvious symmetry occurs, as far as $A_{0,1,2,3} = B_{6,7,8,9}$ and $A_{6,7,8,9} = B_{0,1,2,3}$. Accordingly, the list is reduced to 544 possible processes, without any approximation.

Another important data is the activation energy for each process. To the best of our knowledge, the most complete database of processes and respective activation barriers, for Ag/Ag(100), have been reported by Voter [39], in 1987. The considered interatomic potential is similar to the embedded atom method (EAM) previously presented by Daw and Baskes [274]. We just summarize here the main features of the potential. For further reading see, e.g., [39, 274]. Since in metals the atom core is “embedded” in a electron fluid, in the embedded atom method, the potential energy is written as a sum of the pairwise

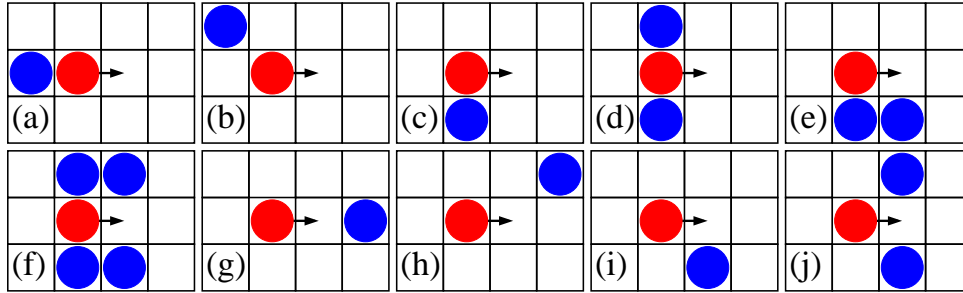


Figure 5.2: Fundamental processes for Ag/Ag(100). All processes that can take place in the surface are superpositions of these fundamental processes with the terrace diffusion. (a) initial bond break, (b) initial second neighbor (can be one or two), (c) first initial slide neighbor, (d) second initial slide neighbor, (e) first edge neighbor, (f) second edge neighbor, (g) final bond formation, (h) final second neighbor, (i) first final slide neighbor, and (j) second final slide neighbor.

interaction between atoms, ϕ , and an embedding function F_e which accounts for the effect of the electron density, ρ_e . Specifically,

$$H = \frac{1}{2} \sum_i \left(\sum_{j \neq i} \phi(r_{ij}) + F_e[\rho_e(r_i)] \right), \quad (5.22)$$

where the used parameters for silver are discussed in the original paper [39].

We consider that each process can be taken as the superposition of the terrace diffusion and a combination of up-to ten other processes, namely: initial bond break, initial second neighbor (can be one or two), first initial slide neighbor, second initial slide neighbor, first edge neighbor, second edge neighbor, final bond formation, final second neighbor (existence or not⁴), first final slide neighbor, and second final slide neighbor. All processes are schematized in Fig. 5.2. Based on such set of fundamental processes, the total list of possible transitions shrinks to 241 processes.

To construct the list of the 241 processes referred above it is important to take into account that certain fundamental processes cannot occur simultaneously, i.e., if a given fundamental process is present the other one cannot be. We list some examples. When a first

⁴The effect of having one or two final second neighbors is the same.

edge neighbor (Fig. 5.2(e)) exists, there are no first initial slide neighbor (Fig. 5.2(c)) and first final slide neighbor (Fig. 5.2(i)). If there is a second edge neighbor (Fig. 5.2(f)), there is also a first edge neighbor (Fig. 5.2(e)) but no: first initial slide neighbor (Fig. 5.2(c)), second initial slide neighbor (Fig. 5.2(d)), first final slide neighbor (Fig. 5.2(i)), second final slide neighbor (Fig. 5.2(j)). A first initial slide neighbor (Fig. 5.2(c)) is incompatible with a second final slide neighbor (Fig. 5.2(j)) or a first final slide neighbor (Fig. 5.2(i)) in the same side. A second initial slide neighbor (Fig. 5.2(d)) occurs with a first initial slide neighbor (Fig. 5.2(c)), but it is incompatible with a first and a second final slide neighbor (Fig. 5.2(i) and (j)). In the same way, if there is a first final slide neighbor (Fig. 5.2(i)) there is no second initial slide neighbor (Fig. 5.2(d)).

From the results of ref. [39], we compute how each fundamental process affects the activation energy of a process. The results are summarized in Table 5.1. For each one, the activation barrier (E_a) can be computed as,

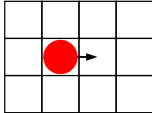
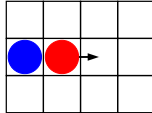
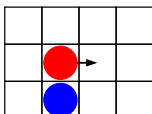
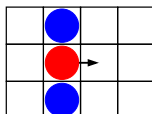
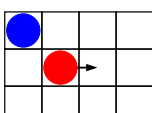
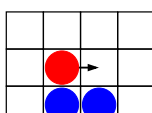
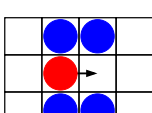
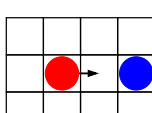
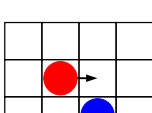
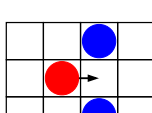
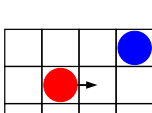
$$E_a = E_d + \sum_j \Delta E_j \quad , \quad (5.23)$$

where E_d is the activation energy of the terrace diffusion and the sum is over the fundamental processes.

The model has been implemented with the kinetic Monte Carlo method⁵. During the simulation, a “dynamical hierarchy” of transition probabilities is adopted, based on the energy barrier of each process, according to eq. (5.3). At each iteration, a process occurs, based on the transition probabilities, and time is incremented in agreement with eq. (2.15). The obtained results, with the model described above, are discussed in the next section.

⁵See Sec. 2.1.2 for discussion about the method.

Table 5.1: The table summarize the contributions (ΔE) of each fundamental process to the activation barrier, eq. (5.23). Values computed from different processes cataloged by Voter [39].

	+0.486 eV		+0.279 eV
	+0.013 eV		+0.133 eV
	+0.051 eV		-0.280 eV
	-0.027 eV		-0.030 eV
	-0.250 eV		-0.027 eV
	+0.007 eV		

5.5 Results

Atoms are deposited on the crystalline substrate and, after being deposited, they jump from binding site to binding site. The hopping process between different sites is a thermally activated process, therefore the diffusion coefficient increases with the temperature. The higher the temperature, the larger the transition rate. At the same time, to minimize the total free energy of the system, atoms tend to aggregate leading to clusters (islands). On that ground, studying the fundamental mechanism related with the nucleation process as well as the influence of the controlled parameters, like flux and the temperature, are important to predict how to tune the morphology of the film through the control of the deposition conditions.

Research efforts have been focused on the statistical analysis of islands formation. We present our own results obtained for the island density, mean size, and distribution, defined in the Sec. 5.2, through simulation of the homoepitaxial deposition of Ag/Ag(100) at a temperature of 200K. Specifically, for different values of the flux of incoming particles, ranging from $10^{-3} - 10^0$ ML/s, we study the system evolution for values of coverage below 20%. For each simulated case, results were averaged over five different samples. In Fig. 5.3(a)-(d) are snapshots of the system for different values of the flux. It is clear that the flux of particles affects, not only, the density of islands, but also their size distribution. We focus our study in three different parameters: island density, average island size, and island size distribution.

As atoms are deposited, they diffuse and eventually nucleate. At an earlier stage of the deposition process, the density of islands is expected to rise due to the nucleation of new islands. The system is mainly made-up of adatoms that diffuse randomly and nucleate leading to dimers. This regime is denoted as the *nucleation regime*. As the number of islands increases, the probability of an adatom collision with an existent island also increases so, mainly, islands growth is observed instead of nucleation. This regime is known as the *growth regime*. Eventually, the size of the islands is such, that islands start to coalesce (*coalescence regime*). The density of islands will then decrease and the size of

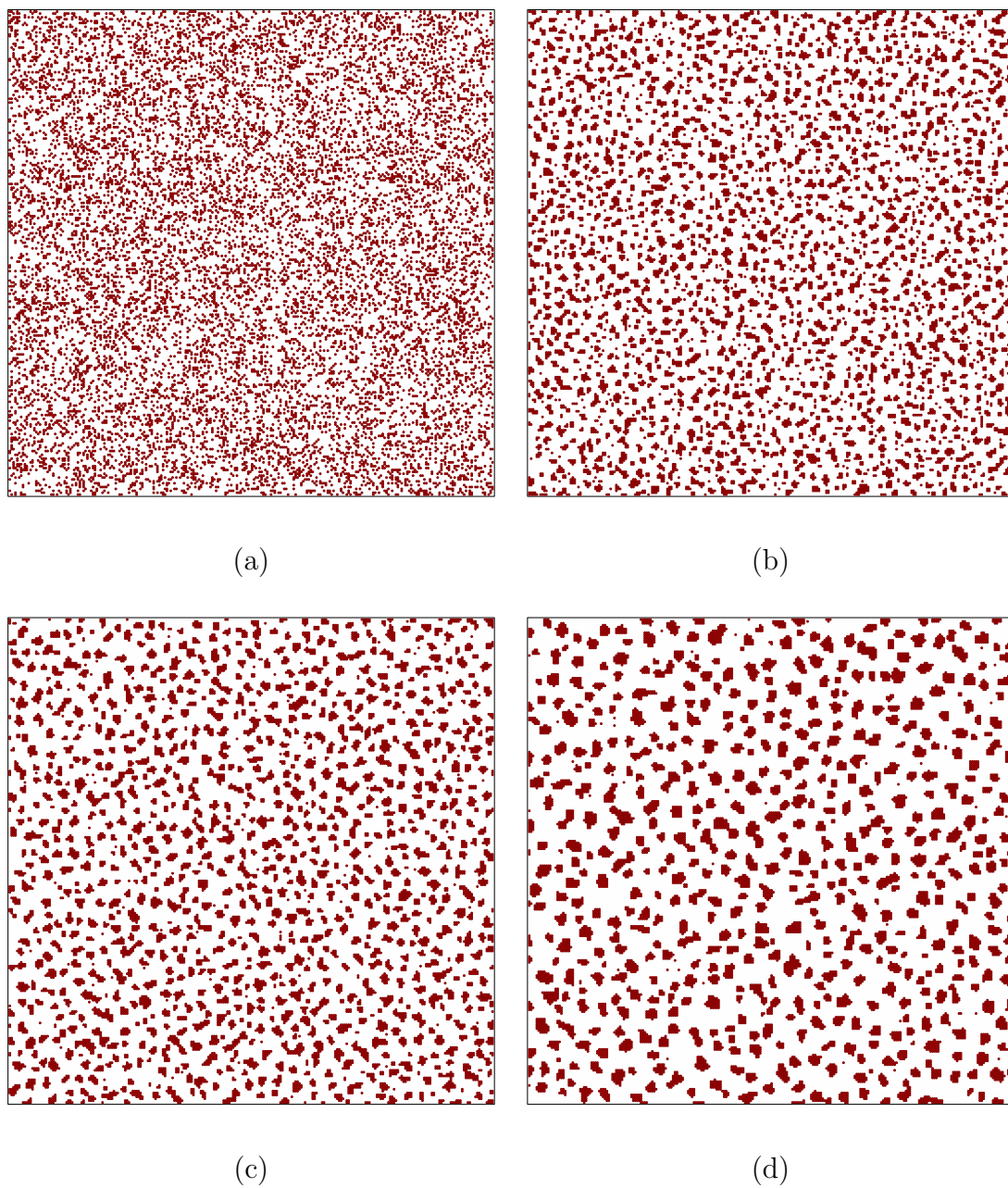


Figure 5.3: Snapshots of a system with 256×256 lattice sites for a coverage of 20%, under different fluxes of incoming atoms: (a) 10^0 ML/s, (b) 10^{-1} ML/s, (c) 10^{-2} ML/s, and (d) 10^{-3} ML/s.

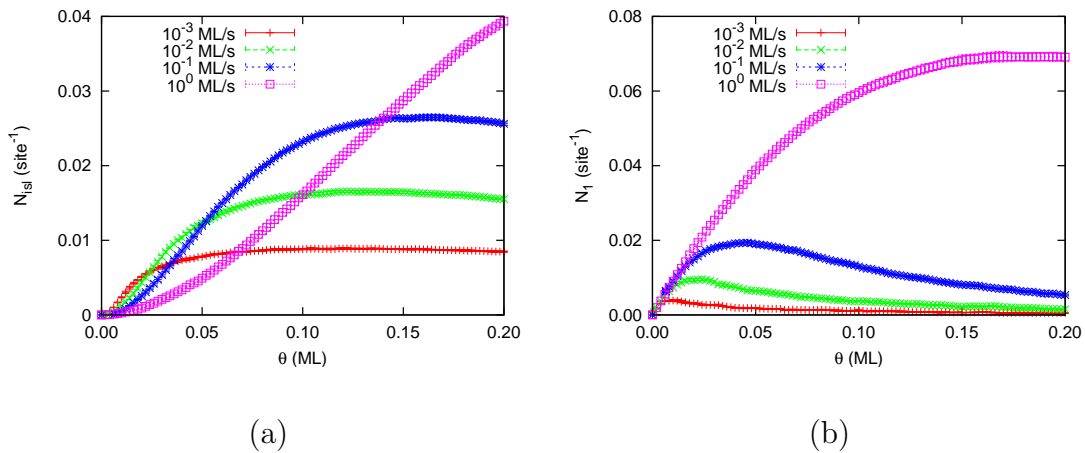


Figure 5.4: For different values of the flux: (a) Density of islands (N_{isl}) as a function of the coverage (θ). (b) Density of monomers (N_1) as a function of the coverage (θ). System size of 256×256 lattice sites and results averaged over five samples. Error bars included for each data point.

the islands will augment. In the limit of 100% coverage, a single layer is obtained with a single island of the size of the system.

In Fig. 5.4, we plot the density of islands (N_{isl}), Fig.5.4(a), and the density of monomers (N_1), Fig.5.4(b), as a function of the coverage for four different fluxes, namely, 10^{-3} , 10^{-2} , 10^{-1} , and 10^0 ML/s. We only consider values of coverage below 20%. It is possible to observe the first two regimes referred above. As the value of the flux increases, the crossover between the *nucleation regime* and the *growth regime* occurs for greater values of coverage. The density of monomers, Fig. 5.4(b), is characterized by a maximum value. Initially an, almost linear, increase of N_1 with the coverage is observed but, when the rate of capture by islands becomes relevant, such behavior smooths out and eventually it starts to decrease.

In Fig. 5.5, is the average island size (s_{av}) as a function of the coverage. In the island *nucleation regime*, the mean island size does not change significantly with the coverage, but in the *growth regime* it augments. From Figs. 5.4 and 5.5, it is also evident that the transition from the first to the second regime occurs for different values of coverage depending on the value of the flux. Greater the flux, later (in terms of coverage) the

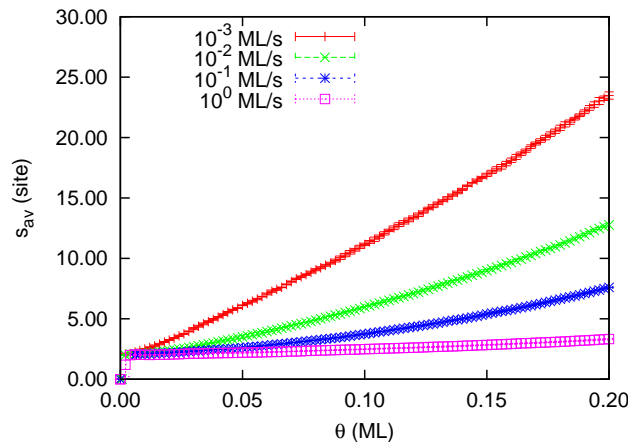


Figure 5.5: Average island size (s_{av}) as a function of the coverage (θ). System size of 256×256 lattice sites and results averaged over five samples. Error bars included for each data point.

transition, i.e., high values of flux extends the *nucleation regime* and leads to a greater island density (number of islands) but smaller ones.

According to *mean field* studies [77, 256], for models of islands with critical size s^* , the island density (N_{isl}) is expected to scale according to a power law

$$N_{isl} \sim \left(\frac{D}{\Phi} \right)^{-\chi} = R_M^{-\chi} . \quad (5.24)$$

For the asymptotic limit of the *growth regime*, when models of critical size s^* are considered, the exponent χ is

$$\chi = \frac{s^*}{s^* + 2} . \quad (5.25)$$

Computational results for such model corroborate the predicted results [255, 258]. Mo et al. [243] present an investigation of the surface self-diffusion of Si adatoms on Si(001), using a method based on the STM analysis of the number of stable islands formed during submonolayer deposition. They did observe that, for temperatures ranging from 348 K to 653 K, the density of islands decreases with temperature and, for temperatures higher than 573 K, the density of islands drops, due to island coarsening. The power-law dependence

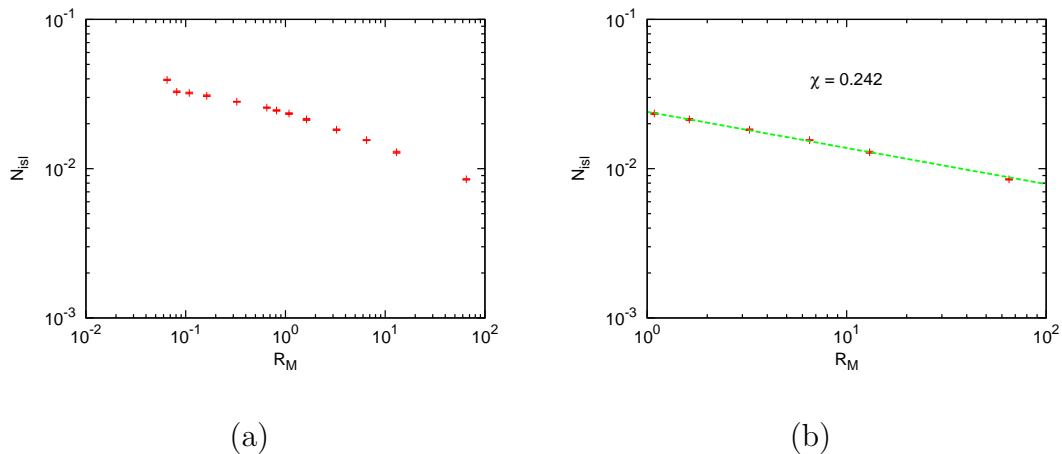


Figure 5.6: Density of islands as a function of the parameter $R_M = \frac{D}{\Phi}$. (a) For values of R_M ranging from 10^{-1} to 10^2 . (b) For higher values of R_M . System size of 256×256 lattice sites and results averaged over five samples. Error bars included for each data point.

was also experimentally observed for Fe/Fe(100) by Stroscio and co-workers [244, 245]. Monte Carlo results by Ratsch et al. [275] show that the power law holds even when detachment from island edges is considered but, in that case, the exponent is dependent on the interaction energy between particles.

Brune et al. [248, 256] report that the exponent predicted by eq. (5.25), are only experimentally observed for $R_M \gg 10^5$. Their results have been obtained for the Ag/Pt(111). For values of R_M below this value, the power-law behavior changes. Eventually, for values of $R_M < 1$ the density of islands is almost independent of R_M . In Fig. 5.6(a), we plot the density of islands as a function of R_M , for values R_M ranging from 10^{-1} to 10^2 . Despite being a different material, we observe the same qualitative behavior of the one observed by Brune and co-workers [248]. For $R > 1$, a power-law behavior is observed as evident in Fig. 5.6(b), with an exponent $\chi = 0.242 \pm 0.005$. For lower values of R_M , the density of islands becomes almost independent of the parameter R_M . As R_M decreases, due to the flux increase, the time between deposition events is such that adatoms have no enough time to diffuse and nucleate. The number of islands rises with the coverage and the island average size does not change significantly, see Figs. 5.4 and 5.5.

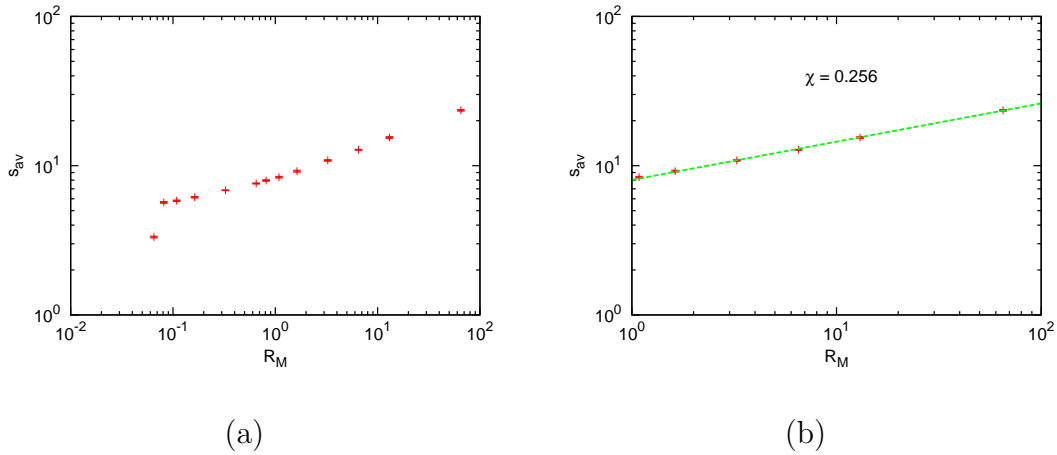


Figure 5.7: Average island size as a function of the parameter $R_M = \frac{D}{\Phi}$. (a) For values of R_M ranging from 10^{-1} to 10^2 . (b) For higher values of R_M . System size of 256×256 lattice sites and results averaged over five samples. Error bars included for each data point.

Experimental results by Zhang et al. [276] report a power-law relation between the average island size and the parameter R_M , with the same exponent χ ,

$$s_{av} = R_M^\chi . \quad (5.26)$$

The results have been obtained for Ag/Ag(100) at a temperature of 295K. They also report a decrease of s_{av} with temperature. Some theoretical results report the same relation [77, 263]. In Fig. 5.7 are the results obtained with our model. The behavior of the average island size is similar to the one from the density of islands. In the regime of $R_M > 1$, see Fig. 5.7(b), the obtained exponent is $\chi = 0.256 \pm 0.003$.

In 1984, Tamás Vicsek and Fereydoon Family [277], have studied the cluster growth of diffusion-limited aggregation of clusters in two dimensions. They report that, the cluster size distribution should obey a scaling law. According to these results [77, 256, 258, 259, 261, 278], for a given coverage θ , the island-size distribution $N_s(\theta)$ can be written in the scaling form

$$N_s(\theta) = \theta s_{av}^{-2} f_s^* \left(\frac{s}{s_{av}} \right) , \quad (5.27)$$

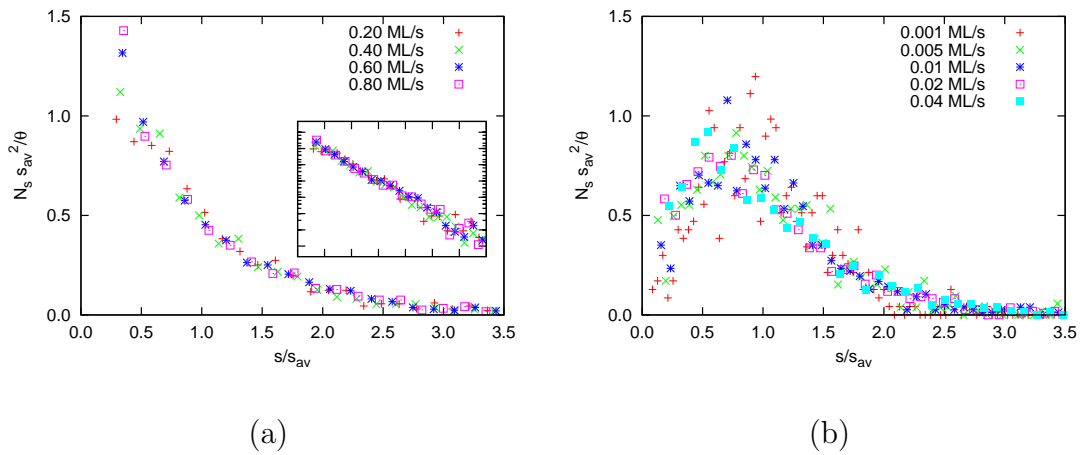


Figure 5.8: Island size distribution for different values of flux obtained for a coverage of 20%. (a) For high values of flux. (b) For low values of flux. System size of 256×256 lattice sites and results averaged over five samples.

where $f_{s^*} \left(\frac{s}{s_{av}} \right)$ is a scaling function normalized, with mean value 1, and the index s^* stands for the functional dependence on the critical island size [261].

Results obtained through different methods (analytical, computational, and experimental) [77, 244, 245, 256, 258, 259, 260, 261, 275, 279], show that such scaling function, for $s^* \geq 1$, is characterized by a maximum value near 1, and, for $s^* = 0$, the island size distribution decays monotonically with size [256, 261].

In Fig. 5.8 are the island size distributions for different values of the flux. We divided the results into two different groups. At high fluxes, Fig. 5.8(a), we recover the expected scaling function for $s^* = 0$, meaning that adatoms have no enough time to diffuse significantly and, therefore, can be considered frozen (without mobility). Islands grow mainly due to particles that are deposited at the edge of an existing one. At low fluxes, Fig. 5.8(b), the diffusion of adatoms can no longer be neglected. Between deposition events, monomers have enough time to diffuse and, eventually, either nucleate or aggregate to an existing island. At the same time, larger islands have lower mobility [280, 281]. Consequently, the island size distribution is characterized by a maximum at a size near the average size. As time evolves, under deposition, the average size increases

as well as the most probable island size.

5.6 Conclusions

The present chapter is focused on the effect of diffusion in the morphology of a film. Specifically, we studied the nucleation and growth of islands, in the submonolayer regime, of Ag/Ag(100) deposition.

Atoms of silver are deposited on a crystalline substrate and, once on the surface, they vibrate within an energetic basin and thermalize with the substrate. Eventually, due to thermal fluctuations, the adatom acquires enough energy to cross an activation barrier, in the energy landscape, and jump to a different basin. The balance between the typical deposition time and the diffusion time is the main parameter to take into account to understand the film morphology.

We are proposing a model, where processes are identified by considering the cell of 12 lattice sites. Each process is written as a combination of up-to 10 processes with terrace diffusion. Therefore, the activation energy, and respective transition rate, for each process can be computed in a straightforward manner. The model have been implemented with the kinetic Monte Carlo method. We simulate the effect of the flux on the morphology of a film resulting from silver deposition on Ag(100) substrate at a temperature of 200K.

Our results show that deposition evolves in two different regimes: *nucleation regime* and *growth regime*. In the former one, the main event is the nucleation of adatoms leading to new islands. The density of islands increases in time and the mean island size does not change significantly. In the latter regime, the density of islands is such that adatoms collide with pre-existing islands. The average size of islands increases with the number of deposited atoms and the density of islands is characterized by a plateau.

We also compute the island size distribution for 20% of coverage. For low values of flux, island size distribution obeys the scaling law predicted in the literature for critical island sizes greater than zero ($s^* > 0$). For high values of flux, the island size distribution

is the characteristic one for systems with $s^* = 0$. Since time interval between depositions is short when compared with the typical time for hopping, adatoms can be considered motionless and islands nucleation occurs, mainly, due to the deposition of particles in the neighborhood of an existing one.

A static list of possible processes is considered. In fact, as previously referred, recent techniques have been developed to avoid such consideration. Notwithstanding, models with a predefined list of processes have been used successfully, specially in the case of homoepitaxial growth, where relevant transitions only involve a single atom jump to a first neighboring site, as considered by our model. Such models have been able to reproduce results obtained with theoretical and experimental methods. On the other hand, methods where the list is built on-the-fly (or is unnecessary) are more tailored for heteroepitaxial growth, where concerted moves, involving more than one adatom, have been reported.

This work emphasis the model and its validation. As a follow-up, the model can be applied to study other system properties. Since processes are treated in a way that relaxation phenomena are considered, it is tailored to study properties related with the morphology/shape of the islands and the effect of the local configuration in the island growth.

Final Remarks

In the present work, the growth of films, under far-from-equilibrium conditions, is studied using statistical physics methods. We have developed stochastic models to characterize how phenomena can emerge from the collective behavior of particles during the adsorption and (separately) the growth process.

Under equilibrium growth conditions, the obtained structures are the ones with lowest free energy, denoted as thermodynamic equilibrium structures. However, in Nature, this is more an exception rather than the rule. Systems evolve in a way that thermodynamic structures cannot be achieved. Mechanisms, like add particles to the system and relaxation, compete leading to kinetically trapped structures.

Studied cases have been split in two different parts. A first one (Part II) where adsorption phenomena have been addressed, in the limit where particles (either segments or disks) stick irreversibly to the substrate, i.e., they cannot detach or diffuse after adsorption. A second one (Part III) where the effect of relaxation is considered, in the homoepitaxial growth of a silver film on a crystalline substrate.

In Part II we have addressed two different problems: the competitive adsorption of a binary mixture of segments on a line (Chapter 3) and the effect of a pattern on the adsorption of particles on a substrate (Chapter 4). In the former case, we take as a binary mixture, segments with two different sizes, which is characterized by its size ratio. In the limit of equal flux of both segment types, we have characterized the size distribution of the gaps between segments. Specifically, we have computed the cumulants up-to the fourth order of the distance between segments.

A distribution function for the distance between segments have been also proposed and parametrized with the first moment of the distance obtained through simulation. The cumulants of the distance have been computed with the proposed function. We found agreement between the Monte Carlo results and the ones for the proposed function. In this work, we put forward a novel method to characterize the morphology of the film using the higher-order cumulants. Despite apparently simple, the 1D version of the model grasp interesting phenomena, bringing not only more insight to the analysis at higher dimensions, but also to intrinsically one-dimensional problems like, e.g., the adsorption of polymeric chains. The considered process accounts for no other type of interactions between segments but the excluded volume and, notwithstanding, it represents a prototype for further studies of more complex systems where, e.g., soft segments are considered or particles shrink/expand once adsorbed [137, 147, 282].

For the adsorption on a surface, we studied the random sequential adsorption of particles, of disk shape, on a patterned substrate. As a pattern we considered, well defined regions, of square shape, organized in a square lattice matrix. Landing particles, solely interacting through excluded volume, can only adsorb inside those regions (cells). Changing the pattern parameters (size and distribution), it is possible to tune the morphology of the film, ranging from completely ordered (revealing the order of the pattern) to homogeneous adsorption (no long-range order). However, interesting morphologies, emerge in between where local order is observed, with a correlation length larger than the cell size. Under the constraint of the pattern, a transition in the functional dependence of the coverage kinetic approach to the jamming limit is identified. For the considered pattern we are able to pin down the set of pattern parameters where the transition occurs. Moreover, due to the stochastic nature of the random sequential adsorption process, an algorithm to fully attain the jammed state is itself a challenge. We proposed an efficient algorithm to attain full coverage, which can be straightforwardly applied to other problems like, e.g., adsorption of particles with size dispersion [188].

In this study, we neglected interactions such as electrostatic interactions, capillary

forces, and interaction between particles and the pattern-cell edges. Focus have been on the geometrical properties of the pattern constraint. Further work can address such more complex interactions. Besides, though the obtained results/conclusions can be extended to other cell shapes and distributions, different interesting properties can also emerge from such cases. For example, the effect of a pattern distributed randomly on the substrate, can pose a relevant case for the use of self-organized structures as a template for adsorption, which avoids the use of lithographic methods to produce the pattern.

In Part III (Chapter 5), the effect of diffusion is considered. Specifically, we developed a model, and used the kinetic Monte Carlo method, to study the homoepitaxial growth of Ag/Ag(100). We used an atomistic description to characterize the morphology of the film and its dependence on the ratio of the diffusion coefficient and flux of incoming particles. This work have been mainly devoted to the validation of a model as well as to the identification of its strengths and weaknesses. We report that, the model, allows reproduction of previous results and achieve experimental time scales. More insight into the system can be obtained with the model specially regarding the island shape and the effect of the local environment like, e.g., distribution of islands in the neighborhood. Since relaxation mechanisms have been included, it is tailored to study restructuring and coalescence of islands, which cannot be done with most previously presented models as the ones based on point-like islands, critical island size, or nearest-neighbor pair-wise interaction. A static list of processes has been considered, thus, it is not possible to guarantee that such model accounts for all relevant processes but, for homoepitaxial growth, such type of models has been yielding satisfactory results. Besides, our results are in agreement with previously reported ones.

Bibliography

- [1] I. Prigogine, *The end of Certainty: Time, Chaos, and the New Laws of Nature*. United States of America: The Free Press, 1997.
- [2] F. Reif, *Fundamentals of statistical and thermal physics*. United States of America: McGraw-Hill, 1965.
- [3] B. Mahon, *The Man Who Changed Everything. The Life of James Clerk Maxwell*. United States of America: John Wiley & Sons, 2003.
- [4] J. W. Gibbs, *Elementary Principles in Statistical Mechanics*. United States of America: Scribner's Son, 1902.
- [5] C. Cercignani, *Ludwig Boltzmann, The Man Who Trusted Atoms*. United Kingdom: Oxford University Press, 1998.
- [6] A. Pais, *Subtil is the Lord... The Science and the Life of Albert Einstein*. United Kingdom: Oxford University Press, 1982.
- [7] W. Ebeling and I. M. Sokolov, *Statistical thermodynamics and stochastic theory of nonequilibrium systems*. Singapore: World Scientific, 2005.
- [8] K. K. Darrow, "Statistical theories of matter, radiation and electricity," *Rev. Mod. Phys.*, vol. 1, p. 90, 1929.
- [9] L. Onsager, "Reciprocal relations in irreversible processes. II.," *Phys. Rev.*, vol. 38, p. 2265, 1931.

-
- [10] L. Onsager, "Reciprocal relations in irreversible processes. I.," *Phys. Rev.*, vol. 37, p. 405, 1931.
- [11] L. Sklar, *Physics and Chance. Philosophical issues in the foundations of statistical mechanics*. United Kingdom: Cambridge University Press, 1993.
- [12] P. Bak, *How nature works? The science of self-organized criticality*. United States of America: Springer-Verlag New York, 1996.
- [13] P. L. Garrido and J. Marro, eds., *Modeling of Complex Systems*. United States of America: American Institute of Physics, 2003.
- [14] D. Stauffer, "Introduction to statistical physics outside physics," *Physica A*, vol. 336, p. 1, 2004.
- [15] S. N. Dorogovtsev, A. V. Goltsev, and J. F. F. Mendes, "Critical phenomena in complex networks," *Rev. Mod. Phys.*, vol. 80, p. 1275, 2008.
- [16] A.-L. Barabási and H. Stanley, *Fractal Concepts in Surface Growth*. Cambridge, United Kingdom: Cambridge University Press, 1995.
- [17] H. E. Stanley, V. Afanasyev, L. A. N. Amaral, S. V. Buldyrev, A. L. Goldberger, S. Havlin, H. Leschhorn, P. Maass, R. N. Mantegna, C.-K. Peng, P. A. Prince, M. A. Salinger, M. H. R. Stanley, and G. M. Viswanathan, "Anomalous fluctuations in the dynamics of complex systems: from DNA and physiology to econophysics," *Physica A*, vol. 224, p. 302, 1996.
- [18] P. L. Garrido, J. Marro, and J. J. Torres, eds., *Cooperative Behavior in Neural Systems*. United States of America: American Institute of Physics, 2007.
- [19] D. Helbing, "Traffic and related self-driven many-particles systems," *Rev. Mod. Phys.*, vol. 73, p. 1067, 2001.

-
- [20] P. L. Garrido, J. Marro, and M. A. Muñoz, eds., *Modeling Cooperative Behavior in the Social Sciences*. United States of America: American Institute of Physics, 2005.
- [21] C. Castellano, S. Fortunato, and V. Loreto, “Statistical physics of social dynamics,” *Rev. Mod. Phys.*, vol. 81, p. 591, 2009.
- [22] R. M. Mantegna and H. E. Stanley, *An introduction to Econophysics, Correlations and Complexity in finance*. United Kingdom: Cambridge University Press, 2000.
- [23] J. Feigenbaum, “Financial physics,” *Rep. Prog. Phys.*, vol. 66, p. 1611, 2003.
- [24] D. Rickles, “Econophysics for philosophers,” *Stud. Hist. Philos. Mod. Phys.*, vol. 38, p. 948, 2007.
- [25] V. M. Yakovenko, “Econophysics, statistical mechanics approach to,” *Encyclopedia of Complexity and System Science*, ed. by R. A. Meyers, Springer, 2009.
- [26] L. D. Landau and E. M. Lifshitz, *Course of Theoretical Physics, volume 5, Statistical Physics - Part I, 3rd Edition*. United Kingdom: Elsevier, 1980.
- [27] H. Goldstein, C. Poole, and J. Safko, *Classical Mechanics, 3rd edition*. United States of America: Addison Wesley, 2002.
- [28] A. I. Khinchin, *Mathematical Foundations of Statistical Mechanics*. United States of America: Dover Publications, 1949.
- [29] L. E. Reichl, *A modern course in statistical physics*. United States of America: John Wiley & Sons, 1998.
- [30] E. J. S. Lage, *Física Estatística*. Portugal: Fundação Calouste Gulbenkian, 1995.
- [31] I. Prigogine, *Is Future Given?* Singapore: World Scientific, 2003.
- [32] G. Ódor, “Universality classes in nonequilibrium lattice systems,” *Rev. Mod. Phys.*, vol. 76, p. 663, 2004.

-
- [33] H. Hinrichsen, “Non-equilibrium critical phenomena and phase transitions into adsorbing states,” *Adv. Phys.*, vol. 49, p. 815, 2000.
- [34] R. C. Tolman, *The principles of Statistical Mechanics*. United States of America: Dover Publications, 1979.
- [35] A. Messiah, *Quantum Mechanics*. United States of America: Dover Publications, 1999.
- [36] N. G. van Kampen, *Stochastic Processes in Physics and Chemistry*. Amsterdam, The Netherlands: Elsevier Science Publishers, 1992.
- [37] O. Penrose, “Foundations of statistical mechanics,” *Rep. Prog. Phys.*, vol. 42, p. 1937, 1979.
- [38] H. S. Wio, *An Introduction to Stochastic Processes and Nonequilibrium Statistical Physics*. Singapore: World Science Publishing, 1994.
- [39] A. F. Voter, “Simulation of the layer-growth dynamics in silver films: Dynamics of adatom and vacancy clusters on Ag(100),” *SPIE*, vol. 821, p. 214, 1987.
- [40] C. L. Liu, J. M. Cohen, J. B. Adams, and A. F. Voter, “EAM study of surface self-diffusion of single adatoms of fcc metals Ni, Cu, Al, Ag, Au, Pd, and Pt,” *Surf. Sci.*, vol. 253, p. 334, 1991.
- [41] S. Chandrasekhar, “Stochastic problems in physics and astronomy,” *Rev. Mod. Phys.*, vol. 15, p. 1, 1943.
- [42] R. Stinchcombe, “Stochastic non-equilibrium systems,” *Adv. Phys.*, vol. 50, p. 431, 2001.
- [43] A. Einstein, “A new determination of molecular dimensions,” *Annalen der Physik*, vol. 19, p. 289, 1906.

-
- [44] R. Zwanzig, *Nonequilibrium statistical mechanics*. United Kingdom: Oxford University Press, 2001.
- [45] V. Privman, "Universality," *Encyclopedia of Applied Physics*, vol. 23, p. 31, 1998.
- [46] J. M. Yeomans, *Statistical Mechanics of Phase Transitions*. United Kingdom: Oxford University Press, 1992.
- [47] Z. H. Barber, ed., *Introduction to Materials Modelling*. United Kingdom: Maney Publishing, 2005.
- [48] W. Krauth, *Statistical Mechanics: Algorithms and Computations*. United Kingdom: Oxford University Press, 2006.
- [49] H. Gould, F. Family, and H. E. Stanley, "Kinetics of formation of randomly branched aggregates: A renormalization-group approach," *Phys. Rev. Lett.*, vol. 50, p. 686, 1983.
- [50] T. A. Witten and L. M. Sander, "Diffusion-limited aggregation, a kinetic critical phenomena," *Phys. Rev. Lett.*, vol. 47, p. 1400, 1981.
- [51] M. Kolb, R. Botet, and R. Jullien, "Scaling of kinetically growing clusters," *Phys. Rev. Lett.*, vol. 51, p. 1123, 1983.
- [52] H. E. Stanley and N. Ostrowsky, *On growth and form. Fractal and non-fractal patterns in physics*. The Netherlands: Martinus Nijhoff Publishers, 1986.
- [53] H. J. Herrmann, "Geometrical cluster growth models and kinetic gelation," *Phys. Rep.*, vol. 136, p. 153, 1986.
- [54] L. Onsager, "Crystal statistics. I. a two-dimensional model with an order-disorder transition," *Phys. Rev.*, vol. 65, p. 117, 1944.
- [55] K. Binder, "Applications of Monte Carlo methods to statistical physics," *Rep. Prog. Phys.*, vol. 60, p. 487, 1997.

-
- [56] D. P. Landau and K. Binder, *A Guide to Monte Carlo Simulations in Statistical Physics, 2nd Edition*. United Kingdom: Cambridge University Press, 2005.
- [57] M. Eden, "A two-dimensional growth process," in *Proceedings of Fourth Berkeley Symposium on Mathematics, Statistics, and Probability*, vol. 4, (University of California Press, Berkeley), p. 223, 1960.
- [58] P. Meakin, "Diffusion-controlled cluster formation in two, three, and four dimensions," *Phys. Rev. A*, vol. 27, p. 604, 1983.
- [59] E. A. Guggenheim, "The principle of corresponding states," *J. Chem. Phys.*, vol. 13, p. 253, 1945.
- [60] H. E. Stanley, *Introduction to phase transitions and critical phenomena*. United Kingdom: Oxford Science Publications, 1971.
- [61] L. P. Kadanoff, *Statistical Physics. Statics, Dynamics and Renormalization*. Singapore: World Scientific, 2000.
- [62] M. E. Fisher, "Renormalization group theory: Its basis and formulation in statistical physics," *Rev. Mod. Phys.*, vol. 70, p. 653, 1998.
- [63] V. Privman, ed., *Finite Size Scaling and Numerical Simulation of Statistical Systems*. Singapore: World Scientific, 1990.
- [64] P. Meakin, "The growth of rough surfaces and interfaces," *Phys. Rep.*, vol. 235, p. 189, 1993.
- [65] J. Krug, "Origins of scale invariance in growth processes," *Adv. Phys.*, vol. 46, p. 139, 1997.
- [66] V. Privman, *Finite-Size Scaling Theory*, ch. 1, p. 1. In [63], 1990.
- [67] R. Miranda, M. Ramos, and A. Cadilhe, "Finite-size scaling study of the ballistic deposition model in (1+1)-dimensions," *Comp. Mat. Sci.*, vol. 27, p. 224, 2003.

-
- [68] M. Kardar, G. Parisi, and Y. Zhang, “Dynamic scaling of growing interfaces,” *Phys. Rev. Lett.*, vol. 56, p. 889, 1986.
- [69] R. J. Baxter, *Exactly solved models in statistical mechanics*. United Kingdom: Academic Press, 1982.
- [70] M. P. Allen and D. J. Tildesley, *Computer simulation of liquids*. United Kingdom: Oxford University Press, 1987.
- [71] P. D. Bristowe and P. J. Hasnip, *General aspects of materials modelling*, ch. 1, p. 1. In Barber [47], 2005.
- [72] M. C. Payne, M. P. Teter, D. C. Allan, T. A. Arias, and J. D. Joannopoulos, “Iterative minimization techniques for *ab initio* total-energy calculations - Molecular-Dynamics and conjugate gradients,” *Rev. Mod. Phys.*, vol. 64, p. 1045, 1992.
- [73] R. Car and M. Parrinello, “Unified approach for Molecular Dynamics and Density-Functional Theory,” *Phys. Rev. Lett.*, vol. 55, p. 2471, 1985.
- [74] J. M. Thijssen, *Computational Physics*. United Kingdom: Cambridge University Press, 1999.
- [75] A. F. Voter, F. Montalenti, and T. C. Germann, “Extending the time scale in atomistic simulation of materials,” *Ann. Rev. Mater. Res.*, vol. 32, p. 321, 2002.
- [76] D. C. Rapaport, *The art of Molecular Dynamics Simulations, 2nd Edition*. United Kingdom: Cambridge University Press, 2004.
- [77] J. W. Evans, P. A. Thiel, and M. C. Bartelt, “Morphological evolution during epitaxial thin film growth: formation of 2D islands and 3D mounds,” *Surf. Sci. Rep.*, vol. 61, p. 1, 2006.

- [78] N. Metropolis, "The beginning of Monte Carlo method," *Los Alamos Science*, vol. 15, p. 125, 1987.
- [79] R. Eckhardt, "Stan Ulam, John von Neumann, and the Monte Carlo method," *Los Alamos Science*, vol. 15, p. 131, 1987.
- [80] N. Metropolis and S. Ulam, "The Monte Carlo method," *J. Am. Stat. Assoc.*, vol. 44, p. 335, 1949.
- [81] J. M. Hammersley and D. C. Handscomb, *Monte Carlo Methods*. United States of America: Chapman and Hall, 1964.
- [82] D. Stauffer and A. Aharony, *Introduction to percolation theory*. United Kingdom: Taylor and Francis Ltd., 1994.
- [83] M. B. Isichenko, "Percolation, statistical topography, and transport in random media," *Rev. Mod. Phys.*, vol. 64, p. 961, 1992.
- [84] J. Hoshen and R. Kopelman, "Percolation and cluster distribution. I. Cluster multiple labeling technique and critical concentration algorithm," *Phys. Rev. B*, vol. 14, p. 3438, 1976.
- [85] N. Metropolis, A. W. Rosenbluth, M. N. Rosenbluth, A. H. Teller, and E. Teller, "Equation of state calculations by fast computing machines," *J. Chem. Phys.*, vol. 21, p. 1087, 1953.
- [86] H. C. Kang and W. H. Weinberg, "Dynamic Monte Carlo with a proper energy barrier: Surface diffusion and two-dimensional domain ordering," *J. Chem. Phys.*, vol. 90, p. 2824, 1989.
- [87] K. A. Fichtorn and W. H. Weinberg, "Theoretical foundations of dynamical Monte Carlo simulations," *J. Chem. Phys.*, vol. 95, p. 1090, 1991.

- [88] A. B. Bortz, M. H. Kalos, and J. L. Lebowitz, "A new algorithm for Monte Carlo simulation of Ising spin systems," *J. Comp. Phys.*, vol. 17, p. 10, 1975.
- [89] L. A. Ray and R. C. Baetzold, "A Monte Carlo estimation of surface diffusion by stimulating laser-induced thermal desorption," *J. Chem. Phys.*, vol. 93, p. 2871, 1990.
- [90] A. Chatterjee and D. G. Vlachos, "An overview of spatial microscopic and accelerated kinetic Monte Carlo methods," *J. Computer-Aided Mater. Des.*, vol. 14, p. 253, 2007.
- [91] D. G. Truhlar, B. C. Garrett, and S. J. Klippenstein, "Current status of transition-state theory," *J. Phys. Chem.*, vol. 100, p. 12771, 1996.
- [92] G. Henkelman and H. Jónsson, "A dimer method for finding saddle points on high dimensional potential surfaces using only first derivatives," *J. Chem. Phys.*, vol. 111, p. 7010, 1999.
- [93] G. Henkelman, B. P. Uberuaga, and H. Jónsson, "A climbing image nudged elastic band method for finding saddle points and minimum energy paths," *J. Chem. Phys.*, vol. 113, p. 9901, 2000.
- [94] G. Henkelman and H. Jónsson, "Improved tangent estimate in the nudged elastic band method for finding minimum energy paths and saddle points," *J. Chem. Phys.*, vol. 113, p. 9978, 2000.
- [95] P. G. Bolhuis, D. Chandler, C. Dellago, and P. L. Geissler, "Transition path sampling: Throwing ropes over rough mountain passes, in the dark," *Annu. Rev. Phys. Chem.*, vol. 53, p. 291, 2002.
- [96] H. Jónsson, "Theoretical studies of atomic-scale processes relevant to crystal growth," *Annu. Rev. Phys. Chem.*, vol. 51, p. 623, 2000.

-
- [97] A. F. Voter, "Classically exact overlayer dynamics: diffusion of rhodium clusters on Rh(100)," *Phys. Rev. B*, vol. 34, p. 6819, 1986.
- [98] G. H. Vineyard, "Frequency factors and isotope effects in solid state rate processes," *J. Phys. Chem. Solids*, vol. 3, p. 121, 1957.
- [99] A. Pedersen and H. Jónsson, "Distributed implementation of the adaptive Kinetic Monte Carlo method," *Math. Comput. Simul.*, 2009. doi:10.1016/j.matcom.2009.02.010.
- [100] D. T. Gillespie, "Approximate accelerated stochastic simulation of chemically reacting systems," *J. Chem. Phys.*, vol. 115, p. 1716, 2001.
- [101] M. Merrick and K. A. Fichthorn, "Synchronous relaxation algorithm for parallel kinetic Monte Carlo simulations of thin film growth," *Phys. Rev. E*, vol. 75, p. 011606, 2007.
- [102] F. Shi, Y. Shim, and J. G. Amar, "Parallel kinetic Monte Carlo simulations of two-dimensional island coarsening," *Phys. Rev. E*, vol. 76, p. 031607, 2007.
- [103] M. R. Sørensen and A. F. Voter, "Temperature-accelerated dynamics for simulation of infrequent events," *J. Chem. Phys.*, vol. 112, p. 9599, 2000.
- [104] G. Henkelman and H. Jónsson, "Long time scale kinetic Monte Carlo simulations without lattice approximation and predefined event table," *J. Chem. Phys.*, vol. 115, p. 9657, 2001.
- [105] O. Trushin, A. Karim, A. Kara, and T. S. Rahman, "Self-learning kinetic Monte Carlo method: Application to Cu(111)," *Phys. Rev. B*, vol. 72, p. 115401, 2005.
- [106] A. F. Voter, "A method for accelerating the molecular dynamics simulation of infrequent events," *J. Chem. Phys.*, vol. 106, p. 4665, 1997.

-
- [107] A. F. Voter, "Parallel replica method for dynamics of infrequent events," *Phys. Rev. B*, vol. 57, p. R13985, 1998.
- [108] F. Montalenti and A. F. Voter, "Applying accelerated molecular dynamics to crystal growth," *phys. stat. sol. (b)*, vol. 226, p. 21, 2001.
- [109] F. Montalenti, M. R. Sørensen, and A. F. Voter, "Closing the gap between experimental and theory: crystal growth by temperature accelerated dynamics," *Phys. Rev. Lett.*, vol. 87, p. 126101, 2001.
- [110] F. Montalenti and A. F. Voter, "Exploiting past visits or minimum-barrier knowledge to gain further boost in the temperature-accelerated dynamics method," *J. Chem. Phys.*, vol. 116, p. 4819, 2002.
- [111] J. A. Sprague, F. Montalenti, B. P. Uberuaga, J. D. Kress, and A. F. Voter, "Simulation of growth of Cu on Ag(001) at experimental deposition rates," *Phys. Rev. B*, vol. 66, p. 205415, 2002.
- [112] B. P. Uberuaga, S. J. Stuart, and A. F. Voter, "Parallel replica dynamics for driven systems: Derivation and application to strained nanotubes," *Phys. Rev. B*, vol. 75, p. 014301, 2007.
- [113] K. A. Fichthorn, R. A. Miron, Y. Wang, and Y. Tiwary, "Accelerated molecular dynamics simulation of thin-film growth with the bond-boost method," *J. Phys.: Condens. Matter*, vol. 21, p. 084212, 2009.
- [114] K. E. Becker, M. H. Mignogna, and K. A. Fichthorn, "Accelerated Molecular Dynamics of temperature-programed desorption," *Phys. Rev. Lett.*, vol. 102, p. 046101, 2009.
- [115] T. Opplestrup, V. V. Bulatov, G. H. Gilmer, M. H. Kalos, and B. Sadigh, "First-passage Monte Carlo algorithm: Diffusion without all the hops," *Phys. Rev. Lett.*, vol. 97, p. 230602, 2006.

- [116] M. A. Novotny, "Monte Carlo algorithms with adsorbing Markov chains: fast local algorithms for slow dynamics," *Phys. Rev. Lett.*, vol. 74, p. 1, 1995.
- [117] P. J. Flory, "Intramolecular reaction between neighboring substituents of vinyl polymers," *J. Am. Chem. Soc.*, vol. 61, p. 1518, 1939.
- [118] A. Rényi, "Egy egydimenziós véletlen térkitöltési problémáról," *Publ. Math. Inst. Hung. Acad. Sci.*, vol. 3, p. 109, 1958.
- [119] A. Rényi, "On a one-dimensional problem concerning random space filling," *Sel. Trans. Math. Stat. Prob.*, vol. 4, p. 203, 1963.
- [120] J. J. González, P. C. Hemmer, and J. S. Høye, "Cooperative effects in random sequential polymer reactions," *Chem. Phys.*, vol. 3, p. 228, 1974.
- [121] J. W. Evans, "Random and cooperative sequential adsorption," *Rev. Mod. Phys.*, vol. 65, p. 1281, 1993.
- [122] V. Privman, "Dynamics of nonequilibrium processes: surface adsorption, reaction-diffusion kinetics, ordering and phase separation," *Trends in Stat. Phys.*, vol. 1, p. 89, 1994.
- [123] V. Privman, ed., *Nonequilibrium Statistical Mechanics in One Dimension*. Cambridge, United Kingdom: Cambridge University Press, 1997.
- [124] J. Marro and R. Dickman, *Nonequilibrium Phase Transitions in Lattice Models*. Cambridge, United Kingdom: Cambridge University Press, 1999.
- [125] V. Privman, "Recent theoretical results for nonequilibrium deposition of submicron particles," *J. Adhesion*, vol. 74, p. 421, 2000.
- [126] V. Privman, "Dynamics of nonequilibrium deposition," *Coll. and Surf. A*, vol. 165, p. 231, 2000.

-
- [127] J. Talbot, G. Tarjus, P. R. van Tassel, and P. Viot, "From car parking to protein adsorption: an overview of sequential adsorption processes," *Coll. and Surf. A*, vol. 165, p. 287, 2000.
- [128] A. Cadilhe, N. A. M. Araújo, and V. Privman, "Random sequential adsorption: from continuum to lattice and pre-patterned substrates," *J. Phys.: Condens. Matter*, vol. 19, p. 065124, 2007.
- [129] P. Seba, "Markov chain of distances between parked cars," *J. Phys. A: Math. Theor.*, vol. 41, p. 122003, 2008.
- [130] G. Y. Onoda and E. G. Liniger, "Experimental determination of the random-parking limit in two-dimensions," *Phys. Rev. A*, vol. 33, p. 715, 1986.
- [131] P. L. Krapivsky and E. Ben-Naim, "Collective properties of adsorption-desorption processes," *J. Chem. Phys.*, vol. 100, p. 6778, 1994.
- [132] P. R. van Tassel, P. Viot, G. Tarjus, J. R. Ramsden, and J. Talbot, "Enhanced saturation coverages in adsorption-desorption processes," *J. Chem. Phys.*, vol. 112, p. 1483, 2000.
- [133] B. Bonnier, "Diffusional relaxation in a random sequential adsorption model," *Phys. Rev. E*, vol. 56, p. 7304, 1997.
- [134] P. Nielaba, "Lattice models of irreversible adsorption and diffusion." in ref. [123], p. 229.
- [135] V. Privman and J.-S. Wang, "Asymptotic layer coverage in deposition models without screening," *Phys. Rev. A*, vol. 45, p. R2155, 1992.
- [136] P. Nielaba and V. Privman, "Kinetic roughening in deposition with suppressed screening," *Phys. Rev. E*, vol. 51, p. 2022, 1995.

-
- [137] A. V. Subashiev and S. Luryi, “Random sequential adsorption of shrinking or expanding particles,” *Phys. Rev. E*, vol. 75, p. 011123, 2007.
- [138] J. W. Lee, “Kinetics of random sequential adsorption on disordered substrates,” *J. Phys. A*, vol. 29, p. 33, 1996.
- [139] M. R. D’Orsogna and T. Chou, “Interparticle gap distributions on one-dimensional lattices,” *J. Phys. A*, vol. 38, p. 531, 2005.
- [140] G. Kondrat, “The effect of impurities on jamming in random sequential adsorption of elongate objects,” *J. Chem. Phys.*, vol. 124, p. 054713, 2006.
- [141] P. Weroński, “Application of the extended RSA models in studies of particle deposition at partially covered surfaces,” *Adv. Colloid Interface Sci.*, vol. 118, p. 1, 2005.
- [142] M. C. Bartelt, “Random sequential filling of a finite line,” *Phys. Rev. A*, vol. 43, p. 3149, 1991.
- [143] B. Bonnier, “Random sequential adsorption of binary mixtures on a line,” *Phys. Rev. E*, vol. 64, p. 066111, 2001.
- [144] M. K. Hassan and J. Kurths, “Competitive random sequential adsorption of point and fixed-sized particles: Analytical results,” *J. Phys. A*, vol. 34, p. 7517, 2001.
- [145] M. K. Hassan, J. Schmidt, B. Blasius, and J. Kurths, “Jamming coverage in competitive random sequential adsorption of a binary mixture,” *Phys. Rev. E*, vol. 65, p. 045103(R), 2002.
- [146] N. A. M. Araújo and A. Cadilhe, “Gap-size distribution functions of a random sequential adsorption model of segments on a line,” *Phys. Rev. E*, vol. 73, p. 051602, 2006.

- [147] A. V. Subashiev and S. Luryi, "Fluctuations of the partial filling factors in competitive random sequential adsorption from binary mixtures," *Phys. Rev. E*, vol. 76, p. 011128, 2007.
- [148] M. C. Bartelt and V. Privman, "Kinetics of irreversible adsorption of mixtures of pointlike and fixed-size particles: Exact results.," *Phys. Rev. A*, vol. 44, p. R2227, 1991.
- [149] A. Cadilhe and V. Privman, "Random sequential adsorption of mixtures of dimers and monomers on a pre-treated Bethe lattice," *Mod. Phys. Lett. B*, vol. 18, p. 207, 2004.
- [150] B. Senger, J.-C. Voegel, P. Schaaf, A. Johner, A. Schmitt, and J. Talbot, "Properties of jamming configurations built up by the adsorption of brownian particles onto solid surfaces," *Phys. Rev. A*, vol. 44, p. 6926, 1991.
- [151] B. Senger, P. Schaaf, J. C. Voegel, A. Johner, A. Schmitt, and J. Talbot, "Influence of bulk diffusion on the adsorption of hard spheres on a flat surface," *J. Chem. Phys.*, vol. 97, p. 3813, 1992.
- [152] E. Kumacheva, R. K. Golding, M. Allard, and E. H. Sargent, "Colloid crystal growth on mesoscopically patterned surfaces: effect of confinement," *Adv. Mater.*, vol. 14, p. 221, 2002.
- [153] C.-A. Fustin, G. Glasser, H. W. Spiess, and U. Jonas, "Site-selective growth of colloidal crystals with photonic properties on chemically patterned surfaces," *Adv. Mater.*, vol. 15, p. 1025, 2003.
- [154] G. Zhu, C. Wang, Y. Zhang, N. Guo, Y. Zhao, R. Wang, S. Qiu, Y. Wei, and R. H. Baughman, "Highly effective sulfated zirconia nanocatalysts grown out of colloidal silica at high temperature," *Chem. Eur. J.*, vol. 10, p. 4750, 2004.

- [155] C. Burda, X. Chen, R. Narayanan, and M. A. El-Sayed, "Chemistry and properties of nanocrystals of different shapes," *Chem. Rev.*, vol. 105, p. 1025, 2005.
- [156] P. C. Lewis, E. Kumacheva, M. Allard, and E. H. Sargent, "Colloidal crystallization accomplished by electrodeposition on patterned substrates," *J. Disp. Sci. and Technol.*, vol. 26, p. 259, 2005.
- [157] E. O'Connor, A. O'Riordan, H. Doyle, S. Moynihan, A. Cuddihy, and G. Redmond, "Near-infrared electroluminescent devices based on colloidal HgTe quantum dot arrays," *App. Phys. Lett.*, vol. 86, p. 201114, 2005.
- [158] L. Yang, Z. Yang, W. Cao, L. Chen, J. Xu, and H. Zhang, "Luminescence 3D-ordered porous materials composed of CdSe and CdTe nanocrystals," *J. Phys. Chem. B*, vol. 109, p. 11501, 2005.
- [159] N. L. Jeon, W. Lin, M. K. Erhardt, G. S. Girolami, and R. G. Nuzzo, "Selective chemical vapor deposition of platinum and palladium directed by monolayers patterned using microcontact printing," *Langmuir*, vol. 13, p. 3833, 1997.
- [160] J. Y. Chen, J. F. Klemic, and M. Elimelech, "Micropatterning microscopic charge heterogeneity on flat surfaces for studying the interaction between colloidal particles and heterogeneously charged surfaces," *Nano Lett.*, vol. 2, p. 393, 2002.
- [161] M. Elimelech, J. Y. Chen, and Z. A. Kuznar, "Particle deposition onto solid surfaces with micropatterned charge heterogeneity: The "hydrodynamic bump" effect," *Langmuir*, vol. 19, p. 6594, 2003.
- [162] J. Joo, B. Y. Chow, and J. M. Jacobson, "Nanoscale patterning on insulating substrates by critical energy electron beam lithography," *Nano Lett.*, vol. 6, p. 2021, 2006.
- [163] D. Xia, D. Li, Y. Luo, and S. R. J. Brueck, "An approach to lithographically defined self-assembled nanoparticles films," *Adv. Mat.*, vol. 18, p. 930, 2006.

- [164] W. R. Childs and R. G. Nuzzo, "Decal transfer microlithography: A new soft-lithographic patterning method," *J. Am. Chem. Soc.*, vol. 124, p. 13583, 2002.
- [165] T. W. Odom, V. R. Thalladi, J. C. Love, and G. M. Whitesides, "Generation of 30-50 nm structures using easily fabricated, composite PDMS masks," *J. Am. Chem. Soc.*, vol. 124, p. 12112, 2002.
- [166] K. E. Paul, M. Prentiss, and G. M. Whitesides, "Patterning spherical surfaces at the two-hundred-nanometer scale using soft lithography," *Adv. Func. Mater.*, vol. 13, p. 259, 2003.
- [167] M.-H. Wu, C. Park, and G. M. Whitesides, "Generation of submicrometer structures by photolithography using arrays of spherical microlenses," *J. Coll. Interf. Sci.*, vol. 265, p. 304, 2003.
- [168] Y. Cui, M. T. Björk, J. A. Liddle, C. Sönnichsen, B. Boussert, and A. P. Alivisatos, "Integration of colloidal nanocrystals into lithographically patterned devices," *Nano Lett.*, vol. 4, p. 1093, 2004.
- [169] M. C. Bartelt and V. Privman, "Kinetic of irreversible monolayer and multilayer adsorption," *Int. J. Mod. Phys. B*, vol. 5, p. 2883, 1991.
- [170] B. Bonnier, "On the random sequential adsorption of d -dimensional cubes," *J. Phys. A*, vol. 34, p. 10757, 2001.
- [171] M. C. Bartelt and J. W. Evans, "Scaling of spatial correlations in cooperative sequential adsorption with clustering," *J. Stat. Phys.*, vol. 76, p. 867, 1994.
- [172] B. Bonnier, M. Hontebeyrie, Y. Leroyer, C. Meyers, and E. Pommiers, "Adsorption of line segments on a square lattice," *Phys. Rev. E*, vol. 49, p. 305, 1994.
- [173] N. V. Brilliantov, Y. A. Andrienko, P. L. Krapivsky, and J. Kurths, "Fractal formation and ordering in random sequential adsorption," *Phys. Rev. Lett.*, vol. 76, p. 4058, 1996.

-
- [174] V. Privman (ed.), “Adhesion of submicron particles on solid surfaces,” *Adhesion of submicron particles on solid surfaces, Coll. and Surfaces A*, vol. 165, Nos. 1-3, 2000.
- [175] J. Feder, “Random sequential adsorption,” *J. Theor. Biology*, vol. 87, p. 237, 1980.
- [176] J. Feder and I. Giaever, “Adsorption of ferritin,” *J. Colloid Interf. Sci.*, vol. 78, p. 144, 1980.
- [177] Y. Pomeau, “Some asymptotic estimates in the random parking problem,” *J. Phys. A*, vol. 13, p. L193, 1980.
- [178] R. H. Swendsen, “Dynamics of random sequential adsorption,” *Phys. Rev. A*, vol. 24, p. 504, 1981.
- [179] B. J. Brosilow, R. M. Ziff, and R. D. Vigil, “Random sequential adsorption of parallel squares,” *Phys. Rev. A*, vol. 43, p. 631, 1991.
- [180] V. Privman, J.-S. Wang, and P. Nielaba, “Continuum limit in random sequential adsorption,” *Phys. Rev. B*, vol. 43, p. 3366, 1991.
- [181] M. J. de Oliveira, T. Tomé, and R. Dickman, “Anisotropic random sequential adsorption of dimers on a square lattice,” *Phys. Rev. A*, vol. 46, p. 6294, 1992.
- [182] J. W. Lee, “Effects of impurities in random sequential adsorption on a one-dimensional substrate,” *Phys. Rev. E*, vol. 55, p. 3731, 1997.
- [183] E. S. Loscar, R. A. Borzi, and E. V. Albano, “Fluctuations of jamming coverage upon random sequential adsorption on homogeneous and heterogeneous media,” *Phys. Rev. E*, vol. 68, p. 041106, 2003.
- [184] G. Döge, “Perfect simulation for random sequential adsorption of d-dimensional spheres with random radii,” *J. Statist. Comput. Simul.*, vol. 69, p. 141, 2000.
- [185] K. Bagi, “An algorithm to generate random dense arrangements for discrete element simulations of granular assemblies,” *Granular Matter*, vol. 7, p. 31, 2005.

- [186] P. Katira, A. Agarwal, and H. Hess, "A random sequential adsorption model for protein adsorption to surfaces functionalized with Poly(ethylene oxide)," *Adv. Mater.*, vol. 20, p. 1, 2008.
- [187] N. A. M. Araújo, A. Cadilhe, and V. Privman, "Morphology of fine-particle monolayers deposited on nanopatterned substrates," *Phys. Rev. E*, vol. 77, p. 031603, 2008.
- [188] J. F. Marques, A. B. Lima, N. A. M. Araújo, and A. Cadilhe, "The interplay between size distribution and substrate pattern in the adsorption of colloidal particles." unpublished.
- [189] N. A. M. Araújo, A. Cadilhe, and V. Privman unpublished.
- [190] A. A. Guzelian, U. Banin, A. V. Kadavanich, X. Peng, and A. P. Alivisatos, "Colloidal chemical synthesis and characterization of InAs nanocrystal quantum dots," *Appl. Phys. Lett.*, vol. 69, p. 1432, 1996.
- [191] T. Teranishi and M. Miyake, "Size control of palladium nanoparticles and their crystal structures," *Chem. Mater.*, vol. 10, p. 594, 1998.
- [192] T. Teranishi, M. Hosoe, T. Tanaka, and M. Miyake, "Size control of monodispersed Pt nanoparticles and their 2D organization by electrophoretic deposition," *J. Phys. Chem. B*, vol. 103, p. 3818, 1999.
- [193] T. Teranishi and M. Miyake, "Novel synthesis of monodispersed Pd/Ni nanoparticles," *Chem. Mater.*, vol. 11, p. 3414, 1999.
- [194] X. Peng, L. Manna, W. Yang, J. Wickham, E. Scher, A. Kadavanich, and A. P. Alivisatos, "Shape control of CdSe nanocrystals," *Nature*, vol. 404, p. 59, 2000.
- [195] J. Park, V. Privman, and E. Matijević, "Model of formation of monodispersed colloids," *J. Phys. Chem. B*, vol. 105, p. 11630, 2001.

- [196] Z. A. Peng and X. Peng, "Formation of high-quality CdTe, CdSe, and CdS nanocrystals using CdO as precursor," *J. Am. Chem. Soc.*, vol. 123, p. 183, 2001.
- [197] Z. A. Peng and X. Peng, "Mechanisms of the shape evolution of CdSe nanocrystals," *J. Am. Chem. Soc.*, vol. 123, p. 1389, 2001.
- [198] L. Qu, Z. A. Peng, and X. Peng, "Alternative routes toward high quality CdSe nanocrystals," *Nano Lett.*, vol. 1, p. 333, 2001.
- [199] N. Toshima, Y. Shiraishi, T. Teranishi, M. Miyake, T. Tominaga, H. Watanabe, W. Brijoux, H. Bönemann, and G. Schmid, "Various ligand-stabilized metal nanoclusters as homogeneous and heterogeneous catalysts in the liquid phase," *App. Organometal. Chem.*, vol. 15, p. 178, 2001.
- [200] D. Battaglia and X. Peng, "Formation of high quality InP and InAs nanocrystals in a noncoordinating solvent," *Nano Lett.*, vol. 2, p. 1027, 2002.
- [201] Z. A. Peng and X. Peng, "Nearly monodisperse and shape-controlled CdSe nanocrystals via alternative routes: Nucleation and growth," *J. Am. Chem. Soc.*, vol. 124, p. 3343, 2002.
- [202] W. W. Yu and X. Peng, "Formation of high-quality CdS and other II-VI semiconductor nanocrystals in noncoordinating solvents: Tunable reactivity of monomers," *Angew. Chem. Int. Ed.*, vol. 41, p. 2368, 2002.
- [203] S. Libert, D. V. Goia, and E. Matijević, "Internally composite uniform colloidal cadmium sulfide spheres," *Langmuir*, vol. 19, p. 10673, 2003.
- [204] S. Libert, V. Gorshkov, D. Goia, E. Matijević, and V. Privman, "Model of controlled synthesis of uniform colloid particles: cadmium sulfide," *Langmuir*, vol. 19, p. 10679, 2003.
- [205] V. Privman, "Mechanisms of diffusional nucleation of nanocrystals and their self-assembly into uniform colloids," *Ann. N. Y. Acad. Sci.*, vol. 1161, p. 508, 2009.

-
- [206] V. Privman, "Dissociative adsorption: a solvable model of "hot" deposition," *Europhys. Lett.*, vol. 23, p. 341, 1993.
- [207] J.-S. Wang, P. Nielaba, and V. Privman, "Locally frozen defects in random sequential adsorption with diffusional relaxation," *Physica A*, vol. 199, p. 527, 1993.
- [208] J.-S. Wang, P. Nielaba, and V. Privman, "Collective effects in random sequential adsorption of diffusing hard squares," *Modern Phys. Lett. B*, vol. 7, p. 189, 1993.
- [209] P. Nielaba, V. Privman, and J.-S. Wang, "Irreversible multilayer adsorption," *Ber. Bunsenges. Phys. Chem.*, vol. 98, p. 451, 1994.
- [210] M. D. Grynberg and R. B. Stinchcombe, "Dynamic correlation functions of adsorption stochastic systems with diffusional relaxation," *Phys. Rev. Lett.*, vol. 74, p. 1242, 1995.
- [211] D. Stauffer, ed., *Annual Reviews of Computational Physics*, vol. III, ch. Dynamics of Nonequilibrium Desposition with Diffusional Relaxation, V. Privman, p. 177. Singapore: World Scientific, 1995.
- [212] P. Lavalley, P. Schaaf, M. Ostafin, J.-C. Voegel, and B. Senger, "Extended random sequential adsorption model of irreversible deposition processes: from simulations to experiments," *Proc. Natl. Acad. Sci. USA*, vol. 96, p. 11100, 1999.
- [213] E. W. James, D.-J. Liu, and J. W. Evans, "Relaxation effects in random sequential adsorption: application to chemisorption systems," *Coll. and Surf. A*, vol. 165, p. 241, 2000.
- [214] C. Fusco, P. Gallo, A. Petri, and M. Rovere, "Random sequential adsorption and diffusion of dimers and k -mers on a square lattice," *J. Chem. Phys.*, vol. 114, p. 7563, 2001.
- [215] P. Nielaba and V. Privman, "Multilayer adsorption with increasing layer coverage," *Phys. Rev. A*, vol. 45, p. 6099, 1992.

- [216] M. Bardosova and R. H. Tredgold, "Ordered layers of monodisperse colloids," *J. Mater. Chem.*, vol. 12, p. 2835, 2002.
- [217] Z. Adamczyk, K. Jaszczólt, A. Michna, B. Siwek, L. Szyk-Warszyńska, and M. Zem-bala, "Irreversible adsorption of particles on heterogeneous surfaces," *Adv. Colloid Interface Sci.*, vol. 118, p. 25, 2005.
- [218] J. Talbot and P. Schaaf, "Random sequential adsorption of mixtures," *Phys. Rev. A*, vol. 40, p. 422, 1989.
- [219] N. M. Švrakić and M. Henkel, "Kinetics of irreversible deposition of mixtures," *J. Phys. I*, vol. 1, p. 791, 1991.
- [220] A. S. McLeod and L. F. Gladden, "The influence of the random sequential adsorption of binary mixtures on the kinetics of hydrocarbon hydrogenation reactions," *J. Chem. Phys.*, vol. 110, p. 4000, 1999.
- [221] I. Lončarević, L. Budinski-Petković, and S. B. Vrhovac, "Reversible random sequential adsorption of mixtures on a triangular lattice," *Phys. Rev. E*, vol. 76, p. 031104, 2007.
- [222] M. Tanemura, "On random complete packing by disks," *Ann. Inst. Stat. Math.*, vol. 31, p. 351, 1979.
- [223] E. L. Hinrichsen, J. Feder, and T. Jøssang, "Geometry of random sequential adsorption," *J. Stat. Phys.*, vol. 44, p. 793, 1986.
- [224] P. Meakin and R. Jullien, "Random-sequential adsorption of disks of different sizes," *Phys. Rev. A*, vol. 46, p. 2029, 1992.
- [225] J.-S. Wang, "A fast algorithm for random sequential adsorption of disks," *Int. J. Mod. Phys. C*, vol. 5, p. 707, 1994.

- [226] S. Torquato, O. U. Uche, and F. H. Stillinger, "Random sequential addition of hard spheres in high Euclidean dimensions," *Phys. Rev. E*, vol. 74, p. 061308, 2006.
- [227] P. Viot and G. Tarjus, "Random sequential addition of unoriented squares: Breakdown of Swendsen's conjecture," *Europhys. Lett.*, vol. 13, p. 295, 1990.
- [228] P. Viot, G. Tarjus, S. M. Ricci, and J. Talbot, "Random sequential adsorption of anisotropic particles. I. Jamming limit and asymptotic behavior," *J. Chem. Phys.*, vol. 97, p. 5212, 1992.
- [229] P. Meakin and R. Jullien, "Random sequential adsorption of spheres of different sizes," *Physica A*, vol. 187, p. 475, 1992.
- [230] Z. Adamczyk, B. Siwek, M. Zembala, and P. Weroński, "Influence of polydispersity on random sequential adsorption of spherical particles," *J. Coll. Interf. Sci.*, vol. 185, p. 236, 1997.
- [231] Z. Adamczyk, J. Barbasz, and M. Nattich, "Particle assembly on patterned surfaces bearing circular (dots) and rectangular (stripes) surface features," *Langmuir*, vol. 24, p. 1756, 2008.
- [232] J. Talbot, G. Tarjus, and P. Viot, "Equilibrium adsorption on a random site surface," *J. Phys. Chem. B*, vol. 112, p. 13051, 2008.
- [233] V. Privman, H. L. Frisch, N. Ryde, and E. Matijević, "Particle adhesion in model systems. Part 13 - theory of multilayer deposition," *J. Chem. Soc. Faraday Trans.*, vol. 87, p. 1371, 1991.
- [234] S. M. S. Pereira, M. A. Martins, T. Trindade, I. M. Watson, D. Zhu, and C. J. Humphreys, "Controlled integration of nanocrystals in inverted hexagonal nanopits at the surface of light-emitting heterostructures," *Adv. Mater.*, vol. 20, p. 1038, 2008.

-
- [235] J. Talbot, G. Tarjus, and P. Schaaf, "Unexpected asymptotic behavior in random sequential adsorption of nonspherical particles," *Phys. Rev. A*, vol. 40, p. 4808, 1989.
- [236] B. Bonnier, D. Boyer, and P. Viot, "Pair correlation function in random sequential adsorption processes," *J. Phys. A*, vol. 27, p. 3671, 1994.
- [237] Z. Adamczyk, M. Zembala, B. Siwek, and P. Warszyński, "Structure and ordering in localized adsorption of particles," *J. Coll. Interf. Sci.*, vol. 140, p. 123, 1990.
- [238] Z. Adamczyk, B. Siwek, M. Zembala, and P. Belouschek, "Kinetics of localized adsorption of colloid particles," *Adv. Colloid. Int. Sci.*, vol. 48, p. 151, 1994.
- [239] P. A. Thiel and J. W. Evans, "Energetic parameters for atomic-scale processes on Ag(100)," *J. Phys. Chem. B*, vol. 108, p. 14428, 2004.
- [240] N. W. Ashcroft and N. D. Mermin, *Solid State Physics*. United States of America: Thomson Learning, 1976.
- [241] H. Brune, M. Giovannini, K. Bromann, and K. Kern, "Self-organized growth of nanostructure arrays on strain-relief patterns," *Nature*, vol. 394, p. 451, 1998.
- [242] L. Royer *Bull. Soc. Fr. Mineralog. Crystallogr.*, vol. 51, p. 7, 1928.
- [243] Y. W. Mo, J. Kleiner, M. B. Webb, and M. G. Lagally, "Activation energy for surface diffusion of Si on Si(001): a scanning-tunneling-microscopy study," *Phys. Rev. Lett.*, vol. 66, p. 1998, 1991.
- [244] J. A. Stroscio, D. T. Pierce, and R. A. Dragoset, "Homoepitaxial growth of iron and a real space view of reflection-high-energy-electron diffraction," *Phys. Rev. Lett.*, vol. 70, p. 3615, 1993.
- [245] J. A. Stroscio and D. T. Pierce, "Scaling of diffusion-mediated island growth in iron-on-iron homoepitaxy," *Phys. Rev. B*, vol. 49, p. 8522, 1994.

- [246] B. Müller, L. Nedelmann, B. Fischer, H. Brune, and K. Kern, “Initial stages of Cu epitaxy on Ni(100): postnucleation and a well-defined transition in critical island size,” *Phys. Rev. B*, vol. 54, p. 17858, 1996.
- [247] A. Pimpinelli and J. Villain, *Physics of Crystal Growth*. United Kingdom: Cambridge University Press, 1998.
- [248] H. Brune, G. S. Bales, J. Jacobsen, C. Boragno, and K. Kern, “Measuring surface diffusion from nucleation island densities,” *Phys. Rev. B*, vol. 60, p. 5991, 1999.
- [249] K. A. Fichthorn and M. Scheffler, “Island nucleation in thin-film epitaxy: a first-principles investigation,” *Phys. Rev. Lett.*, vol. 84, p. 5371, 2000.
- [250] F. Much, M. Ahr, M. Biehl, and W. Kinzel, “Kinetic Monte Carlo simulations of dislocations in heteroepitaxial growth,” *Europhys. Lett.*, vol. 56, p. 791, 2001.
- [251] F. Much and M. Biehl, “Simulation of wetting-layer and island formation in heteroepitaxial growth,” *Europhys. Lett.*, vol. 63, p. 14, 2003.
- [252] M. Biehl, M. Ahr, W. Kinzel, and F. Much, “Kinetic Monte Carlo simulations of heteroepitaxial growth,” *Thin Solid Films*, vol. 428, p. 52, 2003.
- [253] T. Michely and J. Krug, *Islands, mounds and atoms: Patterns and processes in crystal growth far from equilibrium*. Germany: Springer, 2004.
- [254] J. W. Evans and M. C. Bartelt, “Nucleation, growth, and kinetic roughening of metal(100) homoepitaxial thin films,” *Langmuir*, vol. 12, p. 217, 1996.
- [255] I. Furman and O. Biham, “Effects of mobility of small islands on growth in molecular-beam epitaxy,” *Phys. Rev. B*, vol. 55, p. 7917, 1997.
- [256] H. Brune, “Microscopic view of epitaxial metal growth: nucleation and aggregation,” *Surf. Sci. Rep.*, vol. 31, p. 121, 1998.

- [257] A. F. Voter and J. D. Doll, "Transition state theory description of surface self-diffusion: Comparison with classical trajectory results," *J. Chem. Phys.*, vol. 80, p. 5832, 1984.
- [258] M. C. Bartelt and J. W. Evans, "Scaling analysis of diffusion-mediated island growth in surface adsorption processes," *Phys. Rev. B*, vol. 46, p. 12675, 1992.
- [259] J. G. Amar, F. Family, and P.-M. Lam, "Dynamic scaling of the island-size distribution and percolation in a model of submonolayer molecular-beam epitaxy," *Phys. Rev. B*, vol. 50, p. 8781, 1994.
- [260] F. Family, "Scaling, percolation and coarsening in epitaxial thin film growth," *Physica A*, vol. 266, p. 173, 1999.
- [261] J. G. Amar and F. Family, "Critical cluster size: Island morphology and size distribution in submonolayer epitaxial growth," *Phys. Rev. Lett.*, vol. 74, p. 2066, 1995.
- [262] M. C. Bartelt and J. W. Evans, "Exact island-size distributions for submonolayer deposition: Influence of correlations between island size and separation," *Phys. Rev. B*, vol. 54, p. R17359, 1996.
- [263] M. C. Bartelt, J. B. Hannon, A. K. Schmid, C. R. Stoldt, and J. W. Evans, "Island formation during deposition or etching," *Colloid Surface A*, vol. 165, p. 373, 2000.
- [264] J. W. Evans and M. C. Bartelt, "Nucleation, adatom capture, and island size distributions: Unified scaling analysis for submonolayer deposition," *Phys. Rev. B*, vol. 63, p. 235408, 2001.
- [265] S. B. Lee, "Influence of morphology of islands and of mobile clusters on island formation in molecular-beam epitaxy," *Phys. Rev. B*, vol. 73, p. 035437, 2006.
- [266] C. R. Stoldt, A. M. Cadilhe, C. J. Jenks, J.-M. Wen, J. W. Evans, and P. A. Thiel, "Evolution of far-from-equilibrium nanostructures formed by cluster-step and cluster-cluster coalescence in metal films," *Phys. Rev. Lett.*, vol. 81, p. 2950, 1998.

- [267] C. R. Stoldt, A. M. Cadilhe, M. C. Bartelt, C. J. Jenks, J. W. Evans, and P. A. Thiel, "Formation and relaxation of 2D island arrays in metal(100) homoepitaxy," *Prog. Surf. Sci.*, vol. 59, p. 67, 1998.
- [268] C. R. Stoldt, C. J. Jenks, P. A. Thiel, A. M. Cadilhe, and J. W. Evans, "Smoluchowski ripening of Ag islands on Ag(100)," *J. Chem. Phys.*, vol. 111, p. 5157, 1999.
- [269] A. M. Cadilhe, C. R. Stoldt, C. J. Jenks, P. A. Thiel, and J. W. Evans, "Evolution of far-from-equilibrium nanostructures on Ag(100) surfaces: Protrusions and indentations at extend step edges," *Phys. Rev. B*, vol. 61, p. 4910, 2000.
- [270] S. Frank, H. Wedler, R. J. Behm, J. Rottler, P. Maass, K. J. Caspersen, C. R. Stoldt, P. A. Thiel, and J. W. Evans, "Approaching the low-temperature limit in nucleation and two-dimensional growth of fcc(100) metal films Ag/Ag(100)," *Phys. Rev. B*, vol. 66, p. 155435, 2002.
- [271] C.-M. Zhang, M. C. Bartelt, J.-M. Wen, C. J. Jenks, J. W. Evans, and P. A. Thiel, "Submonolayer island formation and the onset of multilayer growth during Ag/Ag(100) homoepitaxy," *Surf. Sci.*, vol. 406, p. 178, 1998.
- [272] T. R. Mattsson, G. Mills, and H. Metiu, "A new method for simulating the late stages of island coarsening in thin film growth: The role of island diffusion and evaporation," *J. Chem. Phys.*, vol. 110, p. 12151, 1999.
- [273] J. A. Venables, *Introduction to Surface and Thin Film Processes*. United Kingdom: Cambridge University Press, 2000.
- [274] M. S. Daw and M. I. Baskes, "Embedded-atom method: derivation and application to impurities, surfaces, and other defects in metals," *Phys. Rev. B*, vol. 29, p. 6443, 1984.

-
- [275] C. Ratsch, A. Zangwill, P. Smilauer, and D. D. Vvedensky, "Saturation and scaling of epitaxial island densities," *Phys. Rev. Lett.*, vol. 72, p. 3194, 1994.
- [276] C.-M. Zhang, M. C. Bartelt, J.-M. Wen, C. J. Jenks, J. W. Evans, and P. A. Thiel, "The initial stages of Ag/Ag(100) homoepitaxy: scanning tunneling microscopy experiments and Monte Carlo simulations," *J. Cryst. Growth*, vol. 174, p. 851, 1997.
- [277] T. Vicsek and F. Family, "Dynamic scaling for aggregation of clusters," *Phys. Rev. Lett.*, vol. 52, p. 1669, 1984.
- [278] J. A. Venables, G. D. T. Spiller, and M. Hanbucken, "Nucleation and growth of thin films," *Rep. Prog. Phys.*, vol. 47, p. 399, 1984.
- [279] G. S. Bales and D. C. Chrzan, "Dynamics of irreversible island growth during sub-monolayer epitaxy," *Phys. Rev. B*, vol. 50, p. 6057, 1994.
- [280] J.-M. Wen, J. W. Evans, M. C. Bartelt, J. W. Burnett, and P. A. Thiel, "Coarsening mechanism in a metal film: from cluster diffusion to vacancy ripening," *Phys. Rev. Lett.*, vol. 76, p. 652, 1996.
- [281] J. R. Sanchez and J. W. Evans, "Diffusion of small clusters on metal (100) surfaces: Exact master-equation analysis for lattice-gas models," *Phys. Rev. B*, vol. 59, p. 3224, 1999.
- [282] O. Gromenko and V. Privman, "Random sequential adsorption of objects of decreasing size," *Phys. Rev. E*, vol. 79, p. 011104, 2009.

Index

- activation barrier, 134, 139
- activation energy, 13
- adsorption, 55, 81
 - colloidal particles, 55, 81
 - competitive, 55
 - irreversible, 83
 - kinetics, 81, 103
 - on a line, *see* Random Sequential Adsorption, on a line
 - on a surface, *see* Random Sequential Adsorption, on a surface
 - preadsorption, 55
 - regimes, 87, 95
 - segments, 57
- algorithm, 63, 110
- antiferromagnetic, 42
- Arrhenius equation, 13, 131
- aspect ratio, 58
- attempt frequency, 13, 47, 131
- binary mixture, 55, *see* adsorption, binary mixture
- Boltzmann constant, 15
- cell size, 83, 87
- cell-cell separation, 83, 87
- classical “exact” treatments, 134
- clean substrate, 81, 110
- colloids, 81
- continuity equation, 10
- critical size, 134
- crossover time, 27
- crystalline substrate, 13
- cumulants, 58, 69, 75, 77
 - higher-order, 69
- degrees of freedom, 7
- deposition, 129, 134
 - flux, 129, 134, 142
 - model, 134, 139
- detailed balance, 17, 42
- diffusion, 129, 131, 134
 - coefficient, 131
 - collective, 131
 - Einstein relation, 131
 - tracer, 131
- Dirac delta function, 15
- distribution of empty area, 103
- energy landscape, 13

-
- epitaxial
 - heteroepitaxial, 129
 - homoepitaxial, 129, 134
 - equilibrium system, 9
 - excluded volume, 57, 83
 - exponent, 22, 25, 27
 - exponential law, 103
 - far-from-equilibrium system, 9, 47, 129, 131, 134
 - ferromagnetic, 42
 - finite size, 27, 40, 47
 - flux, 58, 83
 - fundamental processes, 139
 - gap size distribution, 74
 - proposed function, 75
 - gap type, 58
 - generalized coordinates, 7
 - generalized momenta, 7
 - Hamilton
 - dynamics, 10
 - equations, 10
 - Hamiltonian, 42
 - hard-core interaction, *see* excluded volume
 - Heisenberg, 10
 - homogeneous function, 22
 - hopping rate, *see* transition rate
 - ICCA (interacting cell-cell adsorption), 87, 95
 - infrequent events, 13, 47, 131
 - integrable systems, 10
 - interface width, *see* roughness, *see* roughness
 - interparticle distribution function, 99, 110
 - Ising model, 42
 - island
 - average size, 129, 133, 134, 142
 - density of, 129, 133, 134, 142
 - growth, 129, 134
 - nucleation, 129, 134
 - size distribution, 13, 129, 133, 134, 142
 - jammed state, 58, 83, 88, 89, 95, 99
 - jamming coverage, 58, 65, 83, 88, 89, 95
 - kinetic Monte Carlo, *see* Monte Carlo, kinetic
 - KPZ, *see* universality class, Kardar-Parisi-Zhang
 - kurtosis, 58, 69, 76, 77
 - L. Onsager, 9, 42
 - Langevin, 15
 - damping term, 15
 - dynamics, 15
 - equation, 15
 - noise term, 15

- lattice, 13
- Liouville's equation, 10
- macrostate, 7
- Markovian process, 13, 14
- Master equation, 17, 42, 134
- mesh-cell test, 110
- microstate, 7
- model, 19
 - Ballistic Deposition, 27
 - Diffusion-limited aggregation, 22
 - Eden growth, 21
 - Random Deposition, 25
- moments, 58, 75, 77
- Monte Carlo, 62, 81, 110
 - direct, 37
 - importance sampling, 39, 42
 - integration, 37
 - kinetic, 47, 139, 142
 - Markov-chain, 37
 - method, 37
 - Monte Carlo steps, 42
 - N-fold way, 47
 - simple sampling, 39, 40
 - standard, 39
- MPCA (multiparticle-per-cell adsorption), 87, 89, 95
- nearest-neighbor pair-interaction, 134
- NICCA (noninteracting cell-cell adsorption), 87, 89
- non-integrable systems, 10
- nonequilibrium system, 9, 134
- out of equilibrium system, 9, 129, 131, 134
- pair correlation function, *see* interparticle distribution function
- pattern, 83
 - unit cell, 83
- patterned substrate, 81, 110
- percolation model, 40
- Phase diagram, 87
- phase functions, 7
- phase space, 7
- phase-space density, 10
- Poincaré, 10
- Poisson brackets, 10
- Poisson process, 13
- power law, 103
- prescribed bond scission, 134
- Random Sequential Adsorption, 57, 83
 - on a line, 55
 - algorithm, 63
 - jammed state structure, 65
 - on a surface, 81
- rare events, *see* infrequent events
- rate equations, *see* Master equation

regular substrate, *see* clean substrate

roughness, 25, 27

 saturation, 27

scaling, 22, 27

 function, 27

 relation, 27

silver, 129

skewness, 58, 69, 76, 77

spatial distribution of particles, 103

SPCA (single-particle-per-cell adsorption),

 87, 89, 95

spins, 42

state vector, 7

stochastic

 processes, 14

 systems, 14, 37

 variables, 14

submonolayer, 129, 134

time scales, 13, 47

transition rate, 17, 47, 131, 139

Transition State Theory, 13, 131

two-parameters space, 87

universality, 22, 25, 27

universality class, 22, 25, 27

 Kardar-Parisi-Zhang, 27

